Monthly Notices
of the
ROYAL ASTRONOMICAL SOCIETY

MNRAS **471,** 3915–3954 (2017)
Advance Access publication 2017 July 18

doi:10.1093/mnras/stx1776

MALT-45: A 7 mm survey of the southern Galaxy – II. ATCA follow-up observations of 44 GHz class I methanol masers

Christopher H. Jordan,[1,2,3,4★] Andrew J. Walsh,[1] Shari L. Breen,[4,5★] Simon P. Ellingsen,[3] Maxim A. Voronkov[3,4,6] and Lucas J. Hyland[3,4]

[1] *International Centre for Radio Astronomy Research, Curtin University, Bentley, WA 6845, Australia*
[2] *ARC Centre of Excellence for All-Sky Astrophysics (CAASTRO)*
[3] *School of Physical Sciences, Private Bag 37, University of Tasmania, Hobart, TAS 7001, Australia*
[4] *CSIRO Astronomy and Space Science, PO Box 76, Epping, NSW 1710, Australia*
[5] *Sydney Institute for Astronomy (SIfA), School of Physics, University of Sydney, Sydney, NSW 2006, Australia*
[6] *Astro Space Centre, Profsouznaya st. 84/32, 117997 Moscow, Russia*

Accepted 2017 July 12. Received 2017 July 11; in original form 2017 February 23

ABSTRACT

We detail interferometric observations of 44 GHz class I methanol masers detected by MALT-45 (a 7 mm unbiased auto-correlated spectral-line Galactic-plane survey) using the Australia Telescope Compact Array. We detect 238 maser spots across 77 maser sites. Using high-resolution positions, we compare the class I CH_3OH masers to other star formation maser species, including CS (1–0), SiO $v = 0$ and the H53 α radio-recombination line. Comparison between the cross- and auto-correlated data has allowed us to also identify quasi-thermal emission in the 44 GHz class I methanol maser line. We find that the majority of class I methanol masers have small spatial and velocity ranges ($<$0.5 pc and $<$5 km s^{-1}), and closely trace the systemic velocities of associated clouds. Using 870 μm dust continuum emission from the ATLASGAL survey, we determine clump masses associated with class I masers, and find that they are generally associated with clumps between 1000 and 3000 $M_\odot$. For each class I methanol maser site, we use the presence of OH masers and radio recombination lines to identify relatively evolved regions of high-mass star formation; we find that maser sites without these associations have lower luminosities and preferentially appear towards dark infrared regions.

Key words: masers – surveys – stars: formation – ISM: molecules – Galaxy: structure – radio lines: ISM.

1 INTRODUCTION

Methanol masers are excellent tracers of high-mass star-formation (HMSF; e.g. Walsh et al. 2003). Since their discovery (Menten 1991), 6.7 GHz methanol masers have been heralded as one of the most important spectral lines in astronomy; each of the transitions of the class II CH_3OH maser family, of which the 6.7 GHz transition belongs, occurs only towards regions of HMSF (Walsh et al. 2001; Minier et al. 2003; Green et al. 2012; Breen et al. 2013). These class II transitions are powered by mid-infrared emission from a nearby young stellar object (YSO), and dissipate as the H II region resulting from HMSF evolves (Walsh et al. 1998). Consequently, class II CH_3OH masers signpost a specific evolutionary phase of the HMSF timeline.

On the other hand, class I CH_3OH maser transitions have a relatively uncertain connection to HMSF. Observations have shown that class I CH_3OH masers can be found towards many star-forming regions and evolutionary stages, but not consistently, and not necessarily with or without the presence of class II masers (Ellingsen 2006; Breen et al. 2010b; Voronkov et al. 2010a; Ellingsen et al. 2013). Additionally, class I maser emission has been found towards low-mass star formation (Kalenskii et al. 2010), supernova remnants (McEwen, Pihlström & Sjouwerman 2014; Pihlström et al. 2014) and the centres of other galaxies (Ellingsen et al. 2014; Chen et al. 2015). In contrast to class II masers, class I masers are collisionally excited in dense molecular gas (Cragg et al. 1992; Voronkov et al. 2010a,b, 2014).

Another collisionally excited transition commonly found towards star-forming regions is thermal silicon monoxide (SiO $v = 0$), which traces a wide range of shocks (Nguyen-Lu'o'ng et al. 2013; Widmann et al. 2016), and has a rest frequency close to the class I CH_3OH maser. Thus, it is prudent to compare these spectral lines

★ E-mail: christopher.jordan@curtin.edu.au (CHJ); shari.breen@sydney.edu.au (SLB)

Table 1. Bright spectral lines between 42.2 and 49.2 GHz, targeted by MALT-45 and these observations. Column 1 lists the spectral line. Column 2 lists the rest frequency of the line. Column 3 classifies the line as either a maser or thermal line. Column 4 gives the ATCA half power beam width at the corresponding rest frequency. Column 5 indicates whether this line is catalogued in this paper ('Y') or not ('N'); this refers to the inclusion of Gaussian fits to the spectral emission from these lines. Column 6 lists the median RMS noise level for auto-correlation data per 32 kHz spectral channel, with errors representing the standard deviation. Radio recombination line (RRL) frequencies are taken from Lilley & Palmer (1968). All other rest frequencies are taken from the Cologne Database for Molecular Spectroscopy (Müller et al. 2005, 2013). Note that cross-correlation noise levels are given in Table 2.

Spectral line	Rest frequency (GHz)	Maser or thermal?	Beam size (arcsec)	Catalogued in this paper?	Median RMS noise level
SiO (1–0) $v = 3$	42.51938	Maser	66	N	
SiO (1–0) $v = 2$	42.82059	Maser	66	N	
H53α (RRL)	42.95197	Thermal	65	Y	6.5 ± 1.0 mK
SiO (1–0) $v = 1$	43.12207	Maser	65	N	
SiO (1–0) $v = 0$	43.42385	Thermal	65	Y	5.9 ± 0.67 mK
CH_3OH 7(0,7)–6(1,6) A^+	44.06941	Maser (Class I)	64	Y	170 ± 62 mJy
H51α (RRL)	48.15360	Thermal	58	N	
$C^{34}S$ (1–0)	48.20694	Thermal	58	N	8.1 ± 0.85 mK
CH_3OH 1_0–0_0 A^+	48.37246	Thermal	58	Y	7.7 ± 1.8 mK
CH_3OH 1_0–0_0 E	48.37689	Thermal	58	N	
OCS (4–3)	48.65160	Thermal	58	N	
CS (1–0)	48.99095	Thermal	57	Y	8.9 ± 1.3 mK

and learn more about class I CH_3OH masers. Additionally, high-density gas tracers such as carbon monosulfide (CS) highlight regions with potentially sufficient molecular gas abundance for masing. Investigations of the interstellar medium utilizing these spectral lines, which all occur in the 7 mm waveband, form the primary motivation for the Millimetre Astronomer's Legacy Team–45 GHz survey (MALT-45; Jordan et al. 2013, 2015). MALT-45 is an unbiased, sensitivity-limited auto-correlation survey of spectral lines in the 7 mm waveband, primarily surveying CS $J = (1–0)$, class I CH_3OH masers (the 44 GHz 7(0,7)–6(1,6) A^+ transition) and SiO $J = (1–0)$; a table of all surveyed spectral lines is contained in Table 2. Prior to the MALT-45 survey, class I CH_3OH masers were primarily found towards regions containing other masers or regions of shocked gas, such as extended green objects (EGOs; Cyganowski et al. 2008); very little was known about regions containing only class I maser emission.

The extent of the MALT-45 survey is currently detailed in a single paper (Jordan et al. 2015; hereafter Paper I). MALT-45 is unique in that it utilizes the Australia Telescope Compact Array (ATCA) by processing auto-correlated data (although cross-correlated data are simultaneously collected, it is not used due to extremely poor *uv*-coverage).Within the mapped region $330^\circ \leq l \leq 335^\circ, b = \pm 0.5^\circ$, Paper I details the detection of 77 class I methanol masers, 58 of which were new detections. For the first time, with a flux-density limited sample of class I sources, we are able to assess the bulk properties of these masers. Paper I in this series of MALT-45 publications briefly investigated the association of methanol masers with other detected spectral lines, but was ultimately limited by the spatial resolution of the auto-correlation survey (∼1 arcmin). In this paper, we detail the results of interferometric follow-up observations towards each of the class I CH_3OH masers observed in Paper I, in order to derive accurate positions.

2 OBSERVATIONS

Observations were conducted on 2013 September 7 and 8 by using the ATCA. The array configuration was 1.5A, which has five antennas distributed in the east–west direction with baselines ranging from 153 m to 1.5 km; the maximum baseline is 4.5 km including antenna 6 (CA06), however, due to poor weather, baselines including CA06 had bad phase stability. Consequently, data from CA06 are not included in this paper.

The correlator was programmed in the 64M-32k mode, which provides 'zoom windows' for enhanced spectral resolution. In this mode, each zoom window has a channel resolution of 32 kHz over a bandwidth of 64 MHz. This same correlator mode was used in the observations detailed by Paper I; however, unlike Paper I, these observations made use of 'stitched zooms': rather than using individual zoom windows, multiple zooms may be joined to increase the bandwidth over a spectral line, while maintaining the same spectral resolution. Each spectral line in these observations was observed with stitched zoom windows covering 96 MHz (except for the window containing H51α and $C^{34}S$ (1–0), which covers 224 MHz). For observations at 7 mm, the 32 kHz channel resolution corresponds to a spectral resolution of approximately 0.21 km s^{-1} per channel. The spectral lines observed are identical to that of Paper I; the list of observed lines and velocity coverage information and noise statistics are contained in Table 1. Since Paper I, the rest frequencies of the SiO (1–0) molecular lines have been updated (Müller et al. 2013).

The class I CH_3OH masers targeted in these observations are listed in Table 2. This target list was derived from a preliminary reduction of the MALT-45 survey and hence do not exactly match the maser sites presented in Paper I; however, there are only six sites that are not common to both papers. We include four sites in the current observations (G331.44−0.14, G331.44−0.16, G333.01−0.46 and G333.12−0.43) that were not listed in Paper I, and we have not targeted two that are listed in Paper I (G331.36−0.02 and G334.64+0.44), because they are tenuous detections that became apparent only in an improved processing of the MALT-45 survey, after the observations detailed by this paper were conducted. Hence, a total of 79 targets were observed over the 2 d of observations. For more details, refer to Section 3.

To obtain good *uv*-coverage, each target was observed multiple times over a single observing session. Each individual observation of a target lasted 1 min (one 'cut'), and each target has at least seven cuts, but some have up to 10; the noise levels for each target at the 44 GHz class I CH_3OH maser transition frequency are also listed in Table 2. Bandpass calibration was derived from PKS B1253−055,

Table 2. Observational targets for class I CH_3OH masers. Column 1 lists the site name taken from Paper I. Column 2 lists the refined site name, which is determined from the mean position of maser spots within a single maser site. The refined site names are used throughout this paper. A refined name is not supplied if no maser emission was detected in this work. Columns 3 and 4 list the interferometric phase centre for these observations (central maser positions are listed in Table 3). Column 5 gives the date on which the site was observed (2013 September 7 or 8). Column 6 lists the off-source image-plane median RMS noise value for the self-calibrated cube. Column 7 lists the smallest radius of a circle to encompass all emission of the site. Column 8 lists the velocity range of emission detected in auto-correlation data. All maser sites were observed with an approximate local standard of rest velocity coverage between −353 and 195 km s^{-1}. Note that sites with a radius of <1 arcsec contain either only one maser spot, or spots very close together. Sites without a specified radius were not detected in this work. Sites without a velocity range were not detected in cross- or auto-correlation (see Section 3). Sites labelled with an asterisk (∗) were not listed by Paper I, but have class I CH_3OH maser emission detected in these observations. Sites labelled with a dagger (†) are designated as 'young'; see Section 4.1. Sites labelled with a double dagger (‡) have large shifts induced by self-calibration; see Section 2.1.1.

Paper I site name	Refined site name	Interferometric phase centre α_{2000} (h:m:s)	δ_{2000} (°:′:″)	Obs. date (Sep. 2013)	Median RMS noise level (mJy)	Radius (arcsec)	Velocity range (km s^{-1})
G330.30−0.39	G330.294−0.393	16:07:37.0	−52:30:59	8	46	4	−82 to −76
G330.67−0.40	G330.678−0.402	16:09:30.6	−52:16:08	8	42	<1	−69 to −60
G330.78+0.24†	G330.779+0.249	16:07:12.2	−51:43:07	8	42	<1	−46 to −41
G330.83+0.18		16:07:40.6	−51:43:54	8	44		
G330.87−0.36	G330.876−0.362	16:10:16.6	−52:05:50	8	45	22	−66 to −57
G330.88−0.38	G330.871−0.383	16:10:21.1	−52:06:42	8	44	<1	−67 to −57
G330.92−0.41†	G330.927−0.408	16:10:44.2	−52:05:56	8	45	3	−44 to −40
G330.93−0.26†	G330.931−0.260	16:10:06.6	−51:59:23	8	43	1	−91 to −87
G330.95−0.18	G330.955−0.182	16:09:52.0	−51:54:59	8	46	<1	−98 to −84
G331.13−0.48†	G331.131−0.470	16:11:59.8	−52:00:32	8	44	<1	−70 to −65
G331.13−0.25	G331.132−0.244	16:10:59.7	−51:50:25	8	46	10	−93 to −78
G331.13−0.50	G331.134−0.488	16:12:05.9	−52:01:33	8	37	<1	−68 to −68
G331.13+0.15†	G331.134+0.156	16:09:14.8	−51:32:47	8	46	4	−79 to −73
G331.21+0.10		16:09:50.8	−51:32:39	8	44		
G331.29−0.20	G331.279−0.189	16:11:27.0	−51:41:54	8	45	21	−95 to −84
G331.34−0.35	G331.341−0.347	16:12:25.6	−51:46:16	8	46	<1	−67 to −64
G331.37−0.40†	G331.370−0.399	16:12:48.2	−51:47:26	8	44	<1	−66 to −64
G331.37−0.13†	G331.371−0.145	16:11:40.3	−51:35:52	8	47	<1	−89 to −86
G331.39+0.15†	G331.380+0.149	16:10:26.2	−51:22:52	8	46	<1	−47 to −43
G331.41−0.17†	G331.409−0.164	16:11:59.2	−51:35:33	8	45	<1	−85 to −85
G331.44−0.14*†		16:11:57.9	−51:33:08	8	45		−87 to −84
G331.44−0.19	G331.440−0.187	16:12:11.5	−51:35:02	8	44	5	−92 to −85
G331.44−0.16*†	G331.442−0.158	16:12:05.0	−51:33:45	8	40	<1	−87 to −85
G331.50−0.08	G331.492−0.082	16:11:59.6	−51:28:14	8	46	22	−93 to −84
G331.50−0.10	G331.503−0.109	16:12:10.5	−51:29:23	8	44	17	−101 to −86
G331.52−0.08	G331.519−0.082	16:12:07.5	−51:27:25	8	44	8	−93 to −85
G331.54−0.10	G331.530−0.099	16:12:14.5	−51:27:34	8	45	19	−95 to −85
G331.55−0.07	G331.544−0.067	16:12:11.3	−51:25:29	8	45	7	−92 to −85
G331.56−0.12	G331.555−0.122	16:12:26.7	−51:27:41	8	44	3	−104 to −97
G331.72−0.20†		16:13:34.4	−51:24:25	8	46		−49 to −45
G331.86−0.13†	G331.853−0.129	16:13:52.3	−51:15:42	8	46	<1	−52 to −48
G331.88+0.06†	G331.887+0.063	16:13:10.5	−51:06:09	8	44	12	−91 to −84
G331.92−0.08†	G331.921−0.083	16:13:58.0	−51:10:56	8	46	<1	−53 to −51
G332.09−0.42†	G332.092−0.420	16:16:15.6	−51:18:31	8	46	7	−59 to −54
G332.24−0.05†	G332.240−0.044	16:15:17.6	−50:55:59	8	47	8	−51 to −46
G332.30−0.09	G332.295−0.094	16:15:46.0	−50:55:54	8	46	8	−55 to −45
G332.32+0.18†	G332.318+0.179	16:14:40.0	−50:43:11	8	45	10	−50 to −44
G332.36−0.11	G332.355−0.114	16:16:07.3	−50:54:16	8	45	<1	−51 to −49
G332.59+0.15†	G332.583+0.147	16:15:58.5	−50:33:22	8	45	<1	−45 to −42
G332.60−0.17†	G332.604−0.167	16:17:28.1	−50:46:20	8	46	2	−48 to −44
G332.72−0.05†	G332.716−0.048	16:17:28.6	−50:36:34	8	45	2	−41 to −38
G333.00−0.43	G333.002−0.437	16:20:27.7	−50:41:06	8	45	<1	−57 to −55
G333.01−0.46*‡	G333.014−0.466	16:20:37.1	−50:41:31	7	41	<1	−55 to −52
G333.02−0.06†	G333.029−0.063	16:18:55.9	−50:24:03	8	43	1	−43 to −39
G333.03−0.02†	G333.029−0.024	16:18:45.9	−50:22:21	7	41	<1	−43 to −41
G333.07−0.44‡	G333.068−0.446	16:20:49.6	−50:38:51	7	46	<1	−55 to −51
G333.07−0.40	G333.071−0.399	16:20:37.0	−50:36:33	7	42	6	−54 to −51
G333.10−0.51	G333.103−0.502	16:21:13.4	−50:39:56	7	41	11	−60 to −53
G333.12−0.43*	G333.121−0.433	16:20:58.5	−50:35:41	7	54	3	−57 to −44
G333.13−0.44	G333.126−0.439	16:21:02.3	−50:35:53	7	55	12	−57 to −42
G333.14−0.42	G333.137−0.427	16:21:03.0	−50:34:59	7	49	17	−57 to −43
G333.16−0.10	G333.162−0.101	16:19:41.4	−50:19:55	7	35	4	−93 to −90

Table 2 – *continued*

Paper I site name	Refined site name	Pointing centre α_{2000} (h:m:s)	Pointing centre δ_{2000} (°:′:″)	Obs. date (Sep. 2013)	Median RMS noise level (mJy)	Radius (arcsec)	Velocity range (km s^{-1})
G333.18−0.09	G333.184−0.090	16:19:45.2	−50:18:45	7	37	10	−89 to −84
G333.22−0.40	G333.220−0.402	16:21:16.9	−50:30:17	7	42	4	−57 to −49
G333.23−0.06	G333.233−0.061	16:19:49.4	−50:15:17	7	42	14	−96 to −81
G333.24+0.02†		16:19:26.0	−50:11:29	7	42		−71 to −66
G333.29−0.38	G333.284−0.373	16:21:28.1	−50:26:35	7	43	<1	−55 to −49
G333.30−0.35	G333.301−0.352	16:21:24.5	−50:24:47	7	40	<1	−54 to −48
G333.31+0.10	G333.313+0.106	16:19:27.6	−50:04:45	7	55	8	−51 to −43
G333.33−0.36	G333.335−0.363	16:21:36.4	−50:23:53	7	44	18	−55 to −46
G333.37−0.20†‡	G333.376−0.202	16:21:05.2	−50:15:18	7	44	5	−63 to −56
G333.39+0.02	G333.387+0.031	16:20:08.2	−50:04:49	7	39	3	−73 to −68
G333.47−0.16	G333.467−0.163	16:21:19.5	−50:09:42	7	40	12	−49 to −38
G333.50+0.15†	G333.497+0.143	16:20:06.5	−49:55:25	7	42	2	−115 to −111
G333.52−0.27‡	G333.523−0.275	16:22:03.4	−50:12:08	7	42	<1	−52 to −49
G333.56−0.30	G333.558−0.293	16:22:19.2	−50:11:28	7	42	27	−47 to −44
G333.56−0.02†	G333.562−0.025	16:21:07.9	−49:59:49	7	44	<1	−43 to −37
G333.57+0.03†	G333.569+0.028	16:20:55.4	−49:57:25	7	42	<1	−86 to −81
G333.59−0.21‡	G333.595−0.211	16:22:06.2	−50:06:30	7	45	4	−52 to −44
G333.70−0.20	G333.694−0.197	16:22:27.7	−50:01:22	7	41	9	−52 to −49
G333.71−0.12†‡	G333.711−0.115	16:22:10.8	−49:57:21	7	41	5	−32 to −30
G333.77−0.01†‡	G333.772−0.010	16:21:59.6	−49:50:20	7	42	<1	−91 to −88
G333.77−0.25†‡	G333.773−0.258	16:23:02.8	−50:00:31	7	40	<1	−50 to −47
G333.82−0.30†	G333.818−0.303	16:23:29.5	−50:00:40	7	41	1	−50 to −46
G333.90−0.10‡	G333.900−0.098	16:22:56.3	−49:48:43	7	41	4	−66 to −61
G333.94−0.14†‡	G333.930−0.133	16:23:14.1	−49:48:40	7	44	5	−43 to −39
G333.98+0.07†	G333.974+0.074	16:22:31.0	−49:38:08	7	40	<1	−62 to −57
G334.03−0.04†	G334.027−0.047	16:23:16.7	−49:40:57	7	41	<1	−85 to −83
G334.74+0.51†	G334.746+0.506	16:23:57.9	−48:46:40	7	38	4	−66 to −59

phase calibration from PMN J1646−5044 and flux-density calibration from PKS B1934−638. Partridge et al. (2016) give a flux density scale for B1934−638, which yields a flux density of 0.31 Jy at the rest frequency of the 44 GHz class I CH_3OH maser spectral line. However, we used the recommended flux density of 0.39 Jy derived from the internal work with the ATCA. In addition to the cross-correlation data, auto-correlation data were simultaneously recorded and used; see Section 2.1.2.

2.1 Data reduction

2.1.1 Cross-correlation

Class I CH_3OH maser data were reduced using standard interferometric techniques with MIRIAD (Sault, Teuben & Wright 1995). For all data cubes, the synthesized beam is approximately 0.5 × 1 arcsec in right ascension and declination, respectively. Similar to Voronkov et al. (2014), the results presented in this paper make use of self-calibrated data cubes. Self-calibration affects the absolute positional accuracy of data; to remove this effect, a reference maser spot was chosen from data with no self-calibration applied. The position of this reference spot was determined before and after self-calibration and the measured difference was used to determine the absolute positions for all spectral features in the self-calibrated data cube. Ideally, the reference position before and after self-calibration has not shifted significantly (<0.5 arcsec), but some significant offsets were observed in these data due to poor weather conditions during the observations, which leads to large corrections in the self-calibration model. Models were selected from the brightest channel of emission from CLEANed data, which is generally effective, but occasionally the quality of calibration was so poor that the resulting self-calibrated data experiences a dramatic spatial shift. Despite this, we are encouraged by the accuracy of positions once a reference position has been subtracted; for example, G333.23−0.06 experienced poor calibration, but the difference in position of the brightest maser spot of G333.23−0.06 between this work and that of Voronkov et al. (2014) is 1.2 arcsec. This difference may result from a combination of genuine maser variability and calibration uncertainties. Prior experience with the ATCA in this waveband suggests that, in the best case scenario, the standard phase transfer calibration procedure on the absolute positional accuracy results in an error of approximately 0.5 arcsec (1σ) (Voronkov et al. 2014). However, given that we experience non-ideal self-calibration offsets, the absolute positional error for any maser spot should be considered to be 1 arcsec.

Data cubes were produced for each of the observed targets, which were then used to identify maser spots by visual inspection. In this paper, a maser spot refers to a spatial and spectral peak of emission. Spots were identified if the spectrum contained at least three consecutive channels of 3σ emission, with a peak of at least 5σ within the same pixel (0.2 arcsec). We employ this conservative approach of maser identification so the reader can be confident that all identified maser spots are real. A small number of weaker, narrow features may not satisfy these criteria and so are excluded; however, from past experience and comparison of our cubes with previous observations (where available), we suggest that this is not common. The requirement of three significant consecutive channels has the effect of limiting our maser detections to a velocity width of at least 0.65 km s^{-1}. Similar to Voronkov et al. (2014), dynamic range limitations exist for channels containing extremely bright maser

emission. This reduces the ability to identify real maser emission at a similar velocity to the bright feature; maser spots were excluded where they are believed to have been caused by such dynamic range artefacts. These exclusions were determined by visual inspection.

The position of each maser spot was fitted with the MIRIAD task IMFIT using each channel of significant emission ($>3\sigma$). IMFIT used a 3×3 arcsec box around each maser spot to generate a position, except for those with nearby bright maser spots. To accurately position weaker maser spots close to bright ones, either the velocity range of emission was altered for position fitting, or the size of the box for fitting was decreased. Decreasing the size of the box for IMFIT was found not to significantly affect resultant positions, so we do not highlight the maser spots using these modified procedures. Each channel-fitted position is then flux density-weighted and is listed in Appendix A1. The uncertainty reflects the 1σ positional uncertainty of each channel-fitted position. In some cases, the maser spot positions have uncertainties of a few tens of milliarcsec. We caution that the ATCA is likely not able to determine relative positions to this accuracy for these observations, as dynamic range and calibration uncertainties become a limiting factor. In general, we found the class I maser spots were spatially distinguished by our observations, with separations of 1 arcsec or greater, but occasionally spots were very near to a bright neighbour. In these cases, positions were manually assigned by using the brightest pixel, with a cautious position uncertainty of 100 milliarcsec in Right Ascension and 200 milliarcsec in Declination. Such maser spots are designated with an asterisk ($*$) in Appendix A1.

Spectral information for each maser spot was derived from the image cubes, which were then characterized with Gaussian fits. All residuals are within 10 per cent of the fitted peak intensity. Coupled with uncertainties in calibration, we expect a 20 per cent uncertainty for all quoted flux-density values.

2.1.2 *Auto-correlation*

Each observation target was also searched for CS (1–0), SiO (1–0) $v = 0$ and CH_3OH 1_0–0_0 A^+. However, due to their thermal nature and the *uv*-coverage of the observations (minimum baseline length of 153 m), these thermal emission lines were not readily detectable in the cross-correlation data. To report on these properties, a RUBY script was written to assist with the analysis of the auto-correlated data. Unlike the observations detailed by Paper I, no dedicated reference (i.e. off) position was observed in this work. Instead, data collected at a location where the emission is known to be weak and have a simple spectral profile were used as the reference spectrum for auto-correlations. The script routine pipeline was as follows:

(i) For each source, a raw auto-correlation spectrum was produced for each antenna and each cut.

(ii) For each antenna source cut, a quotient spectrum (i.e. ${}^{\mathrm{on}-\mathrm{off}}/_{\mathrm{off}}$) was formed from the source and reference cut data.

(iii) A first-order polynomial was fitted to and removed from the spectra. The velocity range of the fit was restricted between -160 and $20\,\mathrm{km\,s^{-1}}$, as this contains all of the emission in this section of the Galaxy, and constraining the fit improves the quality of the resulting spectra.

(iv) All quotient spectra from an antenna are averaged together, before averaging all antennas together.

(v) The flux-density calibration is achieved with antenna efficiencies and point-source sensitivities taken from Urquhart et al. (2010).

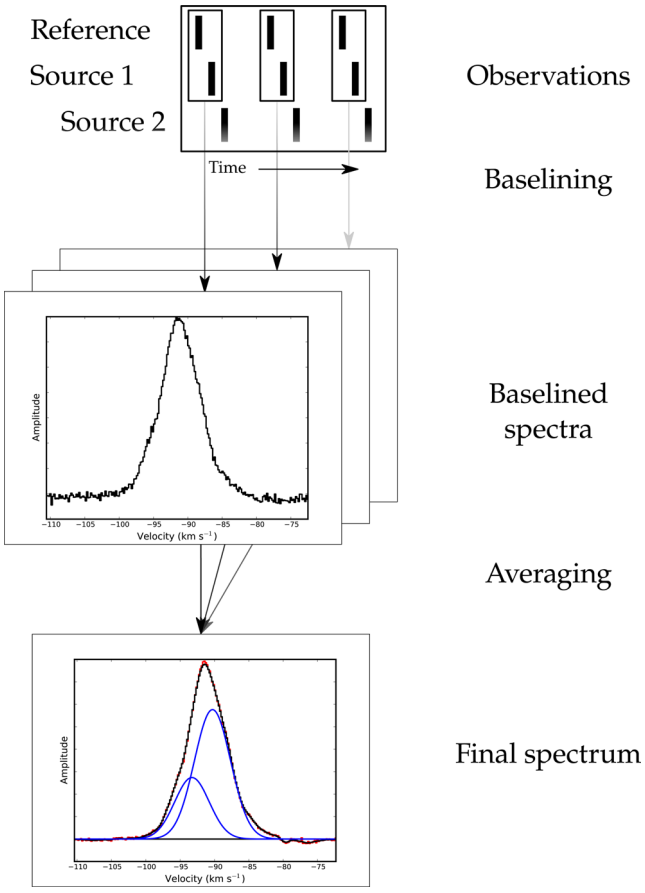

Figure 1. A graphical representation of the reduction procedure for auto-correlated data in this paper. The data from each source cut are combined with the nearest reference cut in time to produce a baselined spectrum. All baselined spectra are then averaged to produce an auto-correlation product. This procedure is performed for each antenna of the ATCA, and all products are then averaged together for a final product. The final panel contains this final product spectrum (red) and the same spectrum after being Hanning-smoothed (black). This example uses two Gaussians (blue) to characterize the data.

This procedure is graphically demonstrated with the CS emission of G330.95−0.18 in Fig. 1.

For the spectral line data processed in this way, spectra were smoothed with a Hanning window of 9 spectral channels, and up to two Gaussians were fitted to the frequency data. This smoothing results in a velocity resolution of $\sim$0.39 km s^{-1} for CS, $\sim$0.44 km s^{-1} for SiO $v = 0$ and $\sim$0.40 km s^{-1} for CH_3OH 1_0–0_0 A^+. As with the cross-correlation data, Gaussians are fitted to minimize residuals; however, occasionally 10 per cent residuals are unavoidable. With additional flux-density calibration uncertainty applied to auto-correlation data, we place a 20 per cent uncertainty on all intensity values derived.

This auto-correlation procedure was also used for class I CH_3OH masers, which we compare with the cross-correlation data in Section 4.5.

3 RESULTS

The basic properties of each observed target are listed in Table 2. Note that five sources were not detected in cross-correlation by these observations, but three of these five were detected in auto-correlation (G331.44−0.14, G331.72−0.20 and G333.24+0.02).

The reason that three of the sites were detected in auto-correlation data, but not cross-correlation data, could either be due to poor weather (causing significant decorrelation) or, alternatively, it may indicate that the emission region is large, and is therefore resolved out in the cross-correlation data. The fact that the spectral profile of these three sources is consistent with maser emission (although relatively weak maser emission; each of the three sources is less than ∼2 Jy) suggests that the most likely explanation for their non-detection is due to poor weather. Further discussion of cross-correlation spectra compared to the auto-correlation data for the same source is contained in Section 4.5.

The remaining two sources, G330.83+0.18 and G331.21+0.10, were detected in October 2013 with peak-flux densities of 3.1 and 3.5 Jy. The median RMS noise of the survey observations was 0.90 Jy, meaning that they were detected a 3.4σ and 3.8σ level, respectively. It is therefore pyesossible that these were spurious detections, or, alternatively, that their peak-flux densities have varied below the 0.85 Jy 5σ detection limit for the current observations. A variation factor of 4 seems reasonable for 44 GHz masers (e.g. variations larger than 4 were found in two sources detailed by Kurtz, Hofner & Álvarez 2004), although there have been no dedicated studies. Given the current data, and the low significance of the original detections, these two sources cannot be considered reliable detections and as such we exclude them from further analysis. For the remainder of this paper, we discuss the 77 regions containing 44 GHz class I CH_3OH emission.

We have classified our class I CH_3OH masers as associated with other maser transitions or selected HMSF tracers if they fall within 60 arcsec of each other, to be consistent with Voronkov et al. (2014). The associations are detailed in Table 3. Each site is compared with published positions of class II CH_3OH (Caswell et al. 2011), water (H_2O) (Breen et al. 2010b; Walsh et al. 2011, 2014) and hydroxyl (OH) masers (Sevenster et al. 1997; Caswell 1998), as well as ATLASGAL clumps (Contreras et al. 2013) and EGOs (Cyganowski et al. 2008). The presence of each thermal line is determined by the method described in Section 2.1.2, using data from these observations. CS is detected towards every source, and because of this is not listed in Table 3. The Gaussian parameters determined for each of the thermal lines are listed in Appendix B. Uncertainties for each of the fitted parameters are quoted; however, we remind the reader to consider the 20 per cent uncertainty adopted for the absolute flux-density scale.

Note that Walsh et al. (2011) detail single-dish positions of H_2O masers, while Walsh et al. (2014) provide high-resolution follow-up positions of these same masers. Hence, we use positions from Walsh et al. (2014) wherever possible; however, two H_2O masers (G331.86+0.06 and G333.46−0.16) were not detected in follow-up observations, and thus we use their single-dish positions for comparisons in this paper. The non-detection of these masers is reasoned as being most likely due to intrinsic variability.

Kinematic distances are also contained in Table 3. Distances were calculated using the program supplied by Reid et al. (2009). All kinematic distance ambiguities were assumed to be at the 'near' distance, except for sources that have been prescribed as 'far' by Green & McClure-Griffiths (2011). All distances presented in this paper use the same parameters as Paper I, specifically: $\Theta_0 = 246\,\mathrm{km\,s^{-1}}$, $R_\odot = 8.4\,\mathrm{kpc}$, $U_\odot = 11.1\,\mathrm{km\,s^{-1}}$, $V_\odot = 12.2\,\mathrm{km\,s^{-1}}$, $W_\odot = 7.25\,\mathrm{km\,s^{-1}}$, $U_s = 0\,\mathrm{km\,s^{-1}}$, $V_s = -15.0\,\mathrm{km\,s^{-1}}$, $W_s = 0\,\mathrm{km\,s^{-1}}$, $\sigma(V_{\mathrm{LSR}}) = 3.32\,\mathrm{km\,s^{-1}}$.

We consider all maser spots detected towards a single target to be part of the same maser site. There is potential for this to artificially to combine multiple maser sites into a single site; however, Apprendix C shows that this is uncommon. To illustrate the derived properties of masers, a sample of Gaussian fits to spectra is included in Table 4. The complete collection of Gaussian spectral fits is included in Appendix A1. Maser positions overlaid on infrared images from the *Spitzer* Galactic Legacy Infrared Mid-Plane Survey Extraordinaire (GLIMPSE; Benjamin et al. 2003) can be seen in Appendix C.

The auto-correlation sensitivity of these observations is approximately a factor of 5 better than that of Paper I, and has improved the detection rate of thermal lines towards the class I CH_3OH masers. Paper I described detectable CS emission towards 95 per cent of class I CH_3OH masers, whereas these data have detectable CS towards every maser. Similarly, the detection rate of thermal SiO has greatly improved; these data have detectable SiO towards 83 per cent of regions (64/77), which is a significant increase over Paper I (30 per cent). The thermal 1_0–0_0 A^+ line of CH_3OH was not characterized in Paper I, but auto-correlations have been produced for this paper. The thermal line of CH_3OH in this frequency band is detected towards almost all regions (75/77; 97 per cent). In addition, we list detections of H53α and $C^{34}S$ in Table 3, along with median RMS noise levels in Table 1. The thermal lines are used for various comparisons in Section 4. The Gaussian parameters determined for each of the thermal lines are listed in Appendix B.

4 DISCUSSION

With the first large and unbiased sample of class I CH_3OH masers, we perform a number of analyses to determine any relationships between this maser transition and other star formation tracers. Given that we simultaneously collect useful thermal lines associated with HMSF, such as CS (1–0), we often compare these with the class I masers to better understand their environments. In addition, we use other surveys pertaining to star formation, such as the Methanol MultiBeam (MMB) and ATLASGAL, in an attempt to identify what class I CH_3OH maser emission can tell us about their host star-forming regions.

4.1 Class I CH_3OH masers on an HMSF evolutionary timeline

Voronkov et al. (2014) found that class I CH_3OH masers likely trace multiple evolutionary phases of the HMSF timeline, perhaps ranging from very young sources tracing outflows to very evolved sources featuring expanding H II regions. In this subsection, we attempt to divide class I CH_3OH masers into 'young' or 'evolved' categories. Paper I briefly discusses class I CH_3OH masers with associated class II CH_3OH or OH masers; class I CH_3OH masers associated with either or both of these types of maser were assumed to be in a relatively late stage of HMSF. Paper I notes that the majority of class I CH_3OH masers lack these associations and therefore seem more likely to be associated with earlier stages of HMSF. With the additional sensitivity provided by the follow-up observations discussed in this paper, we may also use radio recombination line (RRL) data to help discriminate HMSF regions between evolved and young stages. RRLs are associated with H II regions, which typically signpost more evolved stages of HMSF than class II CH_3OH masers (Walsh et al. 1998). As OH masers also occur late in an evolutionary timeline (e.g. Caswell 1997), in this paper, we categorize maser sites as 'evolved' if H53α emission was detected or an OH maser is associated, or both. Otherwise, the class I CH_3OH site is deemed 'young'. The presence of H53α emission as well as all maser associations with class I CH_3OH maser sites is listed in Table 3.

Table 3. Associations with each of the class I CH_3OH maser sites. Note that the presence of CS (1–0) is not listed, because it is detected towards every source. Column 1 lists the refined region name. Columns 2 and 3 list the equatorial coordinates of the mean position of all maser spots within a single maser site. Column 4 lists the kinematic distance (Reid et al. 2009). Uncertainties are listed in units of the least significant figure. Column 5 lists the associations with other masers, EGOs and ATLASGAL sources within 1 arcmin of the centre position[a]. If there is more than one of the same type of emission, it is listed as a subscript. Columns 6 through 9 list whether thermal SiO (1–0), CH_3OH 1_0–0_0 A^+, H53α or $C^{34}S$ (1–0) emission is detected ('Y') or not ('N'). Regions labelled with a dagger (†) are designated as 'young'; see Section 4.1. Regions labelled with a double dagger (‡) have large shifts induced by self-calibration; see Section 2.1.1.

Region name	Centre of maser emission α_{2000} (h:m:s)	δ_{2000} (°:′:″)	Kinematic distance (kpc)	Associations within 1 arcmin[1]	Presence of SiO (1–0) $v = 0$?	Presence of CH_3OH 1_0–0_0 A^+?	Presence of H53α?	Presence of $C^{34}S$ (1–0)?
G330.294−0.393	16:07:37.9	−52:30:58.29	4.9 (2)	WA	N	Y	Y	Y
G330.678−0.402	16:09:31.7	−52:15:50.68	4.1 (2)	A	Y	Y	Y	Y
G330.779+0.249†	16:07:09.8	−51:42:53.76	3.1 (2)	A	Y	Y	N	Y
G330.871−0.383	16:10:22.1	−52:07:08.28	4.1 (2)	MA	Y	Y	Y	Y
G330.876−0.362	16:10:17.9	−52:05:59.37	4.0 (2)	$MWSCGA_2$	Y	Y	Y	Y
G330.927−0.408†	16:10:44.7	−52:05:57.33	3.1 (2)	A	Y	Y	N	Y
G330.931−0.260†	16:10:06.7	−51:59:18.13	5.3 (2)	A	N	Y	N	Y
G330.955−0.182	16:09:53.0	−51:54:52.84	5.5 (2)	MWCA	Y	Y	Y	Y
G331.131−0.470†	16:11:59.4	−52:00:19.88	4.3 (2)	GA	Y	Y	N	Y
G331.132−0.244	16:10:59.8	−51:50:21.78	5.4 (2)	MWCGA	Y	Y	N	Y
G331.134−0.488	16:12:05.1	−52:01:01.37	4.3 (2)	A	Y	Y	Y	Y
G331.134+0.156†	16:09:15.1	−51:32:39.79	4.6 (2)	MWA	Y	Y	N	Y
G331.279−0.189	16:11:27.2	−51:41:57.04	5.3 (2)	MWCA	Y	Y	Y	Y
G331.341−0.347	16:12:26.4	−51:46:20.50	4.2 (2)	MWCGA	Y	Y	Y	Y
G331.370−0.399†	16:12:48.5	−51:47:24.39	4.2 (2)	GA	N	Y	N	Y
G331.371−0.145†	16:11:41.2	−51:36:15.36	5.2 (2)		N	Y	N	Y
G331.380+0.149†	16:10:26.8	−51:22:58.46	3.2 (2)	A	Y	Y	N	Y
G331.409−0.164†	16:11:57.4	−51:35:32.03	5.1 (2)	A_3	Y	Y	N	Y
G331.44−0.14†	16:11:57.9	−51:33:07.81	5.1 (2)	A	Y	Y	N	N
G331.440−0.187	16:12:11.9	−51:35:15.76	9.6 (2)	MWCA	Y	Y	N	Y
G331.442−0.158†	16:12:04.8	−51:33:55.74	5.1 (2)		Y	Y	N	Y
G331.492−0.082	16:11:59.0	−51:28:34.01	5.3 (2)	A_2	Y	Y	Y	Y
G331.503−0.109	16:12:09.3	−51:29:14.95	5.2 (2)	$WSCA_3$	Y	Y	Y	Y
G331.519−0.082	16:12:06.6	−51:27:25.69	5.3 (2)	A	Y	Y	Y	Y
G331.530−0.099	16:12:14.3	−51:27:44.11	5.4 (2)	A	Y	Y	Y	Y
G331.544−0.067	16:12:09.7	−51:25:44.35	5.2 (2)	MCA	Y	Y	Y	Y
G331.555−0.122	16:12:27.1	−51:27:42.69	5.8 (2)	MW_2CA_2	Y	Y	Y	Y
G331.72−0.20†	16:13:34.4	−51:24:24.91	3.3 (2)	A	Y	Y	N	Y
G331.853−0.129†	16:13:52.5	−51:15:46.63	3.4 (2)	A	Y	Y	N	Y
G331.887+0.063†	16:13:11.2	−51:05:58.39	5.2 (2)	A	Y	Y	N	Y
G331.921−0.083†	16:13:59.2	−51:10:56.00	3.5 (2)	A	Y	Y	N	Y
G332.092−0.420†	16:16:15.7	−51:18:27.64	3.7 (2)	MWA	Y	Y	N	Y
G332.240−0.044†	16:15:17.2	−50:56:01.32	3.4 (2)	A	Y	Y	N	Y
G332.295−0.094	16:15:45.3	−50:55:54.87	3.5 (2)	MWGA	Y	Y	Y	Y
G332.318+0.179†	16:14:40.1	−50:43:07.07	3.4 (2)	WA	Y	Y	N	Y
G332.355−0.114	16:16:07.2	−50:54:19.92	3.5 (2)	MWCGA	N	Y	N	Y
G332.583+0.147†	16:16:01.0	−50:33:30.96	11.8 (2)	MGA	N	N	N	Y
G332.604−0.167†	16:17:29.3	−50:46:12.92	3.3 (2)	MWGA	Y	Y	N	Y
G332.716−0.048†	16:17:28.5	−50:36:23.32	3.0 (2)	A	N	Y	N	Y
G333.002−0.437	16:20:28.7	−50:41:00.91	3.8 (2)	WA_3	Y	Y	Y	Y
G333.014−0.466‡	16:20:39.5	−50:41:47.45	3.6 (2)	A	Y	Y	Y	Y
G333.029−0.063†	16:18:56.7	−50:23:54.64	3.0 (2)	MWA	N	Y	N	Y
G333.029−0.024†	16:18:46.6	−50:22:14.57	3.1 (2)	MA_2	Y	Y	N	Y
G333.068−0.446‡	16:20:48.7	−50:38:38.68	3.7 (2)	MWA	Y	Y	Y	Y
G333.071−0.399	16:20:37.2	−50:36:30.13	3.6 (2)	A	Y	Y	Y	Y
G333.103−0.502	16:21:13.1	−50:39:31.37	3.8 (2)	MA	Y	Y	Y	Y
G333.121−0.433	16:20:59.5	−50:35:51.03	3.4 (2)	$M_4W_6C_2A_2$	Y	Y	Y	Y
G333.126−0.439	16:21:02.6	−50:35:52.44	3.5 (2)	$M_4W_6C_2A_2$	Y	Y	Y	Y
G333.137−0.427	16:21:02.2	−50:34:56.03	3.5 (2)	MWC_2A	Y	Y	Y	Y
G333.162−0.101	16:19:42.5	−50:19:56.29	5.3 (2)	MA_2	N	Y	Y	Y
G333.184−0.090	16:19:45.5	−50:18:34.59	5.1 (1)	MGA	Y	Y	Y	Y
G333.220−0.402	16:21:17.9	−50:30:19.97	3.6 (2)	A	Y	Y	Y	Y
G333.24+0.02†	16:19:26.0	−50:11:29.26	4.4 (1)	A	Y	Y	N	Y
G333.233−0.061	16:19:50.8	−50:15:15.94	5.1 (1)	M_2W_3SCA	Y	Y	N	Y
G333.284−0.373	16:21:27.3	−50:26:22.48	3.6 (2)	A	Y	Y	Y	Y
G333.301−0.352	16:21:25.9	−50:24:46.26	3.5 (2)	A_2	Y	Y	Y	Y

Table 3 – *continued*

Site name	Centre of maser emission α_{2000} (h:m:s)	δ_{2000} (°:′:″)	Kinematic distance (kpc)	Associations within 1 arcmin[1]	Presence of SiO (1–0) $v = 0$?	Presence of CH_3OH 1_0–0_0 A^+?	Presence of H53α?	Presence of $C^{34}S$ (1–0)?
G333.313+0.106	16:19:28.5	−50:04:45.61	11.8 (2)	MWCGA	Y	Y	N	Y
G333.335−0.363	16:21:38.0	−50:23:46.78	3.6 (2)	A	Y	Y	Y	Y
G333.376−0.202†‡	16:21:06.2	−50:15:13.21	4.0 (2)	WA	Y	Y	N	Y
G333.387+0.031	16:20:07.5	−50:04:49.51	10.6 (1)	MWCA	Y	Y	N	Y
G333.467−0.163	16:21:20.2	−50:09:41.70	3.1 (2)	MWCGA	Y	Y	Y	Y
G333.497+0.143†	16:20:07.6	−49:55:26.21	6.3 (2)	A_2	Y	Y	N	Y
G333.523−0.275‡	16:22:04.5	−50:12:05.32	3.5 (2)	A	Y	Y	Y	Y
G333.558−0.293	16:22:18.7	−50:11:23.38	3.1 (2)	A_2	Y	Y	Y	Y
G333.562−0.025†	16:21:08.7	−49:59:48.85	12.0 (2)	MA	Y	Y	N	Y
G333.569+0.028†	16:20:56.6	−49:57:15.91	5.0 (1)	A	Y	Y	N	Y
G333.595−0.211‡	16:22:06.7	−50:06:21.28	3.5 (2)	WSCA	Y	Y	Y	Y
G333.694−0.197	16:22:29.1	−50:01:31.84	3.5 (2)	A_2	Y	Y	Y	Y
G333.711−0.115†‡	16:22:12.1	−49:57:20.77	2.5 (2)	A	N	N	N	Y
G333.772−0.010†‡	16:22:00.3	−49:50:15.79	5.2 (1)		N	Y	N	Y
G333.773−0.258†‡	16:23:06.2	−50:00:43.31	3.5 (2)	A	Y	Y	N	Y
G333.818−0.303†	16:23:30.0	−50:00:41.97	3.4 (2)		N	Y	N	Y
G333.900−0.098‡	16:22:57.3	−49:48:35.60	10.9 (2)	MSA	Y	Y	N	Y
G333.930−0.133†‡	16:23:14.5	−49:48:45.94	3.1 (2)	MWA	Y	Y	N	Y
G333.974+0.074†	16:22:31.4	−49:38:08.31	3.9 (2)	A	N	Y	N	Y
G334.027−0.047†	16:23:16.7	−49:41:00.19	5.0 (1)	A_2	N	Y	N	Y
G334.746+0.506†	16:23:58.0	−48:46:59.12	4.2 (1)	A	Y	Y	N	Y

Note. [a]M – 6.7 GHz CH_3OH maser from Caswell et al. (2011); W – 22 GHz H_2O maser from any of Breen et al. (2010b); Walsh et al. (2011, 2014); S – 1612 MHz OH maser from Sevenster et al. (1997); C – 1665 or 1667 MHz OH maser from Caswell (1998); G – EGO from Cyganowski et al. (2008); A – ATLASGAL point source from Contreras et al. (2013).

Table 4. A sample of Gaussian spectral fits for class I CH_3OH maser spots: only those in region G331.132−0.244. The remainder of fits are provided in Appendix A1. Column 1 lists the Galactic coordinates of each distinct spectral feature. In the case where there is more than one velocity component at exactly the same location, the letter associated with the Galactic position is incremented. Spots labelled with an asterisk (∗) have been manually fitted; see Section 2.1.1. Columns 2 and 3 list the fitted position for the Gaussian. Columns 4 through 6 list the fitted Gaussian parameters. Note that the uncertainty for each parameter is quoted in parentheses, in units of the least significant figure. Column 7 lists the integrated flux density of the Gaussian.

Spot name	α_{2000} (h:m:s)		δ_{2000} (°:′:″)		Peak flux density (Jy)		Peak velocity (km s^{-1})		FWHM (km s^{-1})		Integrated flux density (Jy km s^{-1})
G331.1308−0.2441A	16:10:59.53	(2)	−51:50:25.79	(4)	13.0	(6)	−87.50	(3)	1.45	(7)	14.148
G331.1308−0.2441B	16:10:59.54	(6)	−51:50:25.72	(5)	21	(4)	−90.1	(1)	1.6	(3)	24.901
G331.1308−0.2441C	16:10:59.54	(6)	−51:50:25.68	(9)	93	(3)	−91.11	(1)	0.93	(3)	65.276
G331.1333−0.2458A	16:11:00.7	(5)	−51:50:23.97	(6)	45	(1)	−88.531	(8)	0.70	(2)	23.769
G331.1333−0.2410A	16:10:59.41	(2)	−51:50:11.8	(1)	23.1	(2)	−84.630	(2)	0.610	(5)	10.604
G331.1333−0.2410B	16:10:59.45	(2)	−51:50:11.64	(2)	2.9	(1)	−86.19	(1)	0.53	(3)	1.151
G331.1322−0.2454A	16:11:00.25	(6)	−51:50:25.71	(1)	6.5	(2)	−84.34	(1)	0.81	(3)	3.986
G331.1322−0.2454B	16:11:00.29	(4)	−51:50:26.0	(1)	6.3	(2)	−87.667	(8)	0.47	(2)	2.244
G331.1332−0.2407A	16:10:59.30	(4)	−51:50:10.90	(3)	2.11	(6)	−85.718	(8)	0.59	(2)	0.931
G331.1313−0.2434A	16:10:59.499	(9)	−51:50:22.76	(5)	4.19	(7)	−86.097	(3)	0.412	(7)	1.300
G331.1315−0.2441A	16:10:59.73	(8)	−51:50:24.2	(1)	0.90	(5)	−82.85	(2)	0.57	(4)	0.386
G331.1313−0.2451A	16:10:59.9	(2)	−51:50:27.2	(2)	0.89	(7)	−82.53	(4)	0.91	(8)	0.610

From the 77 observed class I CH_3OH maser regions, we classify 41 as evolved (being associated with either an OH maser or H53α emission, 53 per cent). Curiously, when using catalogues of class II CH_3OH and OH masers, we find that a large number of maser sites (16/77; 21 per cent) featuring H53α emission are without class II CH_3OH or OH masers. Perhaps these regions are too evolved to harbour class II CH_3OH or OH masers, or alternatively, it could be that the class II CH_3OH or OH maser emission is too weak to be detected. The population of OH masers within the MALT-45 survey region is primarily formed by the catalogue of Caswell (1998); this survey details detections to a limit of 0.16 Jy, but Caswell (1998) note that the survey is not complete at this level, requiring emission across several channels or corroboration with other data. Additional masers from the SPLASH survey may reveal new associations (Dawson et al. 2014; Qiao et al. 2016). Across the MALT-45 survey region, class II CH_3OH masers from the MMB survey are complete to a 5σ detection limit at 1.0 Jy (Caswell et al. 2011). Given the good sensitivity of these surveys, it seems unlikely that undiscovered class II CH_3OH and OH masers are associated with these class I CH_3OH masers, but follow-up observations at these transitions may prove effective for finding new detections.

Another explanation for 21 per cent of our sites featuring H53α emission but neither class II CH_3OH nor OH masers is that bright H53α emission originates from nearby sources of HMSF, contaminating what we would otherwise deem as young regions of star formation. The G333 giant molecular cloud (Bains et al. 2006; Fujiyoshi et al. 2006) powers bright H53α emission, which may cause false-positive associations of H53α at sites near to this complex. Thus, it can be difficult to accurately discriminate between young and evolved HMSF regions by using only RRL data; however, we suggest that this is generally uncommon, as the H_2O Galactic Plane survey (HOPS; Walsh et al. 2011) finds approximately 10 other examples of comparable RRL regions in 100 square-degrees of the Galactic plane. Therefore, we proceed with the presence of H53α emission or an OH maser to discriminate young and evolved regions of star formation.

Non-evolved class I CH_3OH maser regions comprise 47 per cent of the total population, indicating that class I CH_3OH masers can occur over a broad span of time in star-forming regions. In the following text, we qualitatively discuss infrared associations with young class I CH_3OH masers. Images in Appendix C show the infrared environment of the detected masers. It can be seen that many masers are cospatial with dark infrared regions, presumably IRDCs, which are dense regions of cold gas projected in front of a bright background. IRDCs are known to host HMSF, thus it is not surprising to find a large population of class I CH_3OH masers towards these locations.

The three class I CH_3OH maser sites detected in auto- but not cross-correlated data are also within the young population. G331.72−0.20 and G333.24+0.02 appear to be associated with dark infrared regions, but G331.44−0.14 lacks any obvious infrared feature; it may be originating in an IRDC behind foreground emission, or an example of a region lacking star formation. At present, we are unable to explain why these sites were not detected in cross-correlation data based on their infrared associations; with a larger population, an explanation may become apparent.

Fig. 2 shows histograms of class I CH_3OH maser site spot counts with and without other star-formation tracers. Perhaps most interestingly, the comparison with OH masers suggests that class I CH_3OH maser sites with few spots (less than 5) are unlikely to be associated with an OH maser. To check the significance of this claim, as well as the similarity between the other populations, we have performed Kolmogorov–Smirnov (KS) tests. KS tests on the populations associated with and without OH masers, class II CH_3OH masers and H53α emission finds 1.2, 1.1 and 22 per cent probability that they are drawn from the same distribution, respectively. It seems that the number of detected class I CH_3OH maser spots is a good indication for the presence of other masers, but not necessarily the presence of RRL emission.

With only a few possible exceptions, each of the class I CH_3OH masers identified by MALT-45 appears to be associated with HMSF. As we find many maser sites without associated class II CH_3OH or OH masers or H53α emission, we appear to be identifying early stages of HMSF. Thus, class I CH_3OH masers can provide a useful means of identifying star formation, and further MALT-45 observations will find more young star-forming regions purely through maser emission. In addition to isolating a young population, this work has shown that the number of class I CH_3OH maser spots detected may be indicative of the evolutionary stage of the region, which further demonstrates the usefulness of this spectral line.

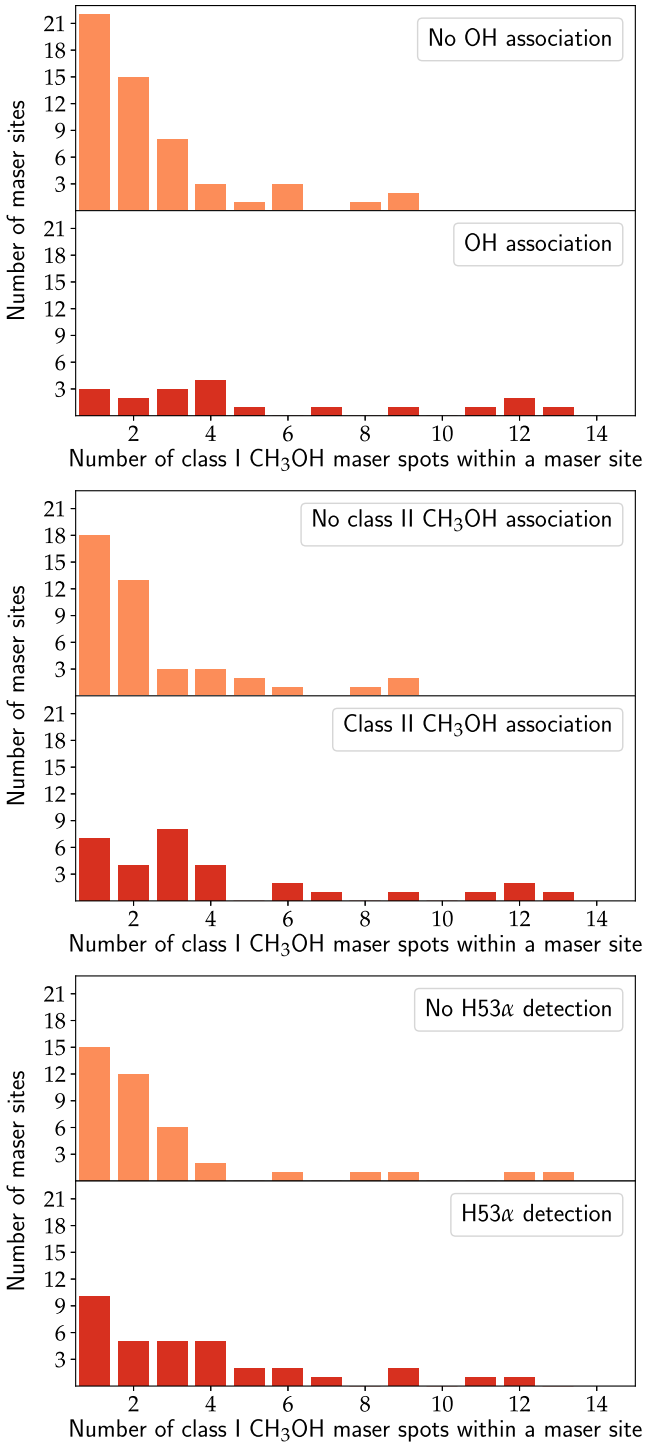

Figure 2. Histograms of class I CH_3OH maser spot counts within each maser region, highlighting associations with and without an OH maser, class II CH_3OH maser or H53α detection. The majority of class I CH_3OH maser regions with only one or two spots do not have an associated OH or class II CH_3OH maser, but there is a tendency for more associations in regions with more class I CH_3OH maser spots. A KS test on the samples with and without an OH maser association shows a 1.2 per cent probability that the two samples are drawn from the same population. The same KS test performed on class II CH_3OH maser and H53α detection samples have a 1.1 and 22 per cent probability, respectively.

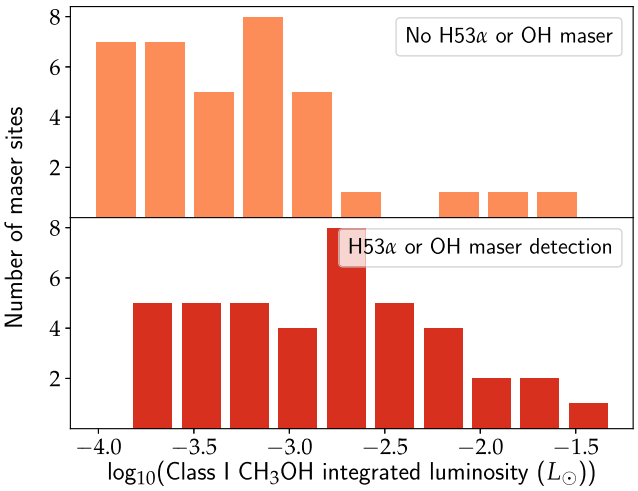

Figure 3. Luminosities of class I CH_3OH maser regions, associated with and without H53α emission or an OH maser. There are relatively few masers with high luminosities that are not associated with H53α emission or an OH maser. A KS test finds a 0.2 per cent chance that both samples are drawn from the same population.

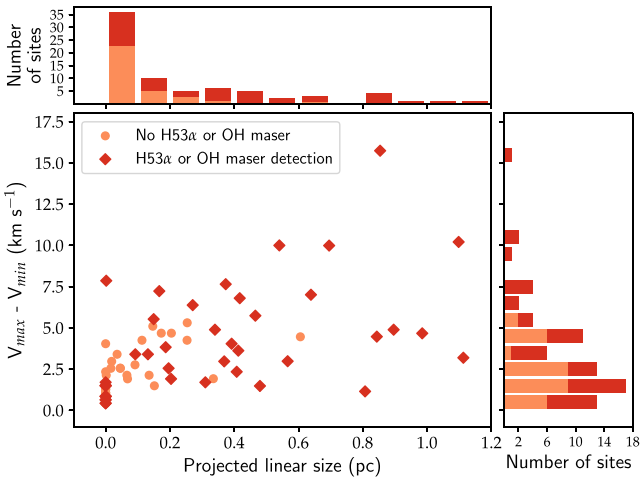

Figure 4. Projected linear sizes and velocity ranges of class I CH_3OH maser regions. The majority of maser regions have relatively small projected linear sizes and velocity ranges. Regions that are not evolved tend to have lower luminosities and smaller projected linear sizes and velocity ranges; KS tests suggest that the populations with and without H53α emission and/or an associated OH maser are distinct (see Section 4.2.2).

4.2 Properties of detected class I CH_3OH masers

4.2.1 Luminosities

Using the information gathered from these observations, we conduct analyses of the basic properties of class I CH_3OH masers. Fig. 3 shows the luminosities of these masers. Luminosities are determined from the integrated intensity of auto-correlated emission, calculated by Gaussian fits to maser spectra.

The histogram in Fig. 3 presents luminosities of class I CH_3OH masers, highlighting the populations associated with and without H53α emission or an OH maser. A KS test finds a 0.2 per cent chance that both samples are drawn from the same population. Using the presence of H53α emission or an OH maser as an indication for a relatively evolved region, this result suggests that the luminosity of class I CH_3OH masers can indicate the evolutionary stage of its host star-forming region.

4.2.2 Projected linear sizes and velocity ranges

Fig. 4 compares the projected linear sizes and velocity ranges of young and evolved class I CH_3OH maser regions. The projected linear size is calculated using the angular size of maser emission across a region and its derived kinematic distance (see Table 3). Velocity range simply refers to the difference between the most redshifted and blueshifted emissions within a single region. The majority of sources are confined to small projected linear sizes (<0.5 pc) and small-velocity ranges (<5 km s^{-1}). Of the maser sites that exceed these sizes and velocity ranges, relatively few are young. KS tests were performed on both young and evolved samples of projected linear sizes and velocities; the probability that each sample is drawn from the same distribution is $<10^{-1}$ per cent and 4.3 per cent, respectively, suggesting that these populations are distinct.

Voronkov et al. (2014) also analysed the projected linear sizes and velocity ranges of class I CH_3OH masers, but between populations with and without an associated OH maser. Here, we observe similarities between our two populations and theirs. Class I CH_3OH masers observed by Voronkov et al. (2014) without an associated OH maser are confined to relatively small projected linear sizes (<0.4 pc) and velocity ranges (<10 km s^{-1}) (Fig. 5 of their paper). In addition, when associated with an OH maser, Voronkov et al. (2014) find that the projected linear sizes and velocity ranges of class I CH_3OH maser sites are typically larger.

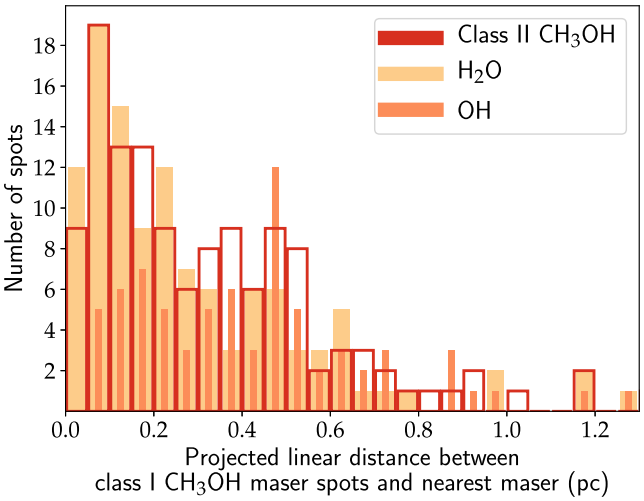

Figure 5. Histogram of the projected linear distance between every class I CH_3OH maser spot position and class II CH_3OH, OH and H_2O masers. This histogram uses the projected distance between masers only when their angular offset is less than 60 arcsec. The majority of projected linear distances to masers are within 0.5 pc.

While the projected linear sizes of our study and that of Voronkov et al. (2014) have similar values (up to 1 pc), the velocity ranges do not. The mean velocity ranges of our class I CH_3OH masers are 4.1 and 2.4 km s^{-1} for the evolved and young populations, respectively, while the Voronkov et al. (2014) with and without OH maser association are approximately 10 and 5 km s^{-1}, respectively. For comparison, the mean velocity range of our class I CH_3OH masers associated with a class II CH_3OH and OH maser is 5.3 km s^{-1}, whereas class II CH_3OH without OH is 3.2 km s^{-1}. This difference is likely due to the sample of class I CH_3OH masers used by Voronkov et al. (2014) being typically biased towards class II CH_3OH masers. The difference between this value and

that of Voronkov et al. (2014) might be due to our sample being more unbiased.

4.2.3 Spatial distributions

The spatial distributions of class I CH_3OH masers have been discussed in the literature. Kurtz et al. (2004) measured the distance between class I CH_3OH masers and H II regions, and Voronkov et al. (2014) compared the distance between class II and class I CH_3OH masers. For our class I CH_3OH maser regions featuring another type of star-formation maser (OH, class II CH_3OH or H_2O), a projected linear distance comparison is presented in Section 4.3.1. As we do not have a common object to compare within each maser site (such as an H II region or class II CH_3OH maser), we instead compare the maximum distance between any two maser spots within a site. Here, we briefly discuss the maximum spatial offset (projected linear size) between any two maser spots within a site (see Fig. 4).

Seven maser sites have a projected linear size greater than 0.8 pc; these sites are G330.876−0.362, G331.279−0.189, G331.492−0.082, G331.503−0.109, G331.530−0.099, G333.313+0.106 and G333.558−0.293. Upon inspection of the distribution of these masers with infrared maps, it is likely that not all the class I CH_3OH masers are related to a single high-mass object (see Appendix C). G330.876−0.362 has only two spots, very far from each other; one is closely associated with class II CH_3OH, H_2O and OH masers, the other with an infrared dark cloud (IRDC). G331.279−0.189 has a single maser spot very far from the rest of the relatively clustered spots, and may not be powered by a common source. G333.558−0.293 has only two maser spots; the infrared map shows what appears to be a different IRDC associated with each. G331.492−0.082, G331.503−0.109, G331.530−0.099 and G333.313+0.106 may be exceptions. There is no obvious infrared distinction between the maser spots of G331.492−0.082 to rule out a common source. The spots associated with both G331.503−0.109 and G331.530−0.099 may be powered by the same source located at G331.512−0.100, which also features H_2O and OH masers, as there are no other apparent infrared sources that could be powering either maser spot. Despite the large projected linear size, the spots associated with G333.313+0.106 appear to be associated with the same object, which also features an EGO and a class II CH_3OH maser.

While it is difficult to discern the origin of each maser spot from observations of maser emission alone, it seems that the large offsets between spots are not necessarily common, and may be erroneously generated by calculating a radius for each observed maser 'site'. While these masers are collisionally excited and therefore more likely to appear at large distances from their powering source, we suggest that genuine class I CH_3OH maser associations over large distances are uncommon. Perhaps the class I masers are tracing weak, continuous C-type shocks rather than powerful J-type shocks (Widmann et al. 2016); in addition, we might expect masers triggered by stronger shocks to have broader velocity ranges than those we observe.

4.3 Comparing class I CH_3OH masers with other masers and thermal lines

4.3.1 Separation from other maser species in star-forming regions

Section 4.2.3 is able to infer the age and size of host star-forming regions by simply using the properties of class I CH_3OH maser spots. Here, we compare the distances between class I CH_3OH maser spots and other maser species to determine the spatial extents of star-forming regions; this is prudent in conjunction with Section 4.2.3, as class II CH_3OH and OH masers are relatively near to their powering source.

The projected linear distances between every spot of a class I CH_3OH maser site and class II CH_3OH, OH and H_2O masers are presented in Fig. 5. The other star-formation maser positions were gathered from Caswell et al. (2011); Sevenster et al. (1997); Caswell (1998); Breen et al. (2010b); Walsh et al. (2011, 2014). A maser site was considered to be associated with a secondary maser site if the two were less than 60 arcsec from each other. If more than one of the same maser species is within 60 arcsec of a class I CH_3OH maser spot, only the closest was used for comparison.

Most projected linear distances are less than 0.5 pc. Kurtz et al. (2004) find that the distance between class I CH_3OH masers and H II regions tends to be within 0.5 pc, in agreement with our results. Voronkov et al. (2014) were able to model an exponential decay to the number of class I CH_3OH maser spots with distance from class II CH_3OH masers; with their larger sample size, they see many masers at projected linear distances beyond 0.5 pc. However, the vast majority are within 0.5 pc, also in agreement with our results. Given that our maser spots are derived from an unbiased sample, it seems that typical regions of HMSF power class I CH_3OH maser activity within a distance of 0.5 pc.

The majority of projected linear distances between class I CH_3OH maser spots and class II CH_3OH or H_2O masers are at small distances (<0.2 pc), whereas OH masers have a flat distribution out to approximately 0.5 pc. The similarity of the projected linear distances in each comparison can be determined with KS tests; the probabilities of each distribution being drawn from the same sample are $<10^{-1}$, $<10^{-1}$ and 49.0 per cent for OH and H_2O, OH and class II, and H_2O and class II, respectively. Thus, OH masers have significantly higher projected linear distances from class I CH_3OH masers compared to class II CH_3OH or H_2O masers.

In general, maser associations are well characterized within distances of 0.5 pc. We believe that most associations beyond 0.5 pc are also genuine, but we would require additional information to conclude otherwise.

4.3.2 Velocities

Paper I finds that class I CH_3OH masers are good tracers of systemic velocity; with these follow-up data, we repeat this type of analysis with more thermal lines, as well as class II CH_3OH maser emission. The peak velocities of class I CH_3OH masers in auto-correlated data are compared with class II CH_3OH masers, thermal CS, SiO and CH_3OH in Fig. 6. We discuss the resulting distributions in the following text.

Voronkov et al. (2014) used a large sample of class I and class II CH_3OH masers to investigate their relative velocities. Analysing the distribution of velocity differences between class I and class II CH_3OH masers, they find a peak velocity difference at $-0.57 \pm 0.07\,\mathrm{km\,s^{-1}}$ with a standard deviation of $3.32 \pm 0.07\,\mathrm{km\,s^{-1}}$ and a slight blueshifted asymmetry. The cause of the blueshift could not be attributed to either the class I or class II CH_3OH masers. As class II CH_3OH masers occur near to a YSO, their velocities are thought to be tracers of systemic velocities, albeit with a large dispersion (Szymczak, Bartkiewicz & Richards 2007; Green & McClure-Griffiths 2011). In the following discussion, we analyse the peak velocities of thermal lines observed in these data, and find that class I CH_3OH masers are significantly better tracers of systemic velocities than class II CH_3OH masers.

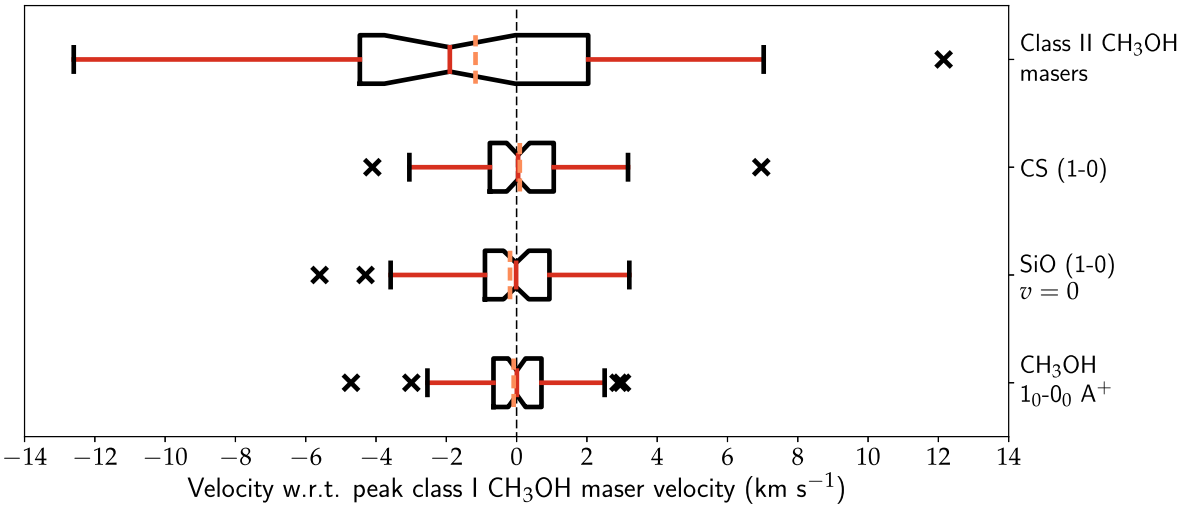

Figure 6. Notched box-and-whisker plot of peak velocity differences between class I CH_3OH masers and various species associated with star formation. The red solid vertical line within the boxes indicates the median, and the orange dashed lines indicate the mean. The notched region about the median indicates the 95 per cent confidence interval on the median, and the box covers the interquartile region (IQR; middle 50 per cent of data). Whiskers extend past the IQR by up to 1.5 × IQR. Black crosses indicate outlying data. The dashed black line indicates zero peak velocity difference. The class II CH_3OH maser box plot has a relatively wide range of velocity differences compared to the other lines. CS, SiO and thermal CH_3OH velocities are all closely associated with the maser velocity.

The distribution of velocity differences in Fig. 6, which compares class I and class II CH_3OH masers, has the statistics $\mu = -1.17 \pm 0.87\,\mathrm{km\,s^{-1}}$, $\tilde{x} = -1.90\,\mathrm{km\,s^{-1}}$ and $\sigma = 4.75 \pm 0.61\,\mathrm{km\,s^{-1}}$ (μ is the mean, $\tilde{x}$ the median and σ the standard deviation). The parameters of this comparison are consistent with that of Voronkov et al. (2014). The median and mean are also blueshifted, but unlike Voronkov et al. (2014), are statistically insignificant.

Paper I compared the peak velocities of CS (1–0) and class I CH_3OH masers where each maser was detected. From that work, the resulting statistics were $\mu = 0.0 \pm 0.2\,\mathrm{km\,s^{-1}}$, $\tilde{x} = -0.1\,\mathrm{km\,s^{-1}}$ and $\sigma = 1.5 \pm 0.1\,\mathrm{km\,s^{-1}}$. The results of the same comparison with these data corroborate that of Paper I: $\mu = 0.09 \pm 0.18\,\mathrm{km\,s^{-1}}$, $\tilde{x} = 0.04\,\mathrm{km\,s^{-1}}$ and $\sigma = 1.56 \pm 0.17\,\mathrm{km\,s^{-1}}$. Given that CS traces very dense gas ($n_c > 10^5\,\mathrm{cm^{-3}}$), the peak CS velocity is likely closely related to the systemic velocity of a molecular cloud. Hence, the statistics suggest that class I CH_3OH masers are also good tracers of systemic velocities. As CS emission can be quite bright in these data, it is possible that optically thick emission, if present, is causing uncertainty in the systemic velocity, and hence skews the distribution in Fig. 6. To help resolve this matter, we analysed the peak velocities of $C^{34}S$ emission. With only one exception, $C^{34}S$ was detected towards each observed class I CH_3OH region, and the peak velocity of $C^{34}S$ agrees with the peak CS velocity to within $0.5\,\mathrm{km\,s^{-1}}$ in each region. Therefore, we consider peak CS velocities as accurate systemic velocity tracers. Green & McClure-Griffiths (2011) compared the peak velocity of CS (2–1) and mid-velocity of class II CH_3OH maser emission, finding a mean and median velocity difference of 3.6 and $3.2\,\mathrm{km\,s^{-1}}$, respectively; their relatively large velocity differences corroborate our results for class II CH_3OH masers compared against class I CH_3OH masers.

The measured difference between SiO emission and class I CH_3OH maser velocities is similar to the difference between CS emission and class I CH_3OH maser velocities: $\mu = -0.19 \pm 0.21\,\mathrm{km\,s^{-1}}$, $\tilde{x} = -0.01\,\mathrm{km\,s^{-1}}$ and $\sigma = 1.65 \pm 0.15\,\mathrm{km\,s^{-1}}$. The distribution featuring SiO is slightly wider than that featuring CS, but we place less emphasis on this difference in line width, since the difference is small. Overall, the peak velocities of class I CH_3OH masers and SiO emission closely agree.

The differences in velocity between the peak velocity of the thermal 1_0–0_0 A^+ line of CH_3OH and class I CH_3OH masers also show a tight association: $\mu = -0.08 \pm 0.15\,\mathrm{km\,s^{-1}}$, $\tilde{x} = 0.01\,\mathrm{km\,s^{-1}}$ and $\sigma = 1.33 \pm 0.11\,\mathrm{km\,s^{-1}}$. As a sufficient abundance of CH_3OH gas is needed for maser emission, it is perhaps not surprising that the thermal velocity is closely matched to the maser velocity. Given the distribution relative to CS, it seems that thermal CH_3OH is also a good tracer of systemic velocities.

The differences in the peak velocity for the thermal CS, SiO and CH_3OH spectral lines all appear consistent with zero, with uncertainties of a couple of $\mathrm{km\,s^{-1}}$. The distribution featuring velocity differences using class II CH_3OH masers, however, is broad and has a relatively distinct mean and median blueshift. This hints that the peak velocity of class II CH_3OH masers tend to be blueshifted from the systemic velocity, although the statistics presented above only provide tentative evidence of this. One explanation of the blueshift is that the strongest class II CH_3OH masers in a region are preferentially detected in the foreground of star-forming regions rather than in the background. This preference may occur because at 6.7 GHz radio continuum free–free emission may be optically thick. This would be especially true for younger sources. The preference to see blueshifted class II CH_3OH masers could be explained by the masers occurring in an outflow or an expanding shell. But blueshifted masers are not easily explained if the masers occur in a circumstellar accretion disc.

4.3.3 *Brightness*

With a statistically complete sample of class I CH_3OH masers and enhanced sensitivity to auto-correlated emission, the observations of this work have the opportunity to identify relations, if any, between the luminosities of class I CH_3OH masers and other species associated with star formation. In this subsection, we use the auto-correlated integrated flux densities of class I CH_3OH maser

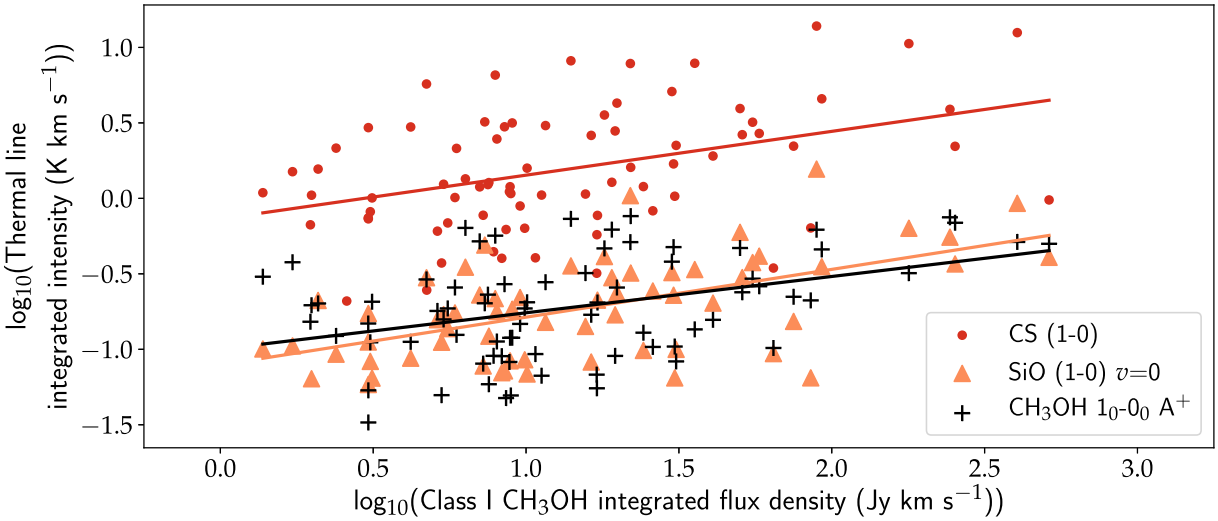

Figure 7. Integrated flux density scatter plots of CS, SiO and thermal CH_3OH against class I CH_3OH masers. All three comparisons show a similar trend, albeit with a large degree of scatter; the r values for the lines of best fit with CS, SiO and thermal CH_3OH are 0.41, 0.57 and 0.40, respectively.

emission to compare with the thermal CS, SiO and CH_3OH integrated intensities (see Fig. 7).

In each comparison, a similar positive trend exists, although the degree of scatter in each comparison is large. The r value for the CS comparison is 0.41.

SiO (1–0) $v = 0$ is typically thought to trace strongly shocked gas, particularly found in outflows. As class I CH_3OH masers are collisionally excited by weak shocks, they may be excited in regions also containing SiO emission. As discussed earlier, analyses with SiO were not possible in Paper I, due to the low detection rate and relatively weak intensities of SiO (1–0) $v = 0$. Consequently, Paper I speculates on the nature of the class I CH_3OH maser sites, given that the SiO detection rate was quite low (30 per cent). As the majority of regions now have confirmed SiO detections, it seems that a large portion of class I CH_3OH maser sites indeed have shocked gas associated with them. As bright SiO emission within these maser sites is rare, perhaps their faint intensities indicate weak shocks, similar to what was found by Widmann et al. (2016). The correlation coefficient (r value) between the integrated intensity of SiO and class I CH_3OH maser integrated flux density (IFD) is 0.57.

Similar to SiO, comparisons with thermal CH_3OH was not possible in Paper I. The correlation here is the weakest, with an r value of 0.40.

The correlation coefficient for each comparison indicates a moderate correlation. This, combined with a significant positive slope, indicates that brighter class I CH_3OH masers are more likely to be associated with brighter thermal lines. We might expect that higher-mass regions of star formation to contain more molecular gas, and thus the thermal line emission to be brighter. Given the moderate correlations between the brightness of class I CH_3OH masers and each of the thermal lines discussed in this section, class I masers may in turn hint at the mass of their host star-forming regions.

Class II CH_3OH masers have been found to be more luminous in more evolved regions of HMSF (Breen et al. 2010a); if there was a relationship between class I and class II CH_3OH masers, then the same might be true for class I CH_3OH masers. The luminosity of class I and class II CH_3OH masers was compared, but no correlation was observed, corroborating the results of Paper I. Due to class I CH_3OH masers being associated with more than one evolutionary phase on HMSF timeline, it is likely that a simple relationship between them and class II CH_3OH masers does not exist.

4.4 Comparing class I CH_3OH masers with 870 μm dust continuum from ATLASGAL

ATLASGAL surveyed 870 μm dust continuum emission across a large part of the Galactic plane ($330^\circ \leq l \leq 60^\circ$; Schuller et al. 2009), including the MALT-45 region. This sub-millimetre emission traces cold dust, which is optically thin, and can in turn be used to infer column densities and clump masses.

The catalogue of Contreras et al. (2013) provides the location and integrated flux densities of 870 μm dust continuum emission point sources. Using these, we can investigate relationships between class I CH_3OH masers and 870 μm emission, such as the brightness of each and the typical clump mass containing a maser site. We associated any class I CH_3OH masers and ATLASGAL clumps within an angular offset of 60 arcsec, to be consistent with the other maser associations, and list the associations in Table 3. Only 4 of our 77 maser regions lack an association with an 870 μm clump (5 per cent).

4.4.1 Separation between ATLASGAL 870 μm dust clumps and class I CH_3OH maser spots

Section 4.3.1 analyses the distances between class I CH_3OH masers and other masers associated with star formation; here, we analyse how class I masers compare against point sources of dust continuum.

Histograms of projected linear distances between class I CH_3OH maser spots and 870 μm clumps are provided in Fig. 8. The majority of maser spots are within 0.4 pc of an ATLASGAL source, but the more evolved maser distribution has a long tail down to approximately 1.2 pc. Quantified with a KS test, we find a 2.4 per cent probability that both samples are drawn from the same population. This is similar to the projected linear distances between class I CH_3OH maser spots and OH masers shown in Fig. 5, and may be due to the same effect: evolved regions of star formation are more likely to affect a greater volume than younger ones.

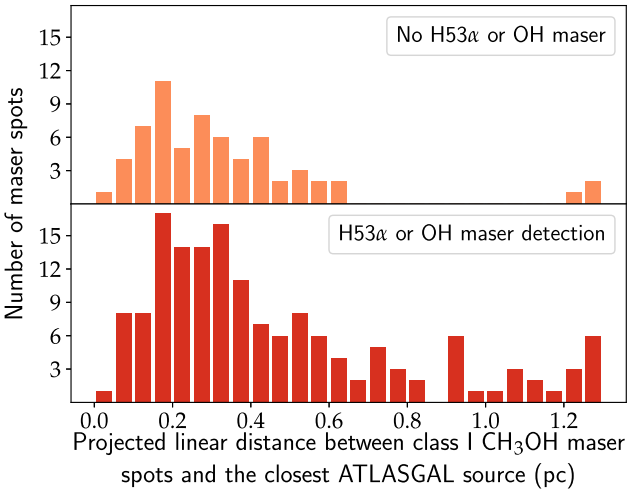

Figure 8. Histograms of offsets between ATLASGAL clumps and class I CH_3OH maser spots, for young and evolved regions. The majority of associations have projected linear distances less than 0.4 pc, and almost all are within 0.6 pc. This indicates a strong relation between the region containing the ATLASGAL source and class I CH_3OH maser emission. A small population also exists with projected linear distances larger than 1 pc. Note that for each class I CH_3OH maser spot, if multiple ATLASGAL sources are present within 60 arcsec, only the closest was used.

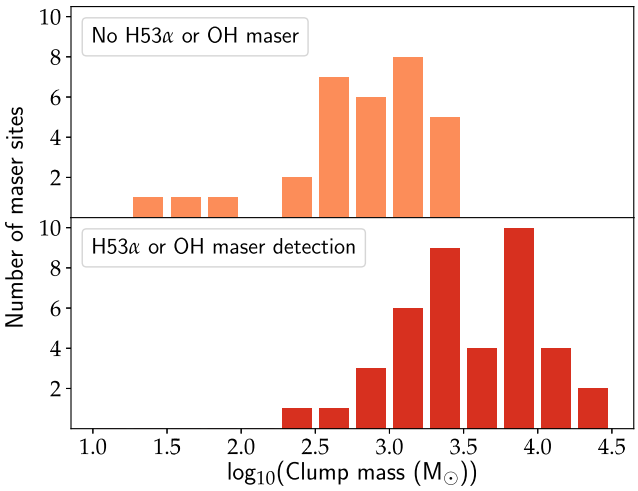

Figure 9. Histograms of clump masses associated with class I CH_3OH masers, determined by using 870 μm ATLASGAL dust continuum, for young and evolved populations. The mean mass of the young distribution is $10^{3.0}\,M_\odot$, whereas the mean mass of the evolved distribution is $10^{3.74}\,M_\odot$. The highest mass values are restricted to evolved masers regions, while the lowest masses are all young maser regions.

Note that Fig. 8 includes any ATLASGAL clump within 60 arcsec of a maser spot. Maser sites without ATLASGAL associations are discussed in Section 4.4.4.

4.4.2 Masses

It is useful to compare the properties of class I CH_3OH masers against the mass of their host star-forming regions. Chen et al. (2012) and Urquhart et al. (2013) estimate clump masses from the integrated intensity of millimetre-wavelength continuum emission, assuming that the emission is optically thin. In the same manner, we use ATLASGAL data to estimate clump masses via:

$$M_{\rm gas} = \frac{S_\nu D^2 R_d}{\kappa_d B_\nu (T_{\rm dust})} \quad (1)$$

where $M_{\rm gas}$ is the mass of the gas, S_ν is the integrated flux density of ATLASGAL 870 μm emission, D is distance to the maser, R_d is the ratio of gas and dust masses, κ_d is the mass-absorption coefficient per unit mass of dust and $B_\nu(T_{\rm dust})$ is the Planck function at temperature $T_{\rm dust}$. Urquhart et al. (2013) justify the choice of $T_{\rm dust} = 20$ K and $\kappa_d = 1.85\,{\rm cm^2\,g^{-1}}$, which we also use here. We also assume $R_d = 100$. The assumption of a single dust temperature is not realistic, but in the absence of temperature measurements towards every individual region, is necessary. Pandian, Wyrowski & Menten (2012) find the kinetic temperatures of gas in regions with class II CH_3OH masers, determined by NH_3 observations, have mean and median values of 26 and 23.4 K, respectively. Urquhart et al. (2011) also find mean and median temperatures towards high-mass YSOs to be 22.1 and 21.4 K, respectively. If we instead assume a dust temperature of 25 K, masses will decrease to 73 per cent of those determined with 20 K. Using a temperature of 15 K increases masses by 56 per cent relative to the 20 K masses. These uncertainties are comparable to those given by the kinematic distances. The histogram of masses can be seen in Fig. 9.

Class I CH_3OH masers appear to be associated with a wide range of clump masses ($10^{1.25} < \frac{M}{M_\odot} < 10^{4.5}$). Urquhart et al. (2013) associate 870 μm dust continuum emission with class II CH_3OH masers, and calculate clump masses. They find that clump masses associated with class II CH_3OH masers can range from $10^{-2} < \frac{M}{M_\odot} < 10^{6}$. As clump mass is consistent with that of Urquhart et al. (2013), and all class II CH_3OH masers are associated with HMSF, the lower end of these clump masses cannot necessarily serve as an indication of low-mass star formation regions.

Fig. 8 shows a difference in the calculated mass range for clumps associated with H53α emission or an OH maser; however, this difference is consistent with the sources we expect to be less evolved (clumps not associated with H53α emission or an OH maser) to be at a lower temperature than assumed 20 K. Other small contributions to this mass discrepancy may be attributable to a slight bias in the detectability of H53α whereby higher-mass objects are more likely to have detectable H53α emission at slightly younger age, or the possibility of genuine associations with low-mass stars. A KS test shows that the probability that both histograms are drawn from the same distribution is $<10^{-1}$ per cent.

4.4.3 Brightness

Fig. 10 compares the IFD of 870 μm ATLASGAL dust continuum clumps and the luminosity of class I CH_3OH masers, but only a weak correlation exists. Chen et al. (2012) performed a similar comparison using 95 GHz class I CH_3OH masers towards Bolocam Galactic Plane Survey (BGPS) sources of 1.1 mm thermal dust emission (Fig. 6 of their paper). They find a strong correlation between the maser luminosity and clump mass, with an r value of 0.84 and a p value of 8.1×10^{-13}. Our line of best fit has the coefficients $r = 0.33$, $p = 5.7 \times 10^{-3}$, and is shown on Fig. 10. The large difference between correlation coefficients may be attributed to the Chen et al. (2012) sample of BGPS sources being selected based on their GLIMPSE colours, which is likely biasing their statistics. On the other hand, given that the relationship between 44 and 95 GHz class I CH_3OH masers is well established (Val'tts et al. 2000), our lack of correlation observed may highlight differences between 870 μm and 1.1 mm emission, with 1.1 mm emission originating from more evolved regions. More data are necessary to establish

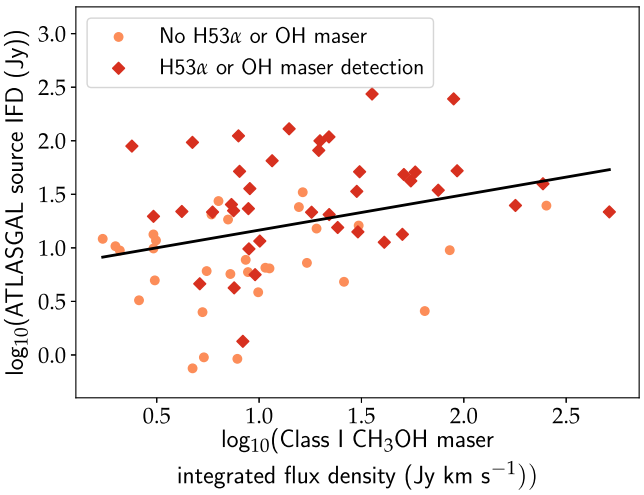

Figure 10. Scatter plot of ATLASGAL 870 μm dust continuum emission and class I CH_3OH maser integrated flux densities. The line of best fit for all data (young and evolved) is shown and has an r value of 0.33.

a connection between class I CH_3OH masers (44 and 95 GHz, to eliminate biases) and dust continuum emission. In particular, finding more 44 GHz class I CH_3OH masers towards sources with the same GLIMPSE colours selected by Chen et al. (2012) would help to eliminate biases.

Here, our correlation coefficient of 0.33 is not much weaker than those found in our comparisons of thermal lines to class I CH_3OH masers (0.41, 0.57 and 0.40 for CS, SiO and thermal CH_3OH, respectively) in Section 4.3.3. In that section, we speculate that the brightness of the thermal lines is proportional to mass; indeed, a comparison between the integrated intensity of CS and the IFD 870 μm dust continuum emission has a correlation coefficient of 0.84. As the brightness of dust continuum emission is directly proportional to mass, the result in this section strengthens the notion that the brightness of class I CH_3OH masers can hint at the mass of their host star-forming regions.

4.4.4 Class I CH_3OH maser sites without an ATLASGAL source

Only four class I CH_3OH maser regions are without an ATLASGAL point source classified by Contreras et al. (2013): G331.371−0.145, G331.442−0.158, G333.772−0.010 and G333.818−0.303. Using the data provided by the ATLASGAL team, we are able to investigate the 870 μm emission in each of these regions. Within ∼12 arcsec, G331.371−0.145, G331.442−0.158 and G333.818−0.303 each have peak 870 μm flux densities of 0.41, 0.63 and 0.23 Jy beam^{-1}, respectively. The ATLASGAL 1σ sensitivity over the MALT-45 area is approximately 60 mJy beam^{-1}. Point sources were classified by the source extraction algorithm SExtractor. Despite the pixel values of 870 μm dust emission towards these three maser sites are at least 3σ, SExtractor has most likely not been satisfied with a spatial morphology criterion. However, we do consider the 870 μm emission at these locations to be genuine. For these three regions, we determine the IFD of 870 μm emission to be 0.57, 0.28 and 0.24 Jy, respectively. Using equation (1), these values correspond to clump masses of 85, 40 and 15 $M_\odot$, respectively. These masses are relatively low compared to those discussed in Section 4.4, but even lower masses were determined from integrated flux densities in the ATLASGAL catalogue.

G333.772−0.010 has a single pixel of 870 μm dust continuum emission with a peak flux density of 0.25 Jy beam^{-1} at a projected linear distance of ∼27 arcsec. However, unlike the other regions of 870 μm emission, nearby pixels are relatively dim (<0.14 Jy beam^{-1}, <∼2σ), indicating that this pixel is likely a random noise spike. For sources at a similar distance (∼5.2 kpc), we might expect to see a similar distribution of 870 μm emission, but this is not the case. The class I CH_3OH maser emission is closely associated with compact infrared emission. Interestingly, the maser emission is strong (peak of 17.7 Jy, IFD of 11.7 Jy km s^{-1}), but the thermal lines are weak (the integrated intensity of CS and thermal CH_3OH are 0.319 and 0.057 K km s^{-1}, respectively, and no SiO is detected). Since Urquhart et al. (2015) do not detect an ATLASGAL counterpart towards approximately 7 per cent of class II CH_3OH masers from the MMB, we may have a similar example of star formation without a significant dust detection.

4.5 Comparing class I CH_3OH masers in cross- and auto-correlation

Minier, Booth & Conway (2002) and Bartkiewicz, Szymczak & van Langevelde (2014) discuss class II CH_3OH maser emission detected by very-long-baseline interferometry and single-dish/auto-correlation observations. These comparisons between cross- and auto-correlation data reveal a significant amount of resolved-out flux density; Bartkiewicz et al. (2014) report between 24 and 86 per cent. Naturally, an interferometer will resolve out any extended emission relative to the synthesized beam. The authors elaborate that the 'missing flux' is not dependent on distance, and that lower-resolution cross-correlation data have similar compact structures. This suggests that missing emission is quite diffuse, and is seemingly independent of the properties of compact maser emission. Minier et al. (2002) also attribute missing flux as being due to diffuse emission.

While these investigations were exclusively focused on class II CH_3OH masers, the observations detailed in this paper are able to undertake a similar investigation for class I CH_3OH masers. It is worth noting that the observations of Minier et al. (2002) and Bartkiewicz et al. (2014) have a resolution approximately two orders of magnitude better than ours. They find that class II CH_3OH maser emission is partially resolved on 100 km baselines, or longer. This is equivalent to a baseline length of approximately 15 km at 44 GHz. Since we note significantly reduced flux densities on MALT-45 baselines of 6 km or less, this implies that the 44 GHz CH_3OH emission regions are on typically larger scales than the 6.7 GHz CH_3OH regions.

Auto-correlation spectra for the CH_3OH masers were extracted using the method discussed in Section 2.1.2. Cross-correlation spectra were then plotted with their corresponding auto-correlation spectrum; three example regions are shown in Fig. 11. With the 1.5A array configuration for the ATCA, the maximum detectable scale of the cross-correlation data for these follow-up observations is approximately 4.6 arcsec.

The relative strength of compact maser emission to diffuse emission of a class I CH_3OH maser region was assessed by computing the ratio of cross-correlation IFD to auto-correlation IFD, i.e. if the cross-correlation IFD closely matches the auto-correlation IFD, the emission is compact. Fig. 11 shows a large variation in missing flux density is across several regions. We analysed the ratios of cross-correlated IFDs to auto-correlated IFDs, but no trends are apparent for evolved, young or total populations. The ratio of cross-correlated IFD to auto-correlated IFD was also compared against

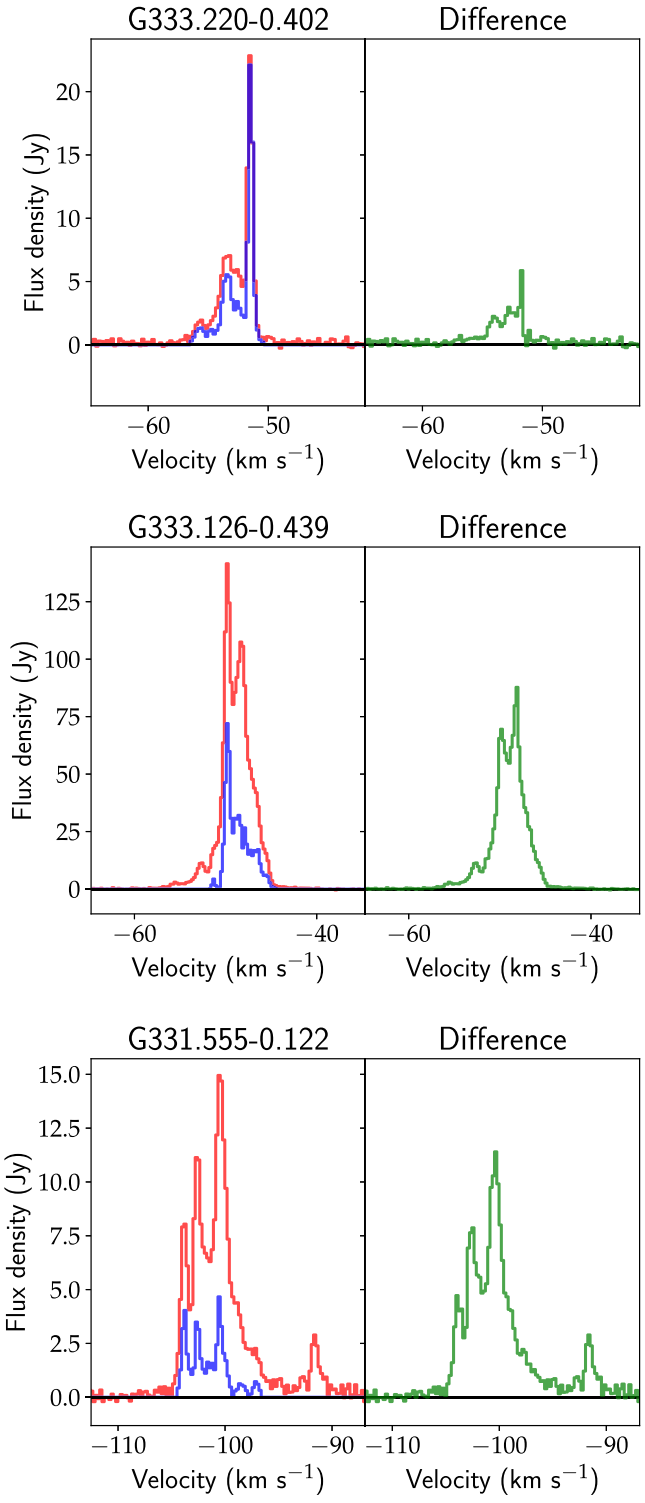

Figure 11. Cross- and auto-correlation spectra of three class I CH_3OH maser regions, with strong, moderate and weak maser strengths. Auto-correlation spectra are plotted red, cross-correlation spectra blue and the difference green.

the flux density of the masers, but no trend was observed. Class I CH_3OH emission can be strongly confined to compact structures (cross-correlated emission $\approx$ auto-correlated emission), extended (auto-correlated emission $\gg$ cross-correlated emission) or a combination of the two. This may explain why three targeted sites were not detected in the cross-correlation data set (G331.44−0.14, G331.72−0.20 and G333.24+0.02); their 44 GHz emission is likely too extended and lacks any bright, compact maser components.

To test if compact or diffuse regions can be separated, populations were investigated with and without various maser associations. These associations included class II CH_3OH, H_2O and OH masers, but no dependence was found for the proportion compact to diffuse maser emission with and without these associations. This proportion of compact to diffuse emission was also compared with thermal line integrated intensities in CS (1–0), SiO (1–0) $v = 0$ and CH_3OH 1_0–0_0 (see Fig. 12). A similar trend can be seen in each comparison; the r values for CS, SiO and thermal CH_3OH are −0.55, −0.38 and −0.45, respectively. The corresponding p values are 3.3×10^{-7}, 2.7×10^{-3} and 7.7×10^{-5}, respectively. These statistics suggest that our lines of best fit are significant.

Any indication of class I CH_3OH emission being dominated by compact components appears to be an intrinsic property of class I masers, but with a significant scatter amongst the sources. Another star formation tracer may reveal a correlation with the property of maser strength discussed here. Further observations of class I CH_3OH maser regions with better sensitivity and zero-spacing data will also help to identify weaker, more diffuse cross-correlation emission, in order to better understand the relationship between the diffuse and compact components of the CH_3OH maser emission.

5 SUMMARY AND CONCLUSIONS

We have extracted high-resolution positions, flux densities and velocities for class I methanol masers detected in the MALT-45 survey, and presented various properties for each observed region. The unbiased population from MALT-45 provides the first opportunity to assess class I methanol masers in a sensitivity-limited sample that are free from target selection biases, such as class II methanol masers or extended green objects. In addition, the thermal lines mapped by MALT-45 were observed with better sensitivity towards each maser site, providing more detail about the regions containing the class I methanol masers. We have determined:

(i) Class I methanol maser sites with fewer spots of emission are less likely to be associated with a class II methanol or hydroxyl maser.

(ii) Class I methanol masers without an associated hydroxyl maser or RRL emission have lower luminosities.

(iii) The spatial extent and velocity range of class I methanol masers is typically small (<0.5 pc and <5 km s^{-1}, respectively), particularly for those without an associated class II methanol or hydroxyl maser.

(iv) Class I methanol masers are generally located within 0.5 pc of a class II methanol or hydroxyl maser, but can be up to 0.8 pc away.

(v) Class I methanol masers are reliable tracers of systemic velocities, and are better than class II methanol masers.

(vi) The brightness of class I methanol masers is weakly correlated with the brightness of the thermal CS (1–0), SiO (1–0) $v = 0$ and CH_3OH 1_0–0_0 lines, as well as 870 μm dust continuum emission from ATLASGAL. These results suggest that the brightness of a class I methanol maser is proportional to the mass of its host star-forming region.

(vii) Class I methanol masers have high association rates with 870 μm dust continuum point sources catalogued by ATLASGAL, with typical offsets not exceeding 0.4 pc.

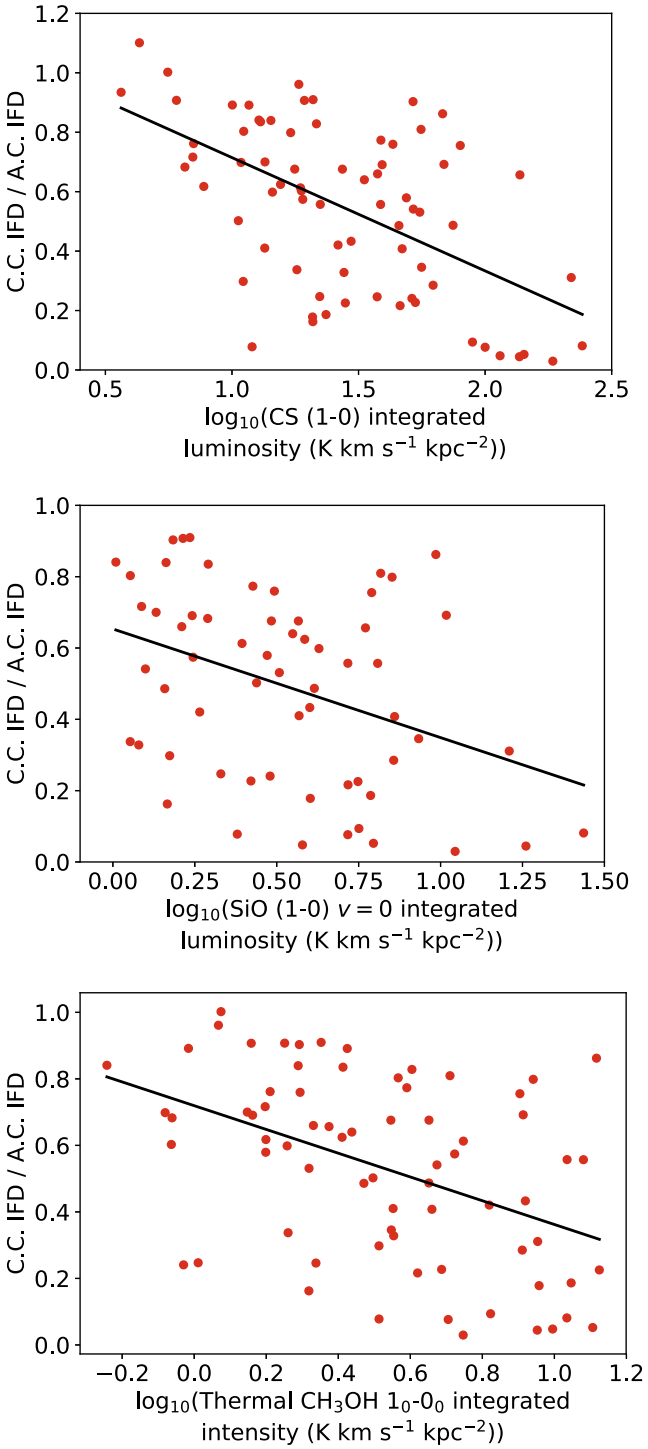

Figure 12. Scatter plots of the ratio of cross-correlation integrated flux density (C.C. IFD) to auto-correlation (A.C.) IFD against the thermal integrated intensity of CS, SiO and CH_3OH. The solid line represents the least squares fit. A similar, weak trend appears for all lines, but the large scatter hampers correlation (r values of −0.55, −0.38 and −0.45, respectively). The single datum with a larger C.C. IFD than A.C. IFD has an overcontribution of cross-correlation emission, due to spectral blending in nearby maser spots.

(viii) Class I methanol masers are found towards a large range of clump masses ($10^{1.25}$–$10^{4.5}$ $M_\odot$), but peak between $10^{3.0}$ and $10^{3.5}$ $M_\odot$. Additionally, masers associated with clump masses between $10^{3.25}$ and $10^{4.5}$ $M_\odot$ are almost all evolved regions of star formation;

(ix) The amount of diffuse emission in the 44 GHz class I methanol transition varies from source to source, but appears to increase as the brightness of thermal lines increases.

ACKNOWLEDGEMENTS

Parts of this research were conducted by the Australian Research Council Centre of Excellence for All-sky Astrophysics (CAASTRO), through project number CE110001020. The Australia Telescope Compact Array is part of the Australia Telescope National Facility, which is funded by the Commonwealth of Australia for operation as a National Facility managed by CSIRO. Shari Breen is the recipient of an Australian Research Council DECRA Fellowship (project number DE130101270). This research has made use of NASA's Astrophysics Data System Bibliographic Services, and the SIMBAD data base, operated at CDS, Strasbourg, France. Computation was aided by the NUMPY (Walt, Colbert & Varoquaux 2011), SCIPY (Jones et al. 2001) and ASTROPY (Astropy Collaboration et al. 2013) libraries. Figures were generated with MATPLOTLIB (Hunter 2007). Some figures in this paper use colours from www.ColorBrewer.org (Brewer 2017). The MIRIAD[1] software suite is managed and maintained by CSIRO Astronomy and Space Science.

REFERENCES

Astropy Collaboration et al., 2013, A&A, 558, A33
Bains I. et al., 2006, MNRAS, 367, 1609
Bartkiewicz A., Szymczak M., van Langevelde H. J., 2014, A&A, 564, A110
Benjamin R. A. et al., 2003, PASP, 115, 953
Breen S. L., Ellingsen S. P., Caswell J. L., Lewis B. E., 2010a, MNRAS, 401, 2219
Breen S. L., Caswell J. L., Ellingsen S. P., Phillips C. J., 2010b, MNRAS, 406, 1487
Breen S. L., Ellingsen S. P., Contreras Y., Green J. A., Caswell J. L., Stevens J. B., Dawson J. R., Voronkov M. A., 2013, MNRAS, 435, 524
Brewer C. A., 2017, www.ColorBrewer.org
Caswell J. L., 1997, MNRAS, 289, 203
Caswell J. L., 1998, MNRAS, 297, 215
Caswell J. L. et al., 2011, MNRAS, 417, 1964
Chen X. et al., 2012, ApJS, 200, 5
Chen X., Ellingsen S. P., Baan W. A., Qiao H.-H., Li J., An T., Breen S. L., 2015, ApJ, 800, L2
Contreras Y. et al., 2013, A&A, 549, A45
Cragg D. M., Johns K. P., Godfrey P. D., Brown R. D., 1992, MNRAS, 259, 203
Cyganowski C. J. et al., 2008, AJ, 136, 2391
Dawson J. R. et al., 2014, MNRAS, 439, 1596
Ellingsen S. P., 2006, ApJ, 638, 241
Ellingsen S. P., Breen S. L., Voronkov M. A., Dawson J. R., 2013, MNRAS, 429, 3501
Ellingsen S. P., Chen X., Qiao H.-H., Baan W., An T., Li J., Breen S. L., 2014, ApJ, 790, L28
Fujiyoshi T., Smith C. H., Caswell J. L., Moore T. J. T., Lumsden S. L., Aitken D. K., Roche P. F., 2006, MNRAS, 368, 1843
Green J. A., McClure-Griffiths N. M., 2011, MNRAS, 417, 2500
Green J. A. et al., 2012, MNRAS, 420, 3108

[1] http://www.atnf.csiro.au/computing/software/miriad/

Hunter J. D., 2007, Computing In Science & Engineering, 9, 90
Jones E., Oliphant T., Peterson P. et al., 2001, http://www.scipy.org/
Jordan C. H., Walsh A. J., Lowe V., Lo N., Purcell C. R., Voronkov M. A., Longmore S. N., 2013, MNRAS, 429, 469
Jordan C. H. et al., 2015, MNRAS, 448, 2344
Kalenskii S. V., Johansson L. E. B., Bergman P., Kurtz S., Hofner P., Walmsley C. M., Slysh V. I., 2010, MNRAS, 405, 613
Kurtz S., Hofner P., Álvarez C. V., 2004, ApJS, 155, 149
Lilley A. E., Palmer P., 1968, ApJS, 16, 143
McEwen B. C., Pihlström Y. M., Sjouwerman L. O., 2014, ApJ, 793, 133
Menten K. M., 1991, ApJ, 380, L75
Minier V., Booth R. S., Conway J. E., 2002, A&A, 383, 614
Minier V., Ellingsen S. P., Norris R. P., Booth R. S., 2003, A&A, 403, 1095
Müller H. S. P., Schlöder F., Stutzki J., Winnewisser G., 2005, J. Mol. Struct., 742, 215
Müller H. S. P., Spezzano S., Bizzocchi L., Gottlieb C. A., Degli Esposti C., McCarthy M. C., 2013, J. Phys. Chem. A, 117, 13843
Nguyen-Lu'o'ng Q. et al., 2013, ApJ, 775, 88
Pandian J. D., Wyrowski F., Menten K. M., 2012, ApJ, 753, 50
Partridge B., López-Caniego M., Perley R. A., Stevens J., Butler B. J., Rocha G., Walter B., Zacchei A., 2016, ApJ, 821, 61
Pihlström Y. M., Sjouwerman L. O., Frail D. A., Claussen M. J., Mesler R. A., McEwen B. C., 2014, AJ, 147, 73
Qiao H.-H. et al., 2016, ApJS, 227, 26
Reid M. J. et al., 2009, ApJ, 700, 137
Sault R. J., Teuben P. J., Wright M. C. H., 1995, in Shaw R. A., Payne H. E., Hayes J. J. E., eds, ASP Conf. Ser. Vol. 77, Astronomical Data Analysis Software and Systems IV. Astron. Soc. Pac., San Francisco, p. 433
Schuller F. et al., 2009, A&A, 504, 415
Sevenster M. N., Chapman J. M., Habing H. J., Killeen N. E. B., Lindqvist M., 1997, A&AS, 124, 509
Szymczak M., Bartkiewicz A., Richards A. M. S., 2007, A&A, 468, 617
Urquhart J. S. et al., 2010, PASA, 27, 321
Urquhart J. S. et al., 2011, MNRAS, 418, 1689
Urquhart J. S. et al., 2013, MNRAS, 431, 1752
Urquhart J. S. et al., 2015, MNRAS, 446, 3461
Val'tts I. E., Ellingsen S. P., Slysh V. I., Kalenskii S. V., Otrupcek R., Larionov G. M., 2000, MNRAS, 317, 315
Voronkov M. A., Caswell J. L., Ellingsen S. P., Sobolev A. M., 2010a, MNRAS, 405, 2471
Voronkov M. A., Caswell J. L., Britton T. R., Green J. A., Sobolev A. M., Ellingsen S. P., 2010b, MNRAS, 408, 133
Voronkov M. A., Caswell J. L., Ellingsen S. P., Green J. A., Breen S. L., 2014, MNRAS, 439, 2584
Walsh A. J., Burton M. G., Hyland A. R., Robinson G., 1998, MNRAS, 301, 640
Walsh A. J., Bertoldi F., Burton M. G., Nikola T., 2001, MNRAS, 326, 36
Walsh A. J., Macdonald G. H., Alvey N. D. S., Burton M. G., Lee J.-K., 2003, A&A, 410, 597
Walsh A. J. et al., 2011, MNRAS, 416, 1764
Walsh A. J., Purcell C. R., Longmore S. N., Breen S. L., Green J. A., Harvey-Smith L., Jordan C. H., Macpherson C., 2014, MNRAS, 442, 2240
Walt S. v. d., Colbert S. C., Varoquaux G., 2011, Comput. Sci. Eng., 13, 22
Widmann F., Beuther H., Schilke P., Stanke T., 2016, A&A, 589, A29

APPENDIX A: GAUSSIAN SPECTRAL FITS TO CROSS-CORRELATION CLASS I CH_3OH MASER EMISSION

Table A1. Gaussian fits for the spectra of class I CH_3OH maser spots. Column 1 lists the maser spot name, along with a letter designating the spot. Spots labelled with an asterisk (∗) have been manually fitted as these spots appear close to a bright neighbour; see Section 2.1.1. Columns 2 and 3 list the fitted position for the Gaussian. Columns 4 through 6 list the fitted Gaussian parameters. Note that the uncertainty for each parameter is quoted in parentheses, in units of the least significant figure. Column 7 lists the integrated flux density of the Gaussian. Rows without spot names correspond to a second Gaussian fitted to the spot directly above.

Spot name	α_{2000} (h:m:s)		δ_{2000} (°:′:″)		Peak flux density (Jy)		Peak velocity ($km\,s^{-1}$)		FWHM ($km\,s^{-1}$)		Integrated flux density ($Jy\,km\,s^{-1}$)
G330.2940−0.3921A	16:07:37.51	(5)	−52:30:56.1	(2)	1.00	(4)	−80.13	(2)	0.90	(4)	0.679
G330.2945−0.3943A	16:07:38.24	(4)	−52:31:00.5	(1)	0.52	(3)	−77.55	(2)	0.93	(5)	0.363
G330.6780−0.4023A	16:09:31.70	(5)	−52:15:50.7	(1)	1.73	(6)	−64.78	(1)	0.78	(3)	1.015
G330.7790+0.2488A	16:07:09.75	(3)	−51:42:53.76	(5)	0.72	(2)	−43.227	(6)	0.57	(1)	0.308
G330.8749−0.3557A	16:10:15.99	(6)	−52:05:46.6	(1)	14.3	(1)	−61.284	(2)	0.476	(5)	5.120
G330.8774−0.3676A	16:10:19.8	(1)	−52:06:12.1	(2)	2.4	(1)	−58.06	(2)	0.84	(5)	1.519
G330.8711−0.3830A	16:10:22.13	(8)	−52:07:08.23	(9)	0.85	(6)	−58.10	(4)	1.08	(8)	0.690
G330.8711−0.3830B	16:10:22.1	(1)	−52:07:08.3	(1)	0.77	(5)	−62.86	(3)	0.89	(7)	0.513
					0.51	(4)	−64.50	(8)	2.2	(2)	0.340
G330.9261−0.4083A	16:10:44.6	(2)	−52:06:00.37	(4)	11.8	(4)	−42.36	(1)	0.66	(2)	5.877
					1.2	(2)	−41.37	(5)	0.7	(1)	0.598
G330.9274−0.4072A	16:10:44.723	(9)	−52:05:54.29	(9)	1.9	(1)	−41.41	(2)	0.52	(4)	0.744
G330.9304−0.2602A	16:10:06.61	(4)	−51:59:18.5	(1)	3.9	(1)	−90.00	(1)	0.91	(3)	2.675
G330.9311−0.2605A	16:10:06.87	(6)	−51:59:17.78	(5)	3.94	(8)	−89.014	(5)	0.50	(1)	1.480
G330.9548−0.1823A	16:09:52.99	(5)	−51:54:52.8	(2)	1.55	(6)	−93.66	(1)	0.57	(3)	0.670
G331.1308−0.4696A	16:11:59.38	(9)	−52:00:19.5	(2)	0.78	(5)	−68.94	(2)	0.59	(5)	0.346
G331.1308−0.4698A	16:11:59.4	(1)	−52:00:20.24	(5)	2.6	(1)	−67.45	(3)	1.47	(8)	2.876
G331.1336−0.4882A	16:12:05.14	(2)	−52:01:01.37	(5)	3.13	(6)	−67.911	(4)	0.459	(9)	1.082
G331.1308−0.2441A	16:10:59.53	(2)	−51:50:25.79	(4)	13.0	(6)	−87.50	(3)	1.45	(7)	14.148
G331.1308−0.2441B	16:10:59.54	(6)	−51:50:25.72	(5)	21	(4)	−90.1	(1)	1.6	(3)	24.901
G331.1308−0.2441C	16:10:59.54	(6)	−51:50:25.68	(9)	93	(3)	−91.11	(1)	0.93	(3)	65.276
G331.1333−0.2458A	16:11:00.7	(5)	−51:50:23.97	(6)	45	(1)	−88.531	(8)	0.70	(2)	23.769
G331.1333−0.2410A	16:10:59.41	(2)	−51:50:11.8	(1)	23.1	(2)	−84.630	(2)	0.610	(5)	10.604
G331.1333−0.2410B	16:10:59.45	(2)	−51:50:11.64	(2)	2.9	(1)	−86.19	(1)	0.53	(3)	1.151
G331.1322−0.2454A	16:11:00.25	(6)	−51:50:25.71	(1)	6.5	(2)	−84.34	(1)	0.81	(3)	3.986
G331.1322−0.2454B	16:11:00.29	(4)	−51:50:26.0	(1)	6.3	(2)	−87.667	(8)	0.47	(2)	2.244
G331.1332−0.2407A	16:10:59.30	(4)	−51:50:10.90	(3)	2.11	(6)	−85.718	(8)	0.59	(2)	0.931
G331.1313−0.2434A	16:10:59.499	(9)	−51:50:22.76	(5)	4.19	(7)	−86.097	(3)	0.412	(7)	1.300
G331.1315−0.2441A	16:10:59.73	(8)	−51:50:24.2	(1)	0.90	(5)	−82.85	(2)	0.57	(4)	0.386
G331.1313−0.2451A	16:10:59.9	(2)	−51:50:27.2	(2)	0.89	(7)	−82.53	(4)	0.91	(8)	0.610
G331.1329+0.1560A	16:09:15.03	(5)	−51:32:42.42	(7)	1.03	(9)	−78.36	(3)	0.66	(7)	0.509
G331.1339+0.1569A	16:09:15.07	(6)	−51:32:37.79	(4)	1.42	(3)	−78.336	(8)	0.72	(2)	0.768
G331.1348+0.1562A	16:09:15.50	(2)	−51:32:37.3	(1)	10.0	(3)	−77.19	(1)	0.77	(3)	5.760
G331.1332+0.1565A	16:09:15.00	(7)	−51:32:40.5	(1)	76	(1)	−75.532	(5)	0.56	(1)	32.195
					4.0	(6)	−76.48	(6)	0.8	(1)	1.694
G331.1335+0.1562A	16:09:15.16	(2)	−51:32:40.63	(9)	10.4	(2)	−76.139	(5)	0.60	(1)	4.664
G331.1331+0.1568A	16:09:14.884	(9)	−51:32:40.070	(7)	4.8	(1)	−74.512	(8)	0.52	(2)	1.889
G331.2846−0.1953A	16:11:30.32	(4)	−51:41:59.9	(1)	1.08	(4)	−94.03	(3)	1.44	(6)	1.168
G331.2800−0.1899A	16:11:27.57	(5)	−51:41:56.89	(5)	8.4	(6)	−89.31	(3)	0.77	(6)	4.883
G331.2800−0.1899B	16:11:28	(0)	−51:41:57.02	(1)	6.3	(9)	−89.94	(6)	0.9	(2)	4.333
G331.2800−0.1899C	16:11:27.58	(7)	−51:41:57.03	(2)	12.2	(3)	−90.77	(1)	0.81	(3)	7.417
G331.2800−0.1899D	16:11:27.55	(6)	−51:41:57.07	(1)	6	(5)	−91.31	(5)	0.2	(2)	1.021
					1.0	(1)	−92.17	(8)	1.2	(2)	0.170
G331.2802−0.1898A*	16:11:27.6	(2)	−51:41:56.4	(2)	5.4	(6)	−89.92	(5)	0.8	(1)	3.427
G331.2803−0.1899A	16:11:27.66	(4)	−51:41:56.26	(7)	5.0	(4)	−88.49	(3)	0.88	(7)	3.306
G331.2768−0.1870A	16:11:25.91	(5)	−51:41:57.21	(5)	3.0	(3)	−86.83	(4)	0.8	(1)	1.861
G331.2793−0.1873A	16:11:26.69	(2)	−51:41:51.98	(7)	2.7	(1)	−85.764	(9)	0.44	(2)	0.890
G331.2764−0.1874A	16:11:25.91	(3)	−51:41:59.38	(4)	3.78	(7)	−85.259	(6)	0.67	(1)	1.896
G331.2783−0.1884A	16:11:26.71	(3)	−51:41:57.3	(1)	1.34	(4)	−87.816	(6)	0.38	(1)	0.382
G331.2765−0.1871A	16:11:25.85	(2)	−51:41:58.05	(3)	2.0	(1)	−87.76	(1)	0.50	(3)	0.752
G331.3409−0.3470A	16:12:26.40	(4)	−51:46:20.50	(2)	30.7	(9)	−65.69	(1)	0.67	(2)	15.454
G331.3703−0.3990A	16:12:48.54	(5)	−51:47:24.39	(5)	5.15	(9)	−65.132	(4)	0.471	(9)	1.826
G331.3705−0.1446A	16:11:41.22	(4)	−51:36:15.37	(7)	0.90	(5)	−87.95	(3)	1.09	(7)	0.740
G331.3705−0.1446B	16:11:41.23	(5)	−51:36:15.3	(1)	0.90	(7)	−89.07	(3)	0.76	(7)	0.517
G331.3798+0.1490A	16:10:26.81	(2)	−51:22:58.5	(1)	1.47	(7)	−45.72	(2)	0.74	(4)	0.816
G331.4093−0.1643A	16:11:57.37	(4)	−51:35:32.033	(9)	1.27	(2)	−85.050	(5)	0.54	(1)	0.518
G331.4407−0.1869A	16:12:12.2	(1)	−51:35:14.1	(2)	3.3	(3)	−91.66	(2)	0.49	(4)	1.228
					0.56	(4)	−90.06	(6)	1.5	(1)	0.208

Table A1 – *continued*

Spot name	α_{2000} (h:m:s)		δ_{2000} (°:′:″)		Peak flux density (Jy)		Peak velocity (km s^{-1})		FWHM (km s^{-1})		Integrated flux density (Jy km s^{-1})
G331.4408−0.1869A	16:12:12.25	(7)	−51:35:13.88	(6)	1.10	(6)	−87.94	(2)	0.65	(4)	0.536
G331.4381−0.1864A	16:12:11.3	(1)	−51:35:19.3	(1)	1.57	(3)	−87.756	(6)	0.56	(1)	0.660
					0.70	(9)	−86.88	(5)	0.8	(1)	0.294
G331.4417−0.1580A	16:12:04.85	(5)	−51:33:55.74	(3)	0.73	(3)	−85.98	(2)	1.05	(5)	0.574
G331.4876−0.0863A	16:11:58.9	(1)	−51:28:54.33	(6)	0.73	(7)	−90.19	(4)	0.9	(1)	0.483
G331.4954−0.0786A	16:11:59.05	(2)	−51:28:14.81	(6)	31.7	(4)	−89.001	(4)	0.673	(9)	16.069
G331.4962−0.0780A	16:11:59.12	(4)	−51:28:11.66	(2)	1.7	(1)	−88.45	(3)	0.84	(7)	1.073
G331.4874−0.0865A	16:11:58.87	(3)	−51:28:55.23	(3)	1.41	(4)	−87.906	(7)	0.54	(2)	0.575
G331.5046−0.1158A	16:12:11.44	(3)	−51:29:30.20	(3)	2.43	(4)	−100.45	(1)	1.19	(2)	2.171
G331.5033−0.1066A	16:12:08.64	(8)	−51:29:09.1	(1)	0.70	(4)	−88.39	(2)	0.73	(5)	0.386
G331.5028−0.1068A	16:12:08.55	(2)	−51:29:10.76	(4)	1.39	(7)	−86.90	(1)	0.49	(3)	0.508
G331.5032−0.1067A	16:12:08.65	(9)	−51:29:09.71	(6)	0.87	(8)	−86.18	(4)	1.0	(1)	0.625
G331.5219−0.0811A	16:12:07.16	(6)	−51:27:16.2	(2)	0.65	(4)	−90.84	(1)	0.49	(4)	0.237
G331.5179−0.0823A	16:12:06.36	(3)	−51:27:29.28	(3)	3.7	(2)	−88.04	(3)	0.97	(6)	2.708
					2.5	(3)	−89.36	(4)	0.8	(1)	1.830
G331.5179−0.0823B	16:12:06.34	(6)	−51:27:29.42	(5)	7.2	(3)	−90.08	(1)	0.60	(3)	3.267
G331.5185−0.0823A	16:12:06.52	(7)	−51:27:27.81	(5)	0.53	(2)	−87.063	(8)	0.50	(2)	0.199
G331.5290−0.0982A	16:12:13.665	(9)	−51:27:43.92	(2)	18.7	(6)	−93.017	(7)	0.50	(2)	7.093
G331.5327−0.0993A	16:12:15.00	(9)	−51:27:37.6	(2)	79	(2)	−91.827	(9)	0.58	(2)	34.306
					10	(1)	−91.06	(3)	0.45	(6)	4.343
G331.5237−0.1009A	16:12:12.87	(2)	−51:28:04.02	(1)	4.53	(9)	−91.082	(4)	0.422	(9)	1.437
G331.5312−0.0987A	16:12:14.40	(2)	−51:27:39.71	(6)	1.21	(3)	−90.662	(5)	0.42	(1)	0.380
G331.5341−0.0997A	16:12:15.50	(5)	−51:27:35.31	(6)	3.82	(6)	−89.621	(6)	0.75	(1)	2.160
G331.5432−0.0660A	16:12:09.17	(2)	−51:25:44.2	(1)	1.6	(1)	−88.77	(3)	0.74	(8)	0.893
G331.5432−0.0660B	16:12:09.18	(2)	−51:25:44.24	(7)	0.80	(8)	−89.54	(4)	0.9	(1)	0.519
G331.5461−0.0688A	16:12:10.73	(6)	−51:25:44.6	(2)	0.62	(3)	−87.74	(1)	0.59	(3)	0.274
					0.44	(5)	−87.02	(3)	0.52	(7)	0.194
G331.5548−0.1227A	16:12:27.4	(1)	−51:27:44.49	(1)	3.2	(1)	−104.01	(1)	0.59	(3)	1.418
G331.5544−0.1221A	16:12:27.1	(1)	−51:27:44.1	(1)	3.8	(3)	−100.68	(3)	0.95	(8)	2.714
G331.5544−0.1221B	16:12:27.10	(3)	−51:27:44.13	(6)	1.2	(1)	−102.05	(5)	1.0	(1)	0.912
G331.5544−0.1221C	16:12:27.09	(2)	−51:27:44.1	(1)	0.68	(7)	−103.75	(6)	1.2	(1)	0.595
G331.5547−0.1211A	16:12:26.90	(2)	−51:27:40.69	(4)	4.01	(9)	−102.801	(4)	0.40	(1)	1.215
G331.5552−0.1215A	16:12:27.16	(3)	−51:27:40.6	(2)	0.74	(2)	−97.311	(8)	0.62	(2)	0.348
G331.5552−0.1215B	16:12:27.15	(7)	−51:27:40.7	(1)	0.64	(3)	−98.72	(2)	0.87	(5)	0.419
G331.8527−0.1295A	16:13:52.5	(1)	−51:15:46.63	(6)	1.15	(8)	−49.77	(4)	1.05	(9)	0.913
G331.8855+0.0619A	16:13:11.24	(2)	−51:06:04.75	(3)	0.99	(2)	−89.865	(5)	0.58	(1)	0.433
G331.8855+0.0627A	16:13:11.05	(6)	−51:06:02.6	(2)	4.3	(3)	−88.88	(3)	0.86	(6)	2.774
G331.8854+0.0625A*	16:13:11.1	(2)	−51:06:03.5	(2)	3.7	(2)	−88.81	(2)	0.76	(5)	2.112
G331.8847+0.0617A	16:13:11.08	(9)	−51:06:07.4	(2)	2.06	(4)	−88.375	(4)	0.436	(9)	0.675
G331.8854+0.0630A	16:13:10.96	(2)	−51:06:02.21	(2)	0.82	(2)	−87.135	(5)	0.405	(9)	0.250
G331.8892+0.0641A	16:13:11.70	(2)	−51:05:49.90	(8)	0.85	(3)	−86.785	(8)	0.46	(2)	0.294
					0.56	(3)	−86.12	(2)	0.58	(4)	0.194
G331.8864+0.0618A	16:13:11.522	(9)	−51:06:02.7	(1)	0.73	(3)	−86.378	(9)	0.42	(2)	0.230
G331.8898+0.0658A	16:13:11.44	(3)	−51:05:43.9	(1)	0.80	(3)	−85.978	(8)	0.48	(2)	0.286
G331.8880+0.0658A	16:13:10.94	(3)	−51:05:48.5	(1)	1.51	(1)	−86.863	(1)	0.330	(2)	0.375
G331.9209−0.0829A	16:13:59.17	(7)	−51:10:56.00	(6)	4.7	(2)	−51.63	(1)	0.44	(3)	1.549
					0.7	(2)	−52.18	(4)	0.4	(1)	0.231
G332.0933−0.4213A	16:16:16.59	(7)	−51:18:27.90	(8)	3.6	(2)	−58.82	(1)	0.53	(3)	1.442
					1.7	(2)	−58.16	(3)	0.67	(8)	0.681
G332.0911−0.4194A	16:16:15.44	(5)	−51:18:28.51	(8)	8.1	(2)	−55.849	(6)	0.45	(1)	2.742
G332.0908−0.4184A	16:16:15.12	(3)	−51:18:26.51	(5)	0.68	(3)	−58.05	(1)	0.53	(3)	0.270
G332.2420−0.0443A	16:15:17.74	(6)	−50:55:58.09	(9)	2.4	(2)	−47.32	(3)	0.89	(6)	1.599
G332.2420−0.0443B	16:15:17.78	(8)	−50:55:58.0	(1)	121	(3)	−49.178	(7)	0.63	(2)	57.263
					15	(4)	−49.91	(5)	0.36	(9)	7.099
G332.2417−0.0437A	16:15:17.53	(2)	−50:55:57.30	(4)	14.4	(3)	−48.527	(4)	0.509	(9)	5.513
G332.2393−0.0425A	16:15:16.55	(2)	−50:55:60.0	(1)	6.8	(5)	−48.51	(3)	0.61	(6)	3.146
G332.2401−0.0429A	16:15:16.88	(2)	−50:55:59.27	(2)	6.1	(4)	−47.93	(1)	0.40	(3)	1.838
G332.2390−0.0451A	16:15:17.2	(2)	−50:56:07.5	(4)	34	(1)	−47.31	(1)	0.86	(3)	21.996
G332.2387−0.0452A*	16:15:17.1	(2)	−50:56:08.7	(2)	6.5	(8)	−46.78	(3)	0.50	(7)	2.442
G332.2390−0.0428A	16:15:16.55	(6)	−50:56:01.78	(7)	1.10	(4)	−46.247	(9)	0.44	(2)	0.367
G332.2959−0.0945A	16:15:45.8	(2)	−50:55:54.5	(3)	20.2	(8)	−49.70	(2)	0.91	(4)	13.820
G332.2959−0.0945B	16:15:45.80	(5)	−50:55:54.47	(6)	21.4	(6)	−50.627	(9)	0.59	(2)	9.558

Table A1 – *continued*

Spot name	α_{2000} (h:m:s)		δ_{2000} (°:′:″)		Peak flux density (Jy)		Peak velocity (km s^{-1})		FWHM (km s^{-1})		Integrated flux density (Jy km s^{-1})
					14.9	(2)	−49.98	(1)	0.13	(2)	6.655
G332.2956−0.0945A*	16:15:45.7	(2)	−50:55:55.0	(2)	15.5	(5)	−49.83	(1)	0.60	(2)	6.951
G332.2953−0.0944A	16:15:45.61	(8)	−50:55:55.62	(5)	9.0	(2)	−48.355	(7)	0.58	(2)	3.924
G332.2941−0.0924A	16:15:44.771	(9)	−50:55:53.23	(5)	4.5	(2)	−48.915	(7)	0.35	(2)	1.180
G332.2924−0.0919A	16:15:44.15	(2)	−50:55:56.39	(6)	2.69	(7)	−46.107	(9)	0.74	(2)	1.492
G332.3191+0.1763A	16:14:41.1	(2)	−50:43:12.02	(8)	2.9	(2)	−48.15	(2)	0.82	(5)	1.799
G332.3174+0.1817A	16:14:39.18	(5)	−50:43:02.11	(2)	0.55	(3)	−49.28	(1)	0.54	(3)	0.222
G332.3546−0.1145A	16:16:07.18	(3)	−50:54:19.9	(4)	6.1	(1)	−50.221	(8)	0.81	(2)	3.698
G332.5832+0.1469A	16:16:00.97	(5)	−50:33:30.96	(9)	3.01	(5)	−42.631	(6)	0.76	(1)	1.718
G332.6036−0.1679A	16:17:29.34	(5)	−50:46:15.0	(1)	1.6	(1)	−46.15	(3)	0.63	(7)	0.763
G332.6042−0.1668A	16:17:29.21	(4)	−50:46:10.9	(1)	10.5	(3)	−45.836	(9)	0.72	(2)	5.714
G332.7163−0.0480A	16:17:28.34	(6)	−50:36:22.70	(4)	2.8	(1)	−40.02	(2)	1.11	(5)	2.347
G332.7167−0.0488A	16:17:28.65	(5)	−50:36:23.9	(1)	1.10	(5)	−39.71	(1)	0.58	(3)	0.480
					0.82	(5)	−38.66	(2)	0.77	(5)	0.358
G333.0024−0.4368A	16:20:28.68	(3)	−50:41:00.91	(5)	5.7	(2)	−56.387	(8)	0.48	(2)	2.041
					1.4	(1)	−55.77	(3)	0.57	(7)	0.501
G333.0289−0.0623A	16:18:56.54	(6)	−50:23:53.6	(1)	0.755	(5)	−42.125	(2)	0.513	(5)	0.292
					0.768	(3)	−43	(8)	0.14	(2)	0.297
G333.0290−0.0629A	16:18:56.73	(1)	−50:23:55.17	(4)	6.7	(2)	−40.03	(1)	0.75	(3)	3.800
G333.0290−0.0629B	16:18:56.70	(4)	−50:23:55.09	(3)	7.4	(4)	−40.88	(2)	0.63	(4)	3.502
G333.0294−0.0243A	16:18:46.64	(2)	−50:22:14.57	(4)	5.60	(7)	−42.224	(3)	0.419	(5)	1.767
G333.0135−0.4660A	16:20:39.46	(2)	−50:41:47.45	(3)	1.21	(5)	−52.65	(1)	0.58	(3)	0.528
G333.0678−0.4460A	16:20:48.72	(5)	−50:38:38.7	(2)	0.49	(2)	−54.19	(2)	0.71	(4)	0.262
G333.0731−0.3996A	16:20:37.76	(3)	−50:36:26.66	(8)	2.13	(2)	−52.639	(3)	0.676	(7)	1.084
G333.0699−0.3989A	16:20:36.7	(2)	−50:36:32.92	(7)	0.68	(1)	−53.451	(7)	0.63	(2)	0.321
G333.0708−0.3990A	16:20:37.0	(1)	−50:36:30.80	(9)	0.68	(3)	−53.75	(2)	0.81	(4)	0.415
G333.1040−0.5027A	16:21:13.55	(1)	−50:39:31.22	(5)	5.4	(2)	−57.356	(9)	0.51	(2)	2.077
G333.1037−0.5036A	16:21:13.7	(1)	−50:39:34.49	(6)	1.66	(7)	−58.22	(1)	0.54	(3)	0.677
G333.1045−0.5025A	16:21:13.65	(2)	−50:39:29.68	(3)	0.89	(4)	−56.89	(1)	0.55	(3)	0.371
G333.1003−0.4985A	16:21:11.43	(5)	−50:39:30.1	(2)	0.56	(6)	−55.15	(2)	0.45	(5)	0.192
G333.1210−0.4325A	16:20:59.39	(3)	−50:35:48.95	(6)	4.4	(1)	−50.780	(7)	0.45	(2)	1.505
G333.1205−0.4337A	16:20:59.6	(2)	−50:35:53.4	(4)	1.30	(6)	−53.17	(1)	0.56	(3)	0.551
G333.1206−0.4330A	16:20:59.42	(5)	−50:35:51.3	(1)	2.23	(6)	−52.661	(6)	0.45	(1)	0.759
					1.01	(7)	−51.86	(2)	0.70	(6)	0.344
G333.1214−0.4334A	16:20:59.75	(2)	−50:35:50.46	(4)	0.8	(2)	−53.51	(3)	0.3	(1)	0.181
					0.62	(1)	−53.908	(4)	0.372	(9)	0.141
G333.1254−0.4412A	16:21:02.90	(8)	−50:36:00.1	(1)	3.5	(3)	−47.16	(4)	1.06	(9)	2.804
G333.1254−0.4412B	16:21:02.87	(3)	−50:36:00.1	(1)	55	(1)	−49.983	(5)	0.52	(1)	21.447
					13	(2)	−49.12	(8)	1.4	(2)	5.069
G333.1254−0.4412C	16:21:02.88	(3)	−50:36:00.0	(2)	6.5	(4)	−48.12	(2)	0.48	(4)	2.339
					3.1	(9)	−47.61	(6)	0.4	(1)	1.115
G333.1300−0.4373A	16:21:03.06	(1)	−50:35:38.51	(2)	4.35	(2)	−51.528	(1)	0.358	(2)	1.172
G333.1310−0.4389A	16:21:03.75	(1)	−50:35:40.05	(7)	16.7	(2)	−50.238	(5)	0.69	(1)	8.702
					10	(1)	−49.704	(4)	0.26	(3)	5.211
G333.1256−0.4398A	16:21:02.58	(7)	−50:35:56.2	(2)	11.8	(5)	−49.09	(1)	0.56	(3)	4.978
G333.1257−0.4378A	16:21:02.0	(1)	−50:35:50.7	(1)	12	(1)	−48.633	(6)	0.30	(3)	2.680
					3.6	(3)	−49.04	(3)	0.53	(6)	0.804
G333.1256−0.4378A	16:21:02.03	(4)	−50:35:50.78	(6)	10	(1)	−48.69	(2)	0.47	(5)	3.545
G333.1255−0.4379A	16:21:02.03	(6)	−50:35:51.6	(1)	16.7	(8)	−48.05	(1)	0.52	(3)	6.571
G333.1260−0.4398A	16:21:02.7	(3)	−50:35:55.12	(9)	11.6	(7)	−47.40	(2)	0.56	(4)	4.893
G333.1254−0.4387A	16:21:02.20	(3)	−50:35:53.79	(8)	15.3	(3)	−46.730	(6)	0.67	(1)	7.756
					5.8	(4)	−45.81	(3)	0.96	(8)	2.940
G333.1381−0.4247A	16:21:01.89	(3)	−50:34:45.58	(8)	10.8	(2)	−56.070	(3)	0.464	(7)	3.771
G333.1319−0.4310A	16:21:01.92	(1)	−50:35:17.60	(5)	2.33	(9)	−55.586	(8)	0.40	(2)	0.702
G333.1398−0.4260A	16:21:02.69	(6)	−50:34:44.92	(4)	1.28	(5)	−53.770	(9)	0.54	(2)	0.522
G333.1629−0.1010A	16:19:42.69	(5)	−50:19:54.74	(7)	5.63	(6)	−91.480	(4)	0.730	(9)	3.093
G333.1631−0.1011A	16:19:42.75	(7)	−50:19:54.56	(4)	1.4	(2)	−90.83	(4)	0.7	(1)	0.690
G333.1610−0.1009A	16:19:42.15	(2)	−50:19:59.57	(5)	1.12	(3)	−92.337	(5)	0.45	(1)	0.379
					0.62	(6)	−92.83	(3)	0.54	(6)	0.210
G333.1850−0.0929A	16:19:46.47	(2)	−50:18:38.1	(2)	0.97	(4)	−86.18	(1)	0.73	(3)	0.536
G333.1839−0.0904A	16:19:45.53	(3)	−50:18:34.63	(4)	2.0	(1)	−86.69	(2)	0.90	(5)	1.361

Table A1 – *continued*

Spot name	α_{2000} (h:m:s)		δ_{2000} (°:′:″)		Peak flux density (Jy)		Peak velocity (km s^{-1})		FWHM (km s^{-1})		Integrated flux density (Jy km s^{-1})
G333.1828−0.0880A	16:19:44.59	(6)	−50:18:31.04	(2)	1.41	(7)	−86.83	(1)	0.33	(2)	0.355
G333.2302−0.0583A	16:19:49.41	(7)	−50:15:15.4	(1)	280	(3)	−87.298	(6)	1.07	(1)	224.818
					7	(2)	−89.2	(3)	1.6	(6)	5.620
G333.2344−0.0628A	16:19:51.71	(2)	−50:15:16.24	(4)	1.51	(3)	−91.542	(7)	0.65	(2)	0.733
G333.2323−0.0568A	16:19:49.59	(1)	−50:15:06.13	(3)	2.4	(1)	−90.44	(1)	0.70	(3)	1.259
G333.2305−0.0582A*	16:19:49.5	(2)	−50:15:14.2	(2)	35	(4)	−87.87	(3)	0.59	(7)	15.509
					8	(3)	−88.3	(2)	1.4	(5)	3.545
G333.2325−0.0628A	16:19:51.22	(2)	−50:15:21.18	(2)	3.76	(3)	−89.012	(2)	0.429	(5)	1.213
G333.2332−0.0627A	16:19:51.37	(8)	−50:15:19.10	(4)	6.3	(6)	−88.10	(2)	0.44	(5)	2.077
G333.2332−0.0627B	16:19:51.38	(7)	−50:15:19.0	(1)	2.1	(5)	−88.5	(1)	0.8	(2)	1.329
G333.2307−0.0585A	16:19:49.6	(2)	−50:15:14.54	(9)	5.3	(8)	−86.56	(4)	0.6	(1)	2.583
G333.2307−0.0585B	16:19:49.61	(7)	−50:15:14.4	(1)	10.2	(7)	−88.16	(2)	0.47	(4)	3.634
G333.2345−0.0640A	16:19:52.10	(1)	−50:15:19.02	(9)	8.0	(3)	−86.098	(9)	0.44	(2)	2.666
G333.2336−0.0632A	16:19:51.61	(7)	−50:15:19.14	(6)	2.9	(3)	−85.42	(5)	1.0	(1)	2.107
G333.2337−0.0625A	16:19:51.45	(5)	−50:15:17.1	(1)	12.1	(2)	−85.556	(4)	0.377	(7)	3.431
					5.2	(7)	−84.99	(4)	0.7	(1)	1.475
G333.2343−0.0610A	16:19:51.24	(8)	−50:15:11.92	(8)	8.62	(9)	−85.492	(3)	0.506	(7)	3.285
G333.2198−0.4027A	16:21:17.90	(2)	−50:30:22.21	(8)	21.5	(2)	−51.675	(2)	0.422	(5)	6.821
					1.58	(7)	−51.86	(4)	1.54	(8)	0.501
G333.2204−0.4030A	16:21:18.13	(8)	−50:30:21.58	(9)	0.92	(5)	−54.65	(2)	0.82	(5)	0.566
G333.2204−0.4030B	16:21:18.14	(5)	−50:30:21.57	(4)	1.32	(7)	−55.82	(3)	1.15	(7)	1.146
G333.2200−0.4008A	16:21:17.43	(4)	−50:30:16.9	(2)	2.9	(2)	−53.74	(3)	0.90	(7)	1.964
G333.2203−0.4018A	16:21:17.8	(2)	−50:30:18.6	(3)	1.8	(1)	−53.61	(2)	0.75	(4)	1.018
G333.2203−0.4019A	16:21:17.8	(1)	−50:30:19.0	(2)	2.5	(2)	−52.72	(2)	0.56	(4)	1.050
					1.6	(2)	−53.43	(4)	0.8	(1)	0.672
G333.2845−0.3732A	16:21:27.31	(4)	−50:26:22.48	(8)	0.78	(5)	−52.09	(3)	0.90	(6)	0.530
G333.3008−0.3516A	16:21:25.92	(8)	−50:24:46.3	(1)	0.53	(3)	−49.45	(2)	0.70	(4)	0.279
G333.3117+0.1033A	16:19:28.67	(5)	−50:04:54.82	(2)	3.34	(6)	−45.161	(4)	0.480	(9)	1.208
G333.3137+0.1071A	16:19:28.21	(4)	−50:04:39.96	(6)	1.72	(6)	−48.22	(1)	0.69	(3)	0.887
G333.3123+0.1063A	16:19:28.05	(2)	−50:04:45.64	(5)	1.51	(4)	−47.186	(7)	0.58	(2)	0.658
G333.3146+0.1054A	16:19:28.90	(1)	−50:04:42.00	(2)	2.5	(2)	−44.43	(5)	1.0	(1)	1.941
G333.3358−0.3620A	16:21:38.02	(8)	−50:23:43.51	(6)	19.6	(4)	−51.927	(8)	0.81	(2)	11.951
G333.3358−0.3620B	16:21:38.05	(7)	−50:23:43.35	(5)	12.5	(2)	−52.43	(8)	0.2	(2)	1.883
					3	(3)	−52.87	(5)	0.2	(2)	0.452
G333.3376−0.3621A	16:21:38.54	(4)	−50:23:39.2	(1)	2.0	(9)	−49.96	(4)	0.2	(1)	0.369
					1.0	(3)	−49.52	(1)	0.25	(7)	0.184
G333.3376−0.3621B	16:21:38.5	(1)	−50:23:39.3	(1)	6.6	(3)	−50.29	(1)	0.41	(2)	2.047
G333.3376−0.3621C	16:21:38.5	(1)	−50:23:39.3	(2)	0.81	(5)	−54.10	(2)	0.60	(4)	0.365
G333.3284−0.3643A	16:21:36.67	(5)	−50:24:08.16	(2)	4.9	(1)	−50.867	(9)	0.68	(2)	2.519
G333.3285−0.3645A	16:21:36.73	(2)	−50:24:08.35	(5)	3.2	(3)	−50.22	(3)	0.63	(8)	1.509
G333.3359−0.3616A	16:21:37.95	(7)	−50:23:42.20	(7)	4.2	(1)	−51.098	(7)	0.41	(1)	1.303
					1.92	(8)	−50.54	(2)	1.01	(5)	0.596
G333.3384−0.3623A	16:21:38.79	(3)	−50:23:37.62	(2)	0.56	(3)	−47.60	(2)	0.82	(5)	0.347
G333.3874+0.0322A	16:20:07.52	(3)	−50:04:45.95	(4)	3.1	(1)	−70.22	(2)	0.96	(4)	2.231
G333.3860+0.0311A	16:20:07.42	(5)	−50:04:52.28	(5)	0.97	(9)	−72.57	(3)	0.65	(7)	0.473
G333.3862+0.0311A	16:20:07.48	(6)	−50:04:51.84	(4)	1.65	(5)	−72.03	(1)	0.83	(3)	1.027
G333.3872+0.0316A	16:20:07.62	(3)	−50:04:48.0	(2)	1.44	(6)	−68.44	(1)	0.49	(2)	0.528
G333.3745−0.2023A	16:21:05.93	(4)	−50:15:17.91	(7)	9.1	(4)	−61.31	(1)	0.44	(2)	3.000
G333.3773−0.2013A	16:21:06.42	(7)	−50:15:08.52	(7)	6.5	(1)	−57.979	(7)	0.93	(2)	4.574
G333.4679−0.1601A	16:21:19.62	(2)	−50:09:33.1	(2)	17.3	(1)	−43.007	(2)	0.558	(5)	7.267
G333.4679−0.1601B	16:21:19.61	(2)	−50:09:32.95	(2)	0.6	(1)	−43.94	(9)	0.9	(2)	0.405
G333.4669−0.1621A	16:21:19.88	(4)	−50:09:40.75	(6)	6.1	(1)	−45.275	(5)	0.55	(1)	2.508
					0.8	(1)	−45.2	(1)	1.4	(3)	0.329
G333.4658−0.1660A	16:21:20.62	(3)	−50:09:53.44	(7)	2.1	(1)	−44.10	(1)	0.52	(3)	0.815
G333.4658−0.1660B	16:21:20.62	(1)	−50:09:53.47	(3)	0.6	(1)	−44.79	(8)	0.8	(2)	0.364
G333.4664−0.1633A	16:21:20.05	(4)	−50:09:45.2	(1)	5.5	(2)	−43.467	(7)	0.41	(2)	1.716
G333.4681−0.1613A	16:21:19.97	(9)	−50:09:35.64	(7)	1.1	(1)	−42.11	(2)	0.53	(5)	0.435
G333.4681−0.1616A	16:21:20.1	(2)	−50:09:36.55	(4)	3.69	(8)	−41.518	(6)	0.55	(1)	1.530
G333.4684−0.1649A	16:21:21.00	(6)	−50:09:44.19	(3)	1.31	(6)	−38.91	(1)	0.51	(3)	0.502
G333.4973+0.1431A	16:20:07.59	(4)	−49:55:23.7	(1)	2.7	(2)	−112.39	(3)	0.75	(7)	1.531
					0.71	(7)	−113.60	(4)	0.85	(9)	0.403

Table A1 – *continued*

Spot name	α_{2000} (h:m:s)		δ_{2000} (°:′:″)		Peak flux density (Jy)		Peak velocity (km s^{-1})		FWHM (km s^{-1})		Integrated flux density (Jy km s^{-1})
G333.4967+0.1424A	16:20:07.61	(3)	−49:55:26.86	(8)	0.70	(5)	−113.53	(2)	0.64	(5)	0.339
G333.4967+0.1421A	16:20:07.69	(3)	−49:55:28.0	(1)	0.75	(3)	−113.060	(8)	0.49	(2)	0.277
G333.5228−0.2747A	16:22:04.49	(1)	−50:12:05.3	(1)	7.2	(2)	−50.220	(9)	0.78	(2)	4.211
G333.5507−0.2915A	16:22:16.36	(6)	−50:11:36.91	(4)	1.96	(6)	−46.232	(7)	0.44	(2)	0.653
G333.5650−0.2952A	16:22:21.11	(4)	−50:11:09.8	(1)	1.16	(9)	−46.65	(3)	0.72	(6)	0.631
G333.5618−0.0246A	16:21:08.74	(4)	−49:59:48.85	(8)	60	(1)	−39.98	(1)	0.85	(2)	38.498
G333.5687+0.0284A	16:20:56.61	(3)	−49:57:15.91	(7)	7.1	(1)	−84.796	(4)	0.504	(9)	2.693
G333.5934−0.2122A	16:22:06.63	(4)	−50:06:26.6	(1)	27.7	(3)	−49.561	(3)	0.617	(7)	12.863
G333.5950−0.2108A	16:22:06.70	(2)	−50:06:19.2	(1)	1.2	(1)	−48.75	(5)	1.1	(1)	1.021
G333.5950−0.2108B	16:22:06.7	(1)	−50:06:18.8	(2)	2.3	(1)	−50.25	(3)	0.79	(6)	1.374
G333.5950−0.2108C	16:22:06.7	(2)	−50:06:18.77	(6)	0.8	(1)	−51.34	(5)	0.7	(1)	0.407
G333.5941−0.2116A	16:22:06.66	(3)	−50:06:23.07	(8)	1.26	(6)	−48.60	(2)	0.81	(4)	0.768
G333.6919−0.1955A	16:22:28.19	(2)	−50:01:32.9	(1)	3.29	(9)	−50.610	(5)	0.358	(9)	0.886
					0.46	(9)	−50.7	(1)	1.1	(2)	0.124
G333.6958−0.1986A	16:22:30.06	(5)	−50:01:30.8	(1)	0.94	(3)	−51.43	(1)	0.76	(3)	0.535
G333.7123−0.1158A	16:22:12.50	(4)	−49:57:18.37	(5)	6.2	(1)	−31.495	(6)	0.73	(1)	3.407
G333.7098−0.1152A	16:22:11.69	(2)	−49:57:23.17	(8)	0.45	(5)	−28.12	(4)	0.70	(9)	0.236
G333.7733−0.2578A	16:23:06.16	(4)	−50:00:43.31	(2)	2.55	(5)	−49.405	(5)	0.51	(1)	0.985
G333.7722−0.0096A	16:22:00.29	(3)	−49:50:15.79	(5)	17.7	(8)	−89.33	(2)	0.88	(4)	11.671
G333.8181−0.3026A	16:23:29.83	(2)	−50:00:42.0	(1)	20.4	(8)	−48.31	(1)	0.58	(3)	8.895
G333.8187−0.3031A	16:23:30.11	(4)	−50:00:41.93	(3)	2.3	(2)	−47.70	(3)	0.70	(7)	1.219
G333.8993−0.0977A	16:22:56.86	(8)	−49:48:35.3	(1)	1.5	(2)	−63.65	(4)	0.8	(1)	0.885
					1.5	(1)	−62.83	(3)	0.65	(7)	0.885
G333.9007−0.0993A	16:22:57.65	(8)	−49:48:35.9	(2)	1.36	(8)	−64.36	(2)	0.84	(5)	0.861
G333.9307−0.1342A	16:23:14.73	(2)	−49:48:47.5	(1)	3.8	(2)	−42.10	(2)	0.69	(4)	1.960
G333.9305−0.1343A	16:23:14.71	(2)	−49:48:48.46	(4)	3.0	(2)	−42.55	(2)	0.60	(5)	1.356
G333.9303−0.1316A	16:23:13.95	(2)	−49:48:41.8	(1)	0.89	(6)	−41.67	(2)	0.52	(4)	0.345
G333.9744+0.0737A	16:22:31.40	(3)	−49:38:08.44	(4)	6.7	(2)	−58.30	(1)	0.72	(3)	3.610
G333.9746+0.0736A	16:22:31.49	(2)	−49:38:08.19	(2)	3.2	(3)	−59.67	(4)	0.93	(9)	2.246
G334.0266−0.0465A	16:23:16.67	(1)	−49:41:00.19	(2)	10.4	(1)	−84.040	(4)	0.721	(9)	5.641
G334.7452+0.5068A	16:23:57.70	(1)	−48:46:59.92	(4)	3.52	(7)	−64.554	(5)	0.51	(1)	1.360
G334.7459+0.5063A	16:23:57.99	(2)	−48:46:59.41	(8)	1.60	(5)	−63.49	(1)	0.70	(3)	0.845
G334.7469+0.5058A	16:23:58.40	(7)	−48:46:58.0	(1)	2.3	(2)	−61.15	(2)	0.46	(4)	0.803
					0.45	(5)	−60.22	(4)	0.8	(1)	0.157

APPENDIX B: GAUSSIAN SPECTRAL FITS TO AUTO-CORRELATION THERMAL LINE EMISSION

Table B1. Gaussian fits for the spectra of thermal lines detected towards class I CH_3OH maser sites. Column 1 lists the maser site name. Columns 2–5 contain information for CS, columns 6–9 for SiO, columns 10–13 for thermal CH_3OH. The columns for each type of emission list the fitted Gaussian parameters, as well as the integrated intensity bounded by these Gaussians. Note that the uncertainty for each parameter is quoted in parentheses, in units of the least significant figure. Rows without site names correspond to a second Gaussian fitted to the site directly above. If no Gaussian information is listed for an emission type, it was not detected.

Site name	CS (1–0) parameters							SiO (1–0) $v = 0$ parameters							CH_3OH 1_0-0_0 parameters						
	Peak intensity (K)		Peak velocity ($km\,s^{-1}$)		FWHM ($km\,s^{-1}$)		Integrated intensity ($K\,km\,s^{-1}$)	Peak intensity (K)		Peak velocity ($km\,s^{-1}$)		FWHM ($km\,s^{-1}$)		Integrated intensity ($K\,km\,s^{-1}$)	Peak intensity (K)		Peak velocity ($km\,s^{-1}$)		FWHM ($km\,s^{-1}$)		Integrated intensity ($K\,km\,s^{-1}$)
G330.294−0.393	0.507	(3)	−80.68	(1)	5.62	(4)	2.143								0.02	(2)	−80.7	(3)	9.7	(7)	0.147
G330.678−0.402	0.298	(4)	−63.87	(3)	5.32	(7)	1.194	0.013	(1)	−64.0	(2)	8.6	(4)	0.084	0.05	(3)	−63.53	(6)	3.4	(2)	0.127
G330.779+0.249	0.336	(5)	−43.51	(1)	2.72	(3)	0.687	0.027	(1)	−43.81	(9)	6.7	(2)	0.137	0.10	(4)	−43.48	(3)	2.55	(7)	0.192
G330.876−0.362	1.24	(1)	−62.79	(2)	4.58	(4)	4.279	0.044	(1)	−63.35	(6)	7.1	(1)	0.236	0.09	(4)	−62.91	(5)	4.0	(1)	0.272
G330.871−0.383	1.39	(1)	−62.94	(2)	4.88	(4)	5.102	0.060	(1)	−63.63	(5)	7.1	(1)	0.322	0.10	(4)	−63.25	(5)	4.9	(1)	0.370
G330.927−0.408	0.47	(2)	−41.38	(4)	2.9	(1)	1.040	0.016	(1)	−42.5	(1)	5.4	(3)	0.065	0.05	(4)	−41.49	(7)	2.8	(2)	0.106
G330.931−0.260	0.158	(4)	−90.18	(6)	5.2	(1)	0.622								0.02	(4)	−89.1	(2)	3.2	(4)	0.048
G330.955−0.182	1.483	(8)	−91.16	(1)	7.01	(4)	7.820	0.174	(1)	−90.01	(3)	7.96	(7)	1.043	0.12	(5)	−90.59	(6)	5.5	(1)	0.496
G331.131−0.470	0.870	(7)	−67.50	(1)	4.55	(3)	2.979	0.023	(1)	−67.2	(1)	4.2	(2)	0.072	0.09	(3)	−67.78	(4)	4.2	(1)	0.286
G331.134−0.488	0.526	(6)	−66.23	(2)	5.43	(5)	2.152	0.016	(1)	−66.5	(2)	7.7	(4)	0.093	0.03	(2)	−66.1	(1)	5.4	(2)	0.123
G331.132−0.244	0.897	(5)	−86.94	(1)	5.76	(3)	3.889	0.087	(1)	−86.74	(5)	8.5	(1)	0.554	0.19	(4)	−86.33	(3)	5.35	(8)	0.765
G331.134+0.156	0.277	(6)	−76.96	(3)	3.05	(6)	0.637	0.017	(1)	−76.2	(1)	5.1	(3)	0.065	0.06	(3)	−76.52	(5)	4.4	(1)	0.198
G331.279−0.189	0.808	(5)	−88.29	(1)	5.25	(3)	3.195	0.046	(1)	−87.2	(1)	10.9	(3)	0.376	0.11	(3)	−88.06	(3)	3.61	(7)	0.299
G331.341−0.347	0.519	(8)	−65.90	(2)	3.06	(5)	1.197	0.019	(1)	−66.5	(1)	6.9	(3)	0.098	0.04	(2)	−66.46	(6)	4.2	(1)	0.126
G331.370−0.399	0.255	(6)	−64.80	(3)	3.62	(8)	0.695	0.009	(1)	−66.3	(4)	12.3	(8)	0.083	0.02	(2)	−66.5	(2)	8.2	(5)	0.124
	0.051	(5)	−69.9	(1)	3.1	(3)	0.121														
G331.371−0.145	0.167	(3)	−87.06	(4)	4.16	(9)	0.523								0.03	(3)	−87.7	(1)	6.1	(3)	0.138
	0.052	(3)	−91.0	(1)	3.7	(3)	0.145														
G331.380+0.149	0.344	(8)	−45.05	(5)	4.8	(1)	1.255	0.069	(1)	−44.63	(6)	6.7	(1)	0.350	0.20	(6)	−45.03	(3)	4.32	(7)	0.650
	0.07	(1)	−50.3	(1)	1.9	(3)	0.098														
G331.409−0.164	0.348	(4)	−86.36	(4)	5.73	(8)	1.502	0.028	(1)	−85.05	(9)	5.0	(2)	0.105	0.11	(3)	−85.99	(4)	4.48	(8)	0.371
G331.44−0.14	0.169	(5)	−86.6	(1)	8.2	(3)	1.049	0.017	(1)	−85.6	(1)	5.0	(3)	0.064	0.05	(3)	−85.89	(8)	5.7	(2)	0.213
G331.440−0.187	0.240	(7)	−88.0	(1)	8.9	(3)	1.605	0.060	(1)	−87.97	(6)	7.1	(1)	0.320	0.18	(4)	−88.36	(3)	5.51	(7)	0.746
G331.442−0.158	0.203	(3)	−87.10	(6)	7.1	(1)	1.090	0.021	(1)	−87.0	(1)	6.4	(3)	0.101	0.09	(4)	−86.75	(5)	4.5	(1)	0.306
G331.492−0.082	0.586	(7)	−88.83	(2)	4.33	(6)	1.908	0.035	(1)	−88.8	(1)	7.7	(2)	0.202	0.06	(5)	−88.72	(7)	3.3	(2)	0.149
G331.503−0.109	0.63	(2)	−88.14	(7)	5.3	(2)	2.511	0.037	(1)	−88.0	(1)	7.4	(3)	0.206	0.08	(7)	−87.9	(1)	4.0	(2)	0.240
	0.269	(6)	−101.38	(6)	5.2	(1)	1.055	0.032	(1)	−100.8	(2)	8.5	(4)	0.206	0.08	(4)	−101.30	(6)	4.0	(1)	0.238
G331.519−0.082	0.785	(4)	−89.35	(1)	4.73	(3)	2.797	0.027	(1)	−89.3	(2)	8.3	(4)	0.169	0.04	(5)	−89.3	(1)	3.3	(3)	0.100
G331.530−0.099	1.196	(6)	−88.58	(1)	5.07	(3)	4.566	0.063	(1)	−88.63	(6)	7.4	(1)	0.353	0.14	(5)	−89.16	(4)	4.21	(9)	0.443
G331.544−0.067	0.842	(9)	−88.27	(2)	4.79	(6)	3.036	0.038	(1)	−88.50	(7)	5.3	(2)	0.151	0.10	(5)	−88.66	(5)	3.8	(1)	0.287
G331.555−0.122	0.558	(7)	−100.37	(3)	4.51	(6)	1.894	0.024	(1)	−98.2	(2)	16.5	(6)	0.299	0.09	(5)	−100.56	(5)	3.6	(1)	0.247
	0.113	(5)	−88.8	(2)	8.8	(4)	0.747														
G331.72−0.20	0.464	(6)	−47.44	(2)	2.88	(4)	1.007	0.020	(1)	−46.5	(1)	4.3	(2)	0.064	0.05	(4)	−46.7	(1)	6.0	(3)	0.225
G331.853−0.129	0.452	(4)	−50.57	(2)	3.50	(4)	1.191	0.056	(1)	−50.69	(5)	5.4	(1)	0.229	0.13	(6)	−50.84	(7)	5.4	(2)	0.531
G331.887+0.063	0.343	(3)	−87.57	(2)	4.95	(5)	1.278	0.081	(1)	−87.39	(3)	4.89	(7)	0.298	0.20	(4)	−87.44	(2)	4.06	(5)	0.611
G331.921−0.083	0.297	(8)	−51.59	(4)	3.3	(1)	0.742	0.015	(1)	−50.9	(2)	9.9	(5)	0.112	0.06	(5)	−51.56	(8)	3.6	(2)	0.162
G332.092−0.420	0.776	(6)	−56.73	(2)	4.47	(4)	2.613	0.018	(1)	−57.0	(2)	6.1	(4)	0.082	0.06	(4)	−56.97	(7)	4.1	(2)	0.185
G332.240−0.044	0.462	(5)	−47.97	(2)	3.93	(4)	1.365	0.053	(1)	−48.67	(8)	9.2	(2)	0.368	0.19	(6)	−48.18	(4)	4.8	(1)	0.693
	0.080	(3)	−48.6	(2)	14.1	(5)	0.847														

Table B1 – *continued*

Site name	CS (1–0) parameters							SiO (1–0) $v = 0$ parameters							CH_3OH 1_0-0_0 parameters						
	Peak intensity (K)		Peak velocity ($km\,s^{-1}$)		FWHM ($km\,s^{-1}$)		Integrated intensity ($K\,km\,s^{-1}$)	Peak intensity (K)		Peak velocity ($km\,s^{-1}$)		FWHM ($km\,s^{-1}$)		Integrated intensity ($K\,km\,s^{-1}$)	Peak intensity (K)		Peak velocity ($km\,s^{-1}$)		FWHM ($km\,s^{-1}$)		Integrated intensity ($K\,km\,s^{-1}$)
G332.295−0.094	0.564	(7)	−48.86	(2)	3.68	(5)	1.561	0.022	(1)	−50.3	(1)	9.2	(3)	0.153	0.06	(3)	−49.38	(8)	5.3	(2)	0.239
	0.095	(4)	−49.3	(2)	9.2	(5)	0.656														
G332.318+0.179	0.197	(5)	−48.30	(3)	2.50	(7)	0.370	0.022	(1)	−47.9	(1)	5.2	(3)	0.085	0.06	(4)	−48.23	(6)	4.1	(1)	0.183
	0.059	(3)	−48.2	(2)	5.9	(4)	0.264														
G332.355−0.114	0.523	(5)	−49.97	(1)	2.73	(3)	1.076								0.03	(3)	−50.20	(5)	2.1	(2)	0.048
G332.583+0.147	0.124	(9)	−45.03	(8)	2.2	(2)	0.209														
G332.604−0.167	0.40	(1)	−46.66	(5)	3.5	(1)	1.068	0.025	(1)	−46.5	(1)	7.5	(3)	0.142	0.07	(4)	−46.51	(9)	6.1	(2)	0.320
G332.716−0.048	0.140	(5)	−39.54	(7)	4.2	(2)	0.443								0.03	(4)	−39.8	(1)	3.5	(3)	0.080
G333.002−0.437	0.860	(6)	−55.62	(1)	3.31	(3)	2.140	0.019	(1)	−54.5	(1)	6.1	(3)	0.087	0.02	(3)	−54.6	(2)	6.5	(5)	0.097
	0.358	(7)	−51.63	(3)	3.08	(7)	0.831														
G333.029−0.063	0.49	(1)	−41.24	(3)	2.87	(7)	1.058								0.03	(4)	−41.3	(1)	3.4	(4)	0.077
G333.029−0.024	0.45	(1)	−41.73	(3)	2.16	(7)	0.731	0.016	(1)	−41.3	(2)	4.9	(4)	0.058	0.02	(7)	−41.77	(9)	2.1	(2)	0.031
G333.014−0.466	0.818	(8)	−54.33	(2)	4.40	(5)	2.707	0.027	(1)	−53.8	(1)	8.5	(3)	0.173	0.01	(6)	−54.9	(4)	5.9	(9)	0.045
	0.10	(1)	−60.6	(2)	3.2	(4)	0.239														
G333.068−0.446	1.43	(1)	−53.48	(2)	4.68	(4)	5.039	0.064	(1)	−53.27	(6)	6.2	(1)	0.298	0.10	(8)	−53.73	(5)	4.1	(1)	0.306
	0.190	(9)	−59.9	(1)	4.7	(3)	0.671														
G333.071−0.399	0.842	(7)	−53.59	(2)	5.07	(5)	3.212	0.047	(2)	−52.5	(1)	6.0	(2)	0.213	0.06	(7)	−53.68	(8)	4.6	(2)	0.209
								0.020	(1)	−58.4	(4)	18	(1)	0.278							
G333.103−0.502	1.156	(9)	−55.87	(1)	3.63	(3)	3.159	0.027	(1)	−55.4	(1)	9.1	(4)	0.184	0.04	(7)	−56.37	(8)	3.5	(2)	0.106
G333.121−0.433	2.24	(1)	−51.50	(2)	5.65	(4)	9.533	0.096	(2)	−51.54	(7)	8.8	(2)	0.634	0.07	(8)	−51.23	(8)	5.7	(2)	0.302
	0.207	(8)	−60.8	(1)	6.8	(3)	1.063														
G333.126−0.439	2.54	(2)	−50.98	(2)	5.74	(5)	10.976	0.139	(2)	−50.99	(6)	8.9	(1)	0.927	0.1	(1)	−50.49	(7)	6.0	(2)	0.455
	0.30	(1)	−59.5	(1)	6.7	(3)	1.521														
G333.137−0.427	2.84	(1)	−52.32	(1)	6.48	(4)	13.843	0.171	(2)	−52.80	(5)	6.8	(1)	0.876	0.13	(9)	−52.82	(6)	6.4	(1)	0.625
								0.077	(2)	−44.9	(1)	11.9	(3)	0.688							
G333.162−0.101	0.35	(1)	−92.06	(4)	2.47	(9)	0.651								0.02	(4)	−88.8	(4)	16	(1)	0.242
	0.151	(8)	−87.0	(1)	5.1	(3)	0.580														
G333.184−0.090	0.522	(9)	−86.14	(3)	3.09	(6)	1.216	0.018	(1)	−86.4	(2)	5.1	(4)	0.069	0.08	(8)	−86.23	(5)	3.6	(1)	0.216
	0.134	(9)	−90.4	(1)	3.7	(3)	0.370														
G333.233−0.061	0.157	(6)	−88.7	(2)	8.3	(4)	0.976	0.091	(2)	−87.85	(5)	5.9	(1)	0.407	0.15	(7)	−87.93	(3)	4.52	(6)	0.510
G333.220−0.402	0.842	(9)	−52.00	(2)	3.19	(4)	2.024	0.027	(1)	−52.3	(1)	4.9	(3)	0.100	0.04	(8)	−52.24	(7)	2.7	(2)	0.081
	0.101	(9)	−47.1	(1)	2.9	(3)	0.220														
G333.24+0.02	0.348	(8)	−69.87	(5)	4.7	(1)	1.240	0.019	(1)	−68.4	(2)	11.9	(5)	0.170	0.03	(5)	−69.1	(1)	6.8	(3)	0.153
G333.284−0.373	1.983	(7)	−51.947	(9)	5.46	(2)	8.154	0.098	(2)	−51.52	(4)	4.84	(9)	0.357	0.2	(1)	−51.90	(3)	4.44	(7)	0.668
G333.301−0.352	1.623	(8)	−50.27	(1)	4.80	(3)	5.868	0.066	(1)	−50.42	(4)	4.4	(1)	0.217	0.18	(9)	−50.48	(3)	4.06	(6)	0.551
	0.191	(8)	−58.7	(1)	4.8	(2)	0.690														
G333.313+0.106	0.468	(8)	−46.41	(4)	4.80	(9)	1.691	0.039	(1)	−46.8	(1)	7.8	(3)	0.228	0.11	(9)	−46.25	(6)	5.5	(1)	0.459
G333.335−0.363	1.112	(8)	−50.70	(2)	4.70	(4)	3.936	0.067	(2)	−49.93	(9)	6.0	(2)	0.302	0.16	(8)	−50.29	(2)	3.80	(5)	0.457
								0.019	(1)	−59.3	(6)	21	(1)	0.293							
G333.387+0.031	0.324	(9)	−69.87	(5)	3.6	(1)	0.890	0.025	(1)	−69.3	(2)	11.7	(5)	0.220	0.05	(8)	−69.88	(7)	3.6	(2)	0.136
G333.376−0.202	0.357	(8)	−59.94	(4)	3.08	(8)	0.827	0.021	(1)	−55.5	(3)	15.4	(7)	0.244	0.03	(6)	−59.0	(1)	4.9	(3)	0.111
G333.467−0.163	0.35	(1)	−43.81	(4)	3.0	(1)	0.802	0.041	(1)	−44.1	(1)	9.6	(3)	0.298	0.07	(7)	−43.49	(6)	4.6	(1)	0.244
	0.284	(6)	−44.52	(9)	8.8	(2)	1.890	0.011	(1)	−58.2	(6)	14	(1)	0.117							

Table B1 – *continued*

Site name	CS (1–0) parameters								SiO (1–0) $v = 0$ parameters								CH_3OH 1_0-0_0 parameters							
	Peak intensity (K)		Peak velocity ($km\,s^{-1}$)		FWHM ($km\,s^{-1}$)		Integrated intensity ($K\,km\,s^{-1}$)		Peak intensity (K)		Peak velocity ($km\,s^{-1}$)		FWHM ($km\,s^{-1}$)		Integrated intensity ($K\,km\,s^{-1}$)		Peak intensity (K)		Peak velocity ($km\,s^{-1}$)		FWHM ($km\,s^{-1}$)		Integrated intensity ($K\,km\,s^{-1}$)
G333.497+0.143	0.18	(4)	−113.3	(3)	2.8	(6)	0.379	0.013	(1)	−114.6	(3)	11.4	(8)	0.111	0.03	(6)	−113.28	(7)	2.4	(2)	0.053
G333.523−0.275	0.936	(8)	−49.68	(1)	3.51	(3)	2.474	0.037	(1)	−49.3	(1)	6.4	(2)	0.178	0.05	(8)	−49.64	(6)	2.9	(1)	0.110
G333.558−0.293	0.589	(9)	−45.83	(2)	2.87	(5)	1.272	0.013	(1)	−47.8	(3)	12.5	(8)	0.122	0.03	(7)	−45.95	(7)	2.4	(2)	0.055
G333.562−0.025	0.145	(9)	−46.7	(1)	3.2	(2)	0.345	0.016	(1)	−38.9	(2)	7.8	(5)	0.094	0.03	(7)	−39.5	(1)	4.2	(3)	0.096
G333.569+0.028	0.256	(9)	−84.67	(9)	5.3	(2)	1.013	0.031	(1)	−84.4	(1)	7.5	(3)	0.174	0.08	(6)	−84.64	(4)	4.2	(1)	0.254
G333.595−0.211	1.96	(1)	−47.56	(1)	5.33	(3)	7.858	0.069	(1)	−47.93	(6)	6.5	(1)	0.338	0.0	(1)	−47.9	(1)	3.8	(2)	0.000
G333.694−0.197	0.289	(9)	−50.53	(4)	2.8	(1)	0.606	0.026	(1)	−49.9	(2)	8.0	(4)	0.157	0.08	(7)	−50.47	(3)	2.98	(8)	0.180
G333.711−0.115	0.071	(7)	−29.0	(2)	4.6	(5)	0.247														
G333.773−0.258	0.377	(6)	−47.69	(4)	5.5	(1)	1.563	0.048	(1)	−48.64	(8)	5.8	(2)	0.211	0.06	(6)	−48.66	(7)	4.9	(2)	0.220
G333.772−0.010	0.121	(8)	−86.0	(1)	3.5	(3)	0.319								0.01	(5)	−86.8	(4)	7.5	(9)	0.057
G333.818−0.303	0.141	(6)	−46.6	(1)	5.4	(3)	0.574								0.01	(3)	−46.6	(4)	9	(1)	0.069
G333.900−0.098	0.134	(7)	−65.1	(1)	4.0	(2)	0.401	0.014	(1)	−65.1	(2)	6.6	(5)	0.070	0.03	(6)	−64.9	(1)	4.6	(3)	0.104
G333.930−0.133	0.198	(7)	−40.01	(9)	5.2	(2)	0.773	0.020	(1)	−39.4	(1)	5.2	(3)	0.078	0.02	(6)	−39.9	(2)	5.1	(4)	0.077
G333.974+0.074	0.22	(1)	−59.93	(7)	2.4	(2)	0.406								0.01	(5)	−58.0	(5)	10	(1)	0.072
G334.027−0.047	0.366	(8)	−84.93	(4)	3.67	(9)	1.011								0.03	(5)	−84.72	(7)	3.3	(2)	0.075
	0.06	(1)	−89.0	(2)	2.0	(4)	0.089														
G334.746+0.506	0.255	(7)	−62.45	(6)	4.0	(1)	0.771	0.023	(1)	−62.0	(2)	12.2	(5)	0.212	0.06	(7)	−62.36	(6)	4.4	(2)	0.201

Table B2. Gaussian fits for the spectra of H53α RRLs detected towards class I CH_3OH maser sites. If a maser site is not listed, then H53α emission was not detected. Column 1 lists the maser site name. Columns 2–5 list the fitted Gaussian parameters, as well as the integrated intensity bounded by these Gaussians. Note that the uncertainty for each parameter is quoted in parentheses, in units of the least significant figure.

Site name	Peak intensity (K)		Peak velocity ($km\,s^{-1}$)		FWHM ($km\,s^{-1}$)		Integrated intensity ($K\,km\,s^{-1}$)
G330.294−0.393	0.054	(1)	−83.1	(3)	27.8	(6)	1.130
G330.678−0.402	0.026	(1)	−62.2	(4)	21	(1)	0.405
G330.876−0.362	0.082	(1)	−51.3	(2)	32.8	(4)	2.032
G330.871−0.383	0.070	(1)	−54.8	(2)	32.8	(5)	1.729
G330.955−0.182	0.174	(1)	−90.50	(9)	33.6	(2)	4.411
G331.134−0.488	0.019	(1)	−70.3	(4)	15	(1)	0.218
G331.279−0.189	0.070	(1)	−80.1	(2)	24.7	(4)	1.302
G331.341−0.347	0.041	(1)	−61.5	(3)	28.5	(8)	0.878
G331.492−0.082	0.038	(1)	−90.3	(3)	21.7	(7)	0.620
G331.503−0.109	0.057	(1)	−89.1	(2)	19.2	(4)	0.824
G331.519−0.082	0.225	(1)	−91.72	(6)	26.2	(1)	4.445
G331.530−0.099	0.151	(1)	−89.52	(8)	22.9	(2)	2.600
G331.544−0.067	0.099	(1)	−90.8	(1)	21.6	(3)	1.611
G331.555−0.122	0.041	(1)	−99.2	(3)	32.2	(8)	0.988
G332.295−0.094	0.017	(1)	−46.3	(8)	29	(2)	0.372
G333.002−0.437	0.085	(2)	−53.9	(2)	22.2	(5)	1.421
G333.014−0.466	0.154	(1)	−53.09	(6)	21.8	(1)	2.537
G333.068−0.446	0.062	(1)	−56.3	(2)	27.3	(4)	1.279
G333.071−0.399	0.022	(1)	−54.1	(5)	34	(1)	0.560
G333.103−0.502	0.052	(1)	−53.7	(2)	26.0	(5)	1.021
G333.121−0.433	0.286	(1)	−47.75	(4)	26.53	(9)	5.704
G333.126−0.439	0.250	(1)	−50.34	(5)	28.1	(1)	5.294
G333.137−0.427	0.300	(1)	−50.44	(4)	29.50	(9)	6.671
G333.162−0.101	0.040	(1)	−92.0	(2)	22.0	(5)	0.668
G333.184−0.090	0.034	(1)	−92.4	(3)	19.1	(6)	0.490
G333.220−0.402	0.056	(1)	−51.5	(2)	17.5	(4)	0.736
G333.284−0.373	0.168	(1)	−51.81	(7)	28.1	(2)	3.560
G333.301−0.352	0.051	(1)	−53.2	(2)	27.9	(5)	1.070
G333.335−0.363	0.031	(1)	−46.9	(3)	26.7	(8)	0.630
G333.467−0.163	0.055	(1)	−43.1	(2)	20.7	(4)	0.863
G333.523−0.275	0.027	(1)	−51.7	(4)	28.3	(9)	0.571
G333.558−0.293	0.018	(1)	−52.3	(5)	18	(1)	0.242
G333.595−0.211	0.837	(1)	−45.38	(2)	31.78	(5)	20.020
G333.694−0.197	0.014	(1)	−46.9	(8)	24	(2)	0.241

APPENDIX C: GLIMPSE IMAGES

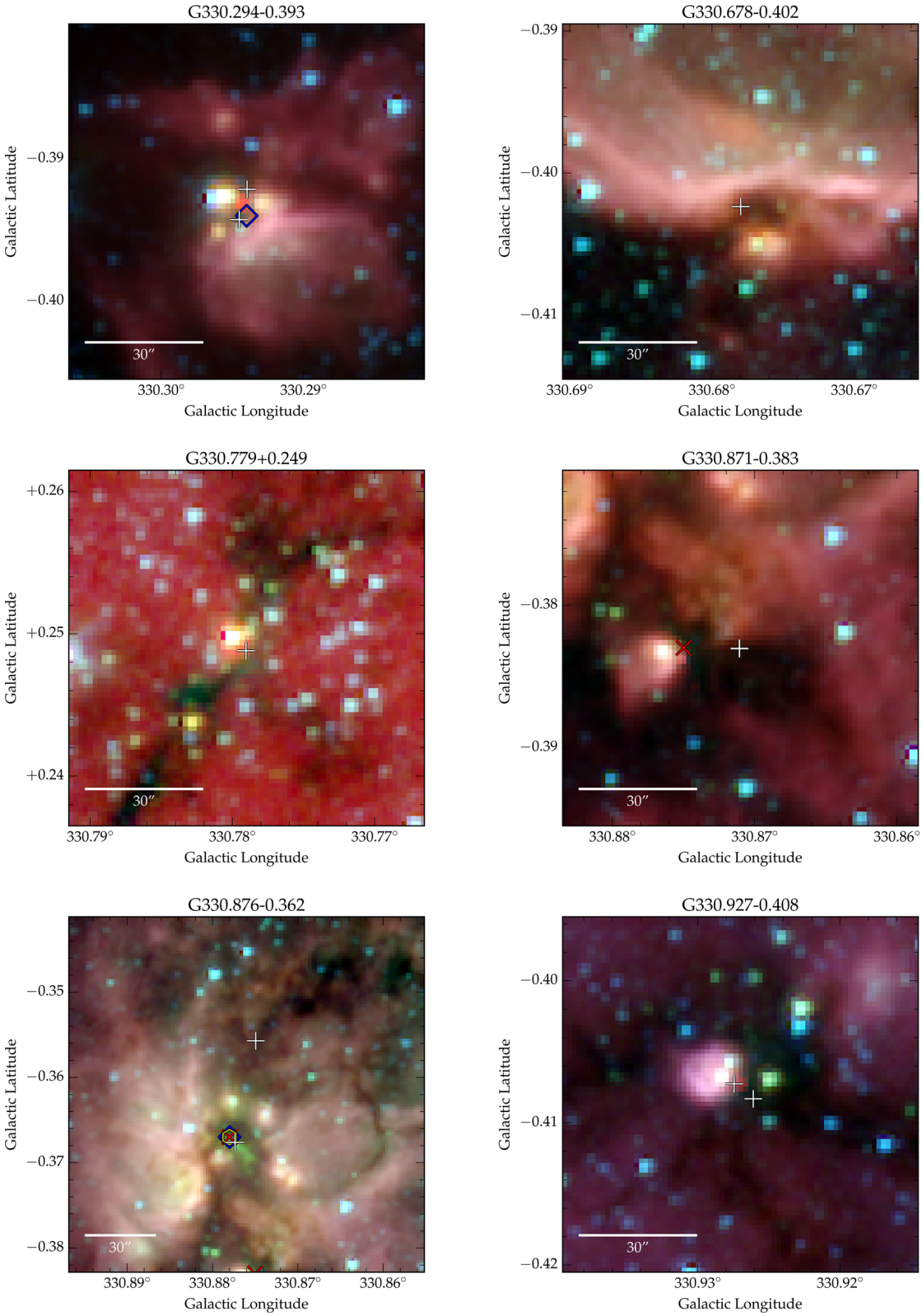

Figure C1. *Spitzer* GLIMPSE three-colour images (RGB = 3.6, 4.5 and 8.0 μm) overlaid with the positions of class I CH_3OH masers (white plus symbols). The size of the symbols reflects the maximum positional uncertainty for a maser spot. The published positions of class II CH_3OH, H_2O and OH masers are overlaid (red cross, blue diamond and yellow hexagon symbols, respectively; Sevenster et al. 1997; Caswell 1998; Breen et al. 2010b; Caswell et al. 2011; Walsh et al. 2011, 2014).

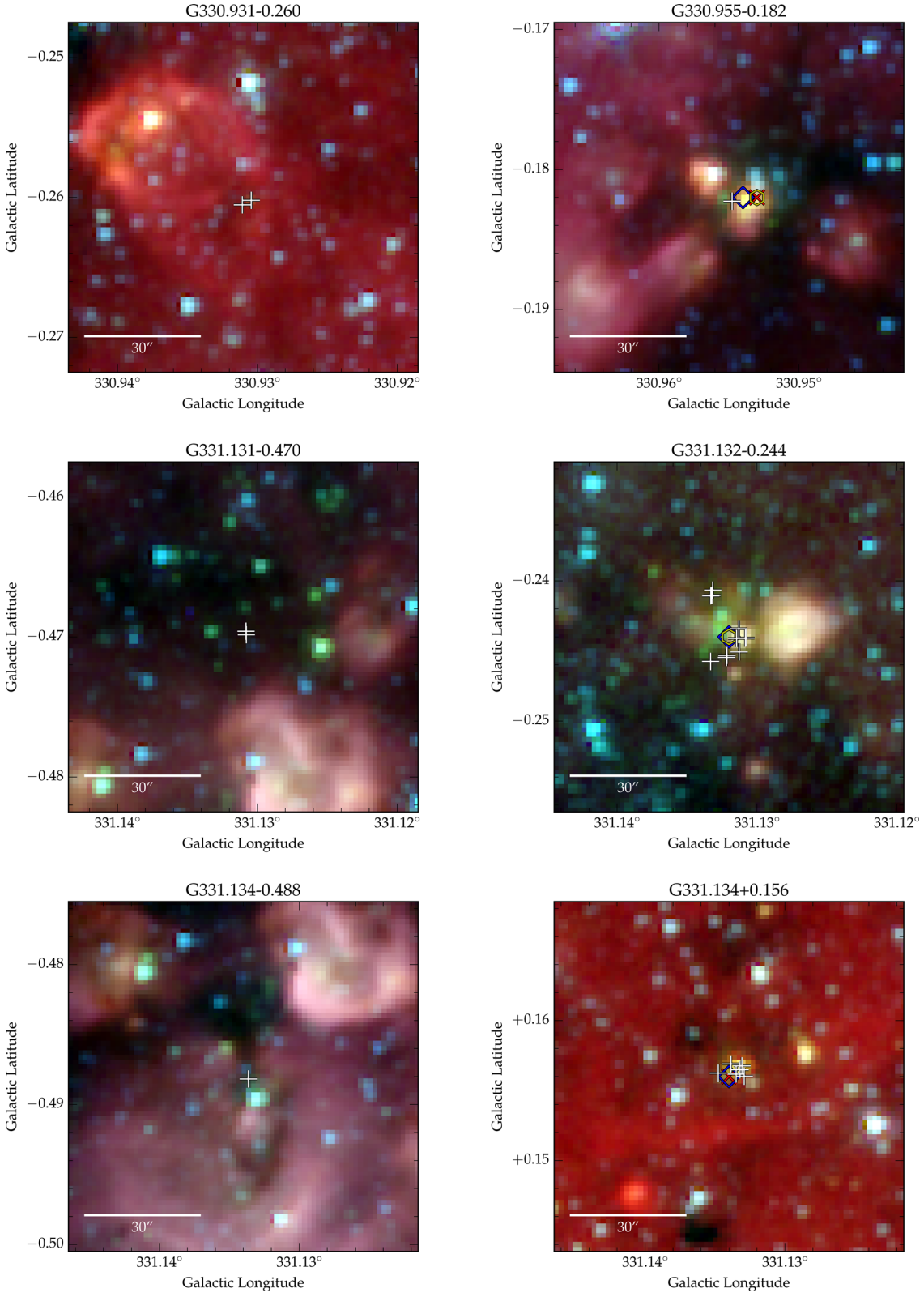

Figure C1 – *continued*

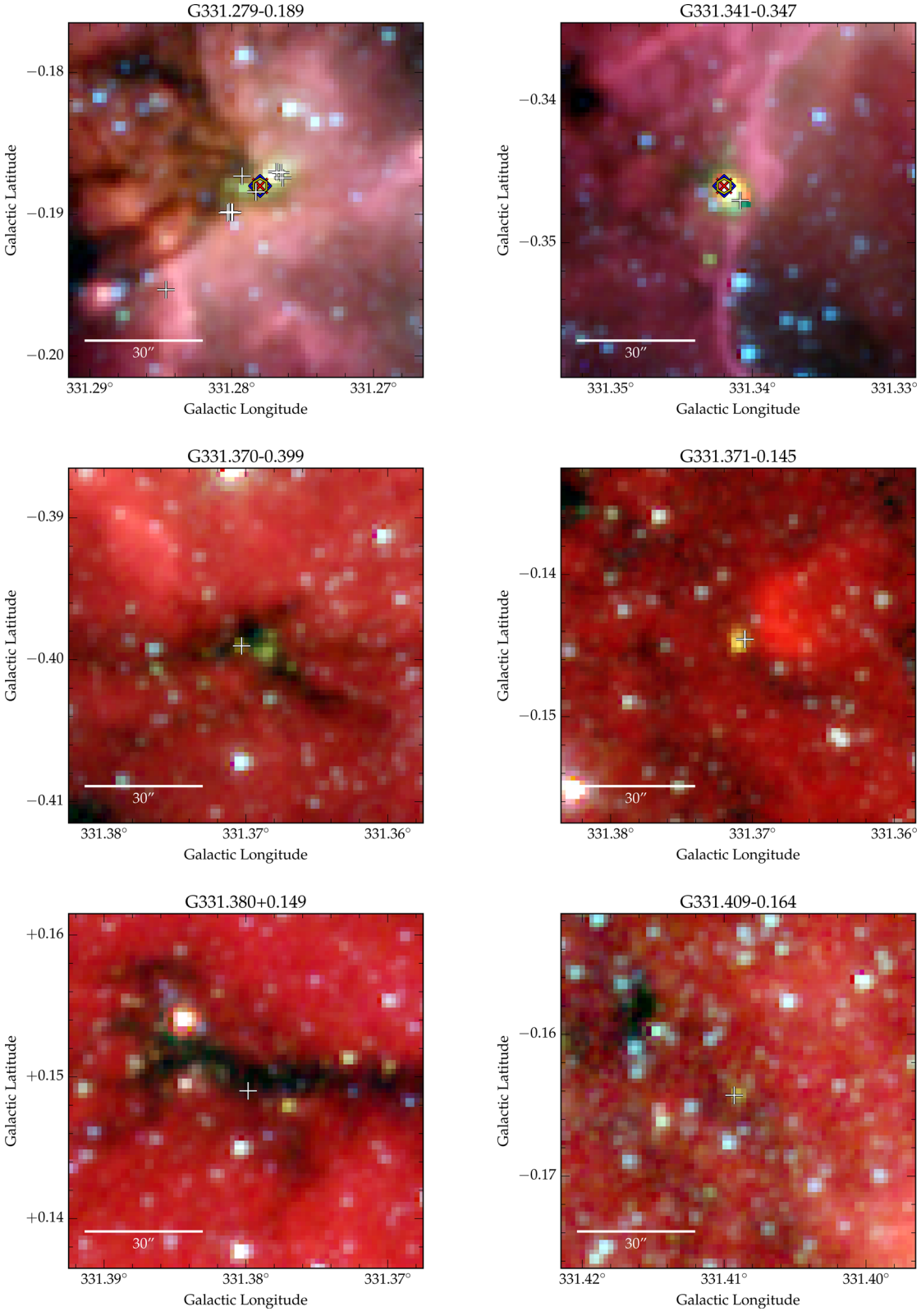

Figure C1 – *continued*

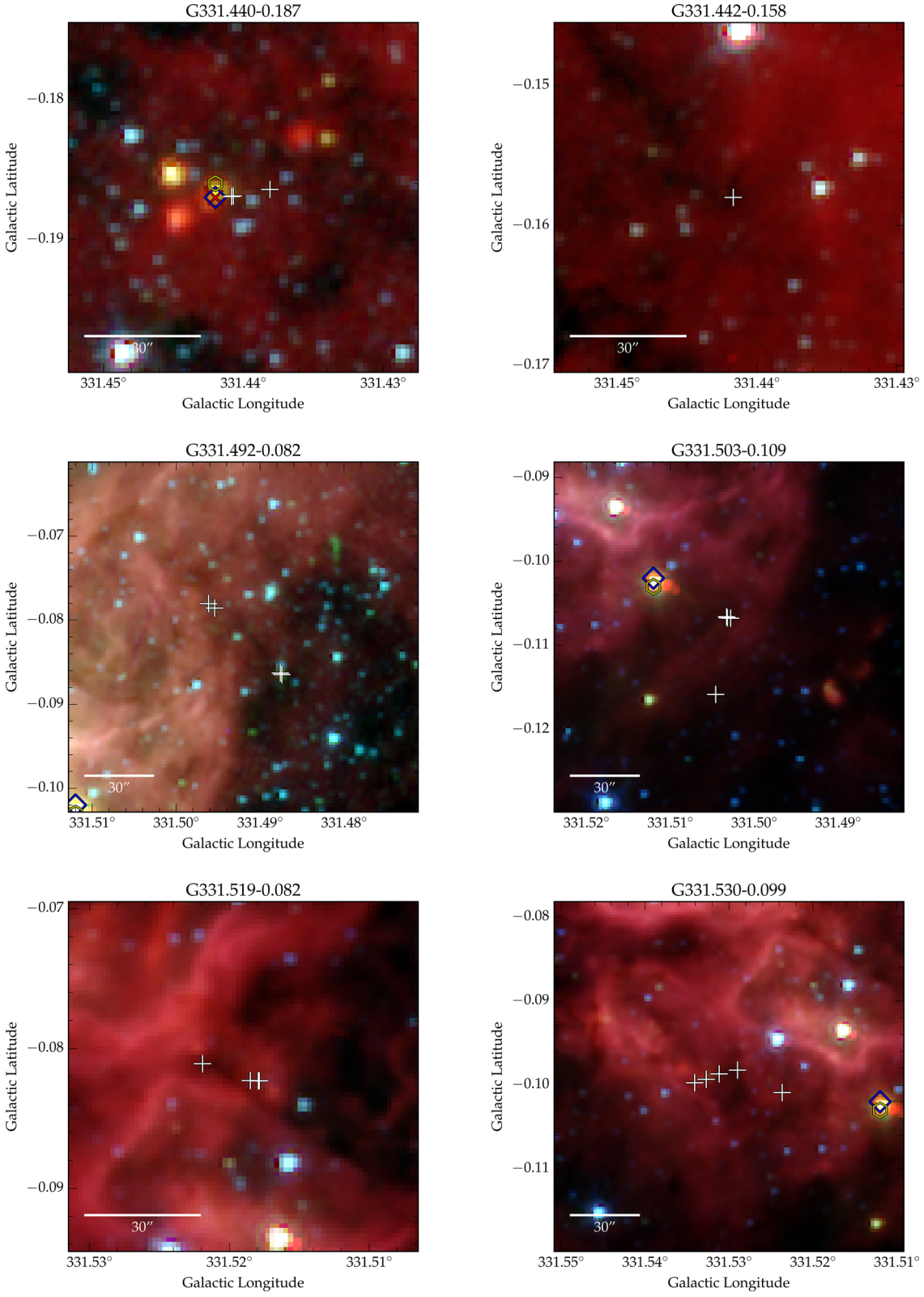

Figure C1 – *continued*

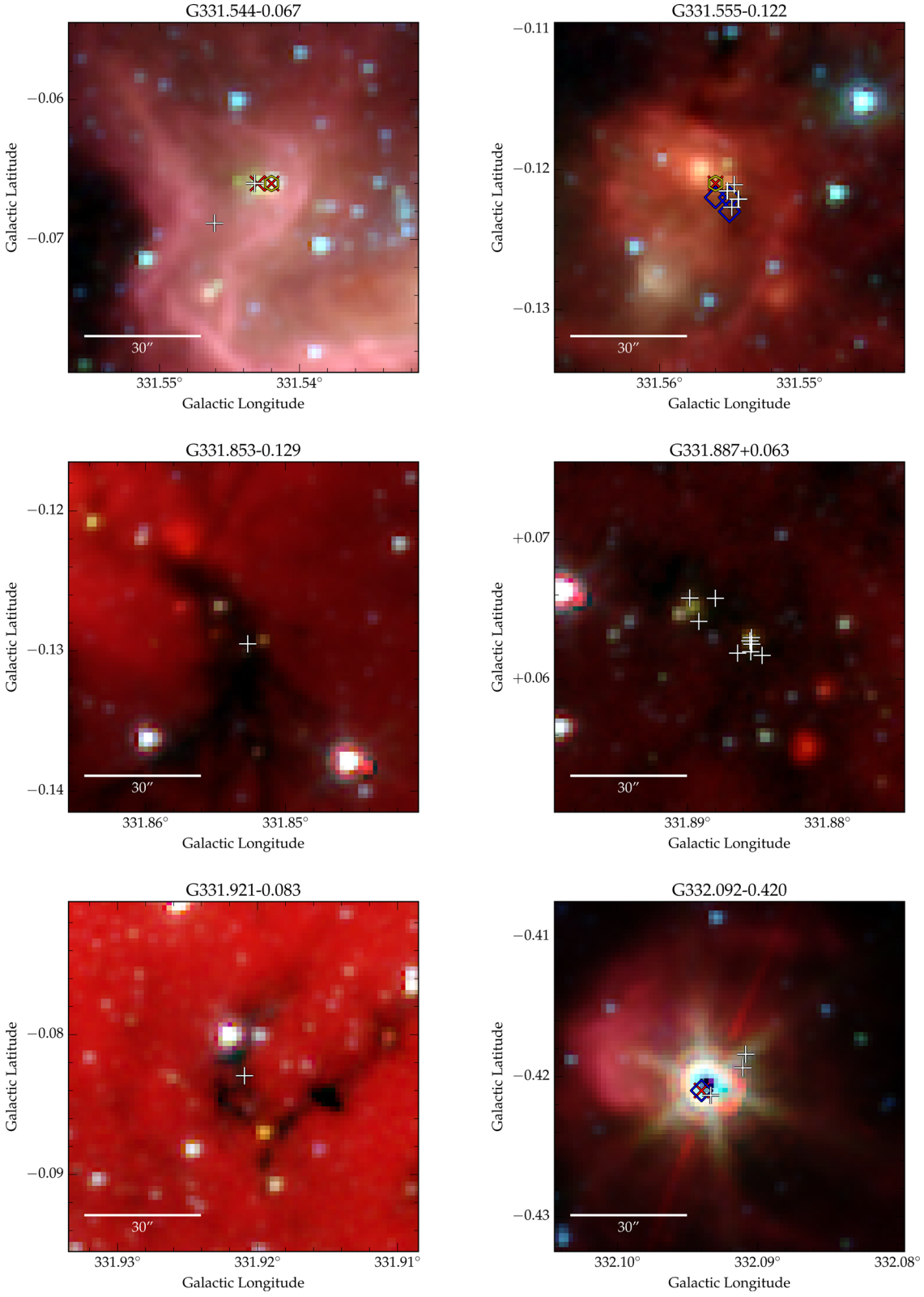

Figure C1 – *continued*

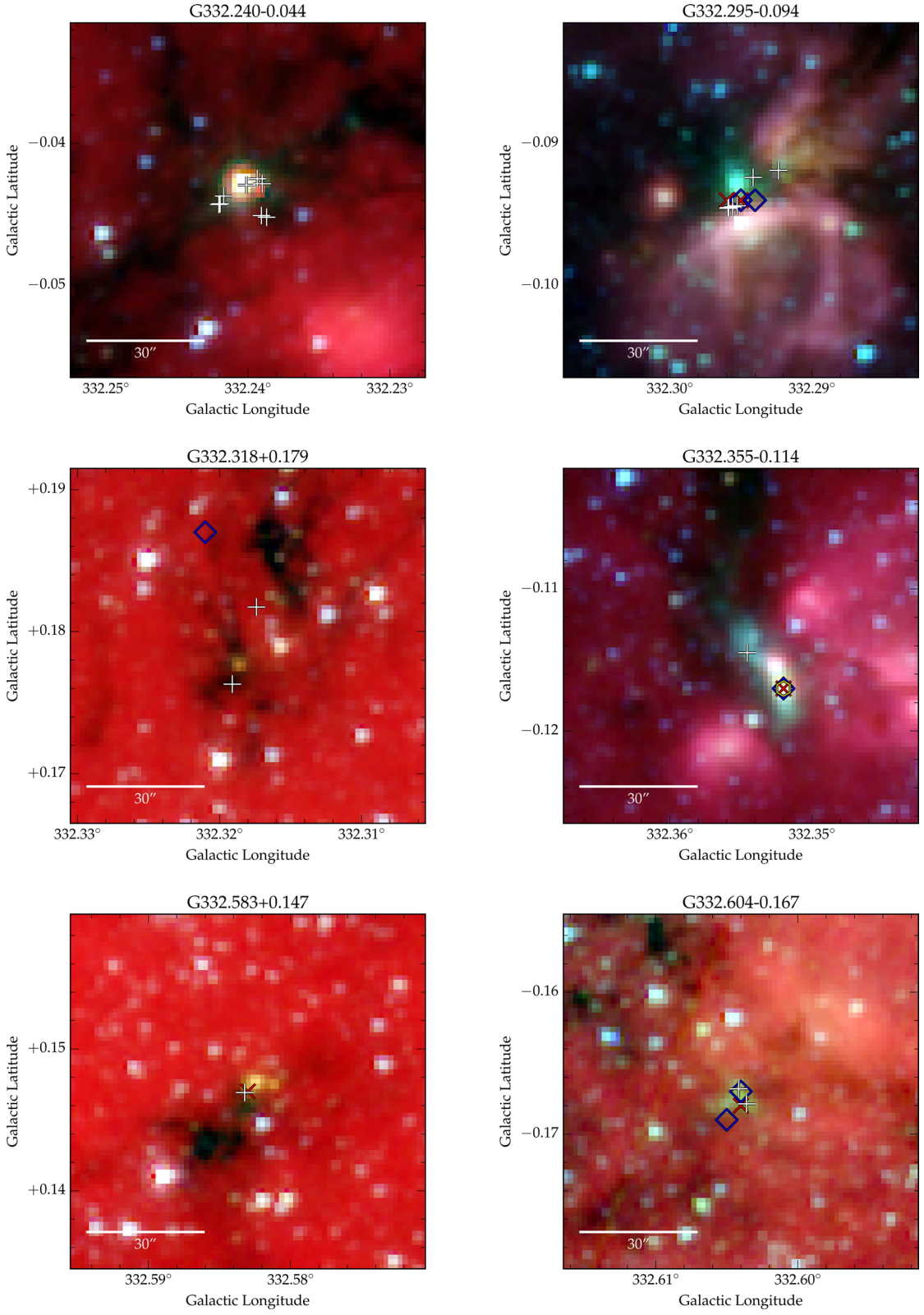

Figure C1 – *continued*

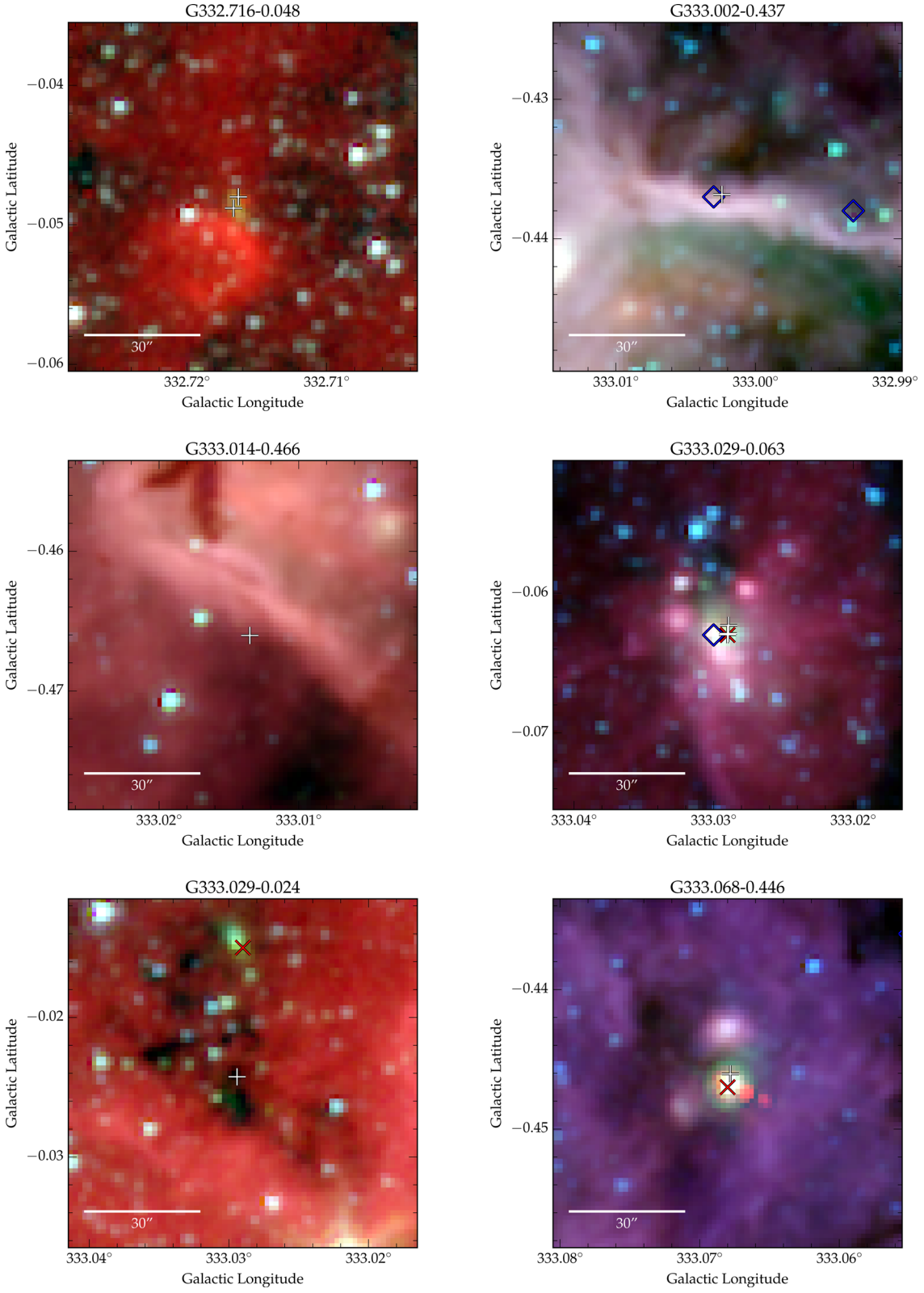

Figure C1 – *continued*

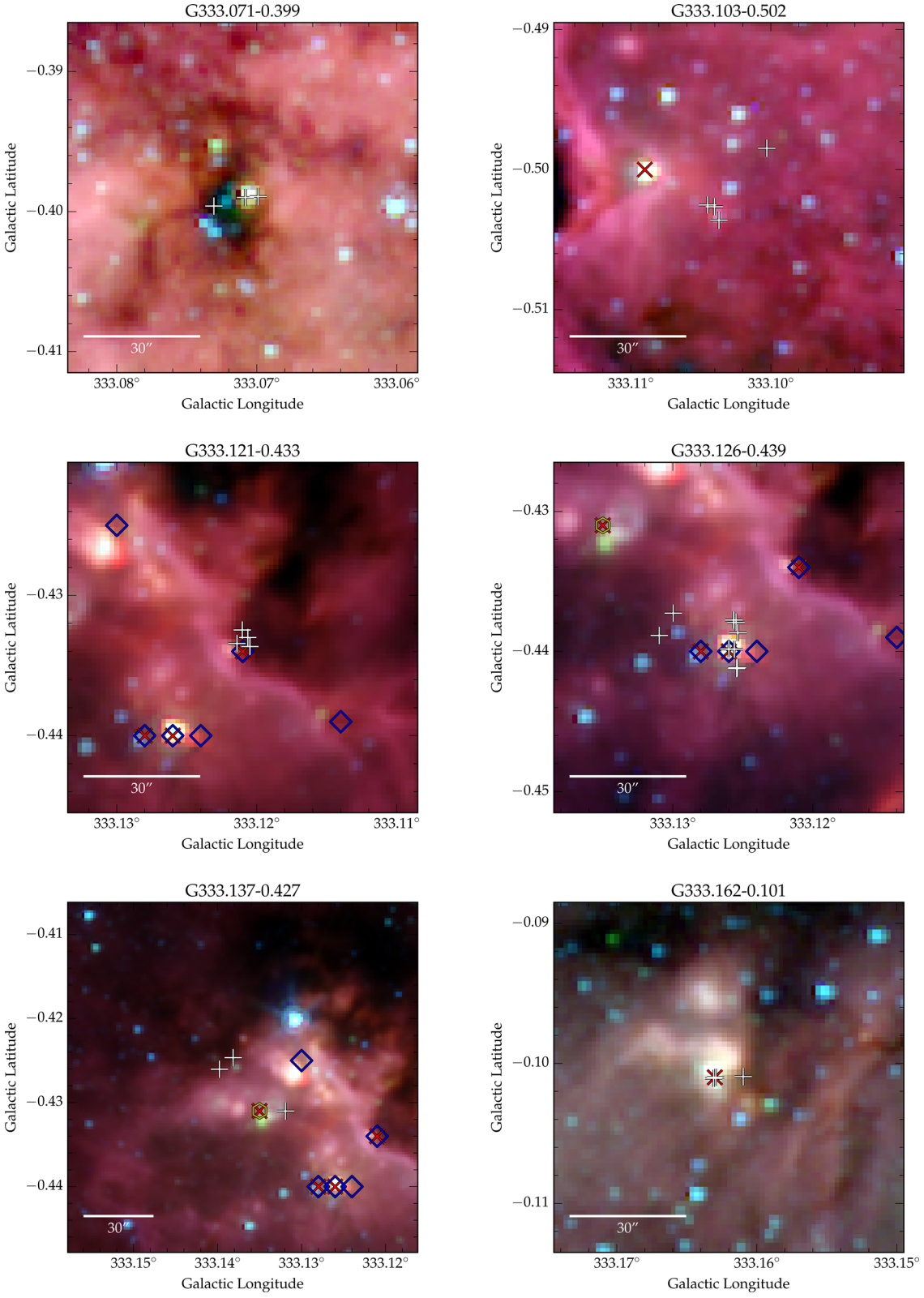

Figure C1 – *continued*

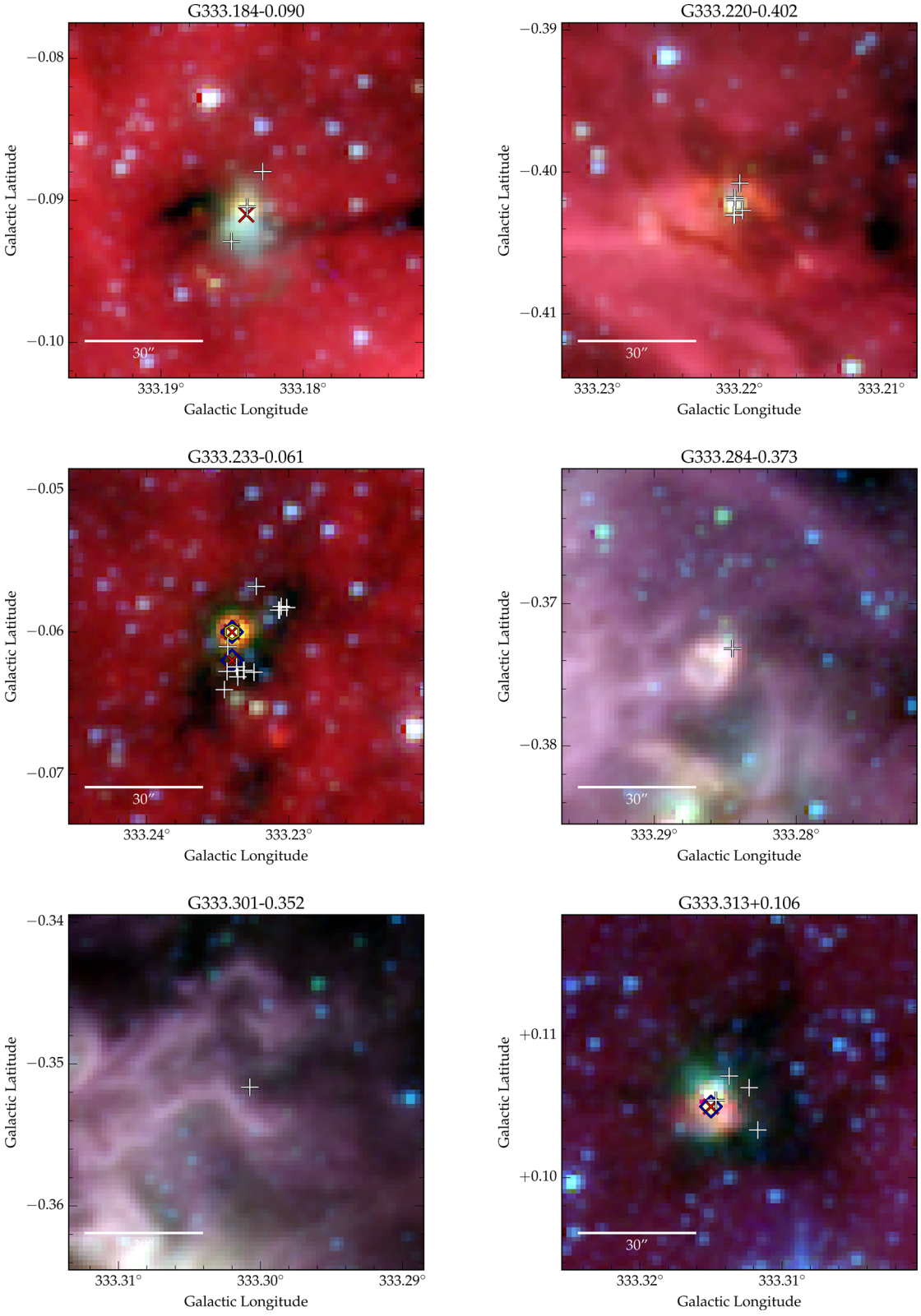

Figure C1 – *continued*

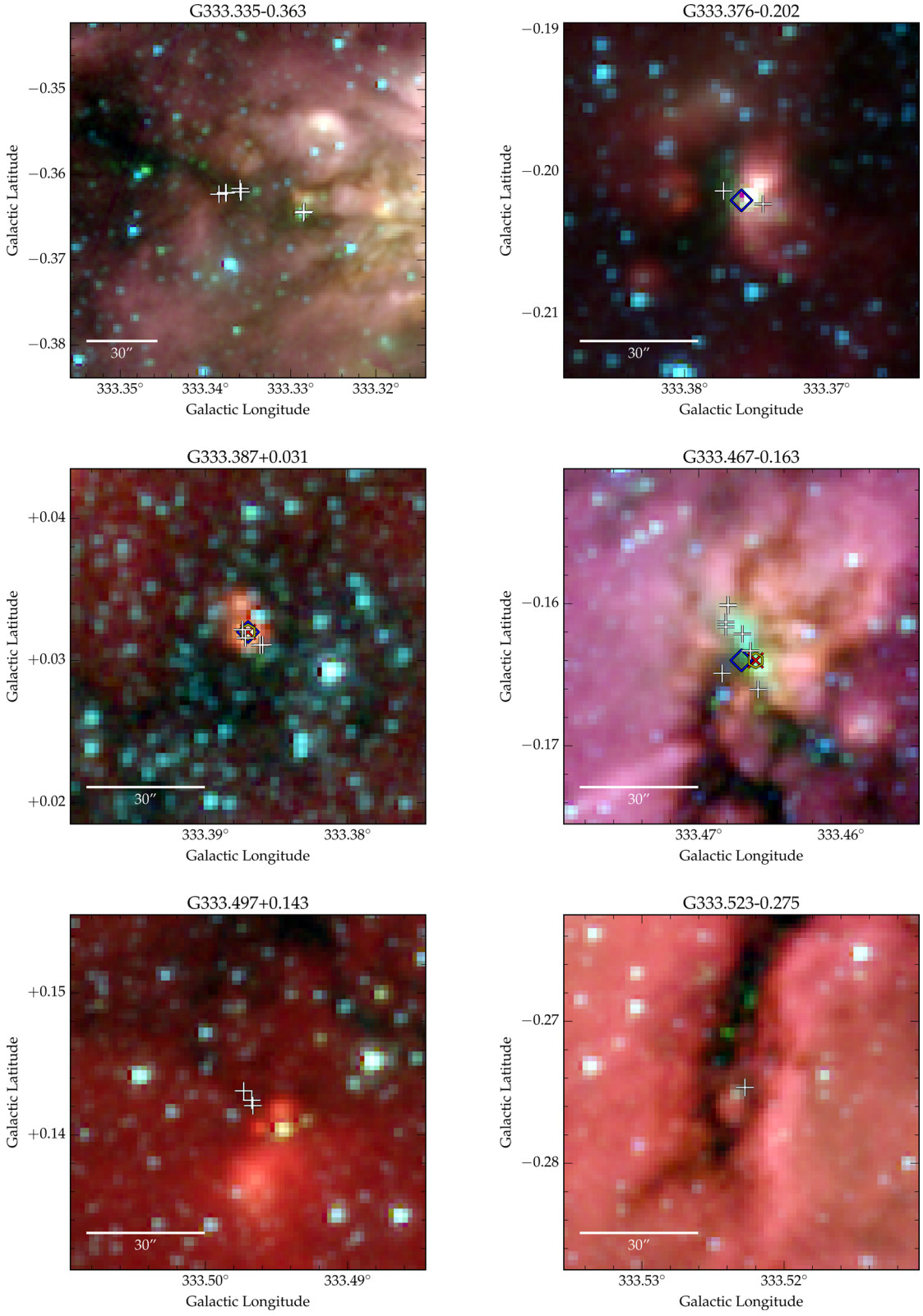

Figure C1 – *continued*

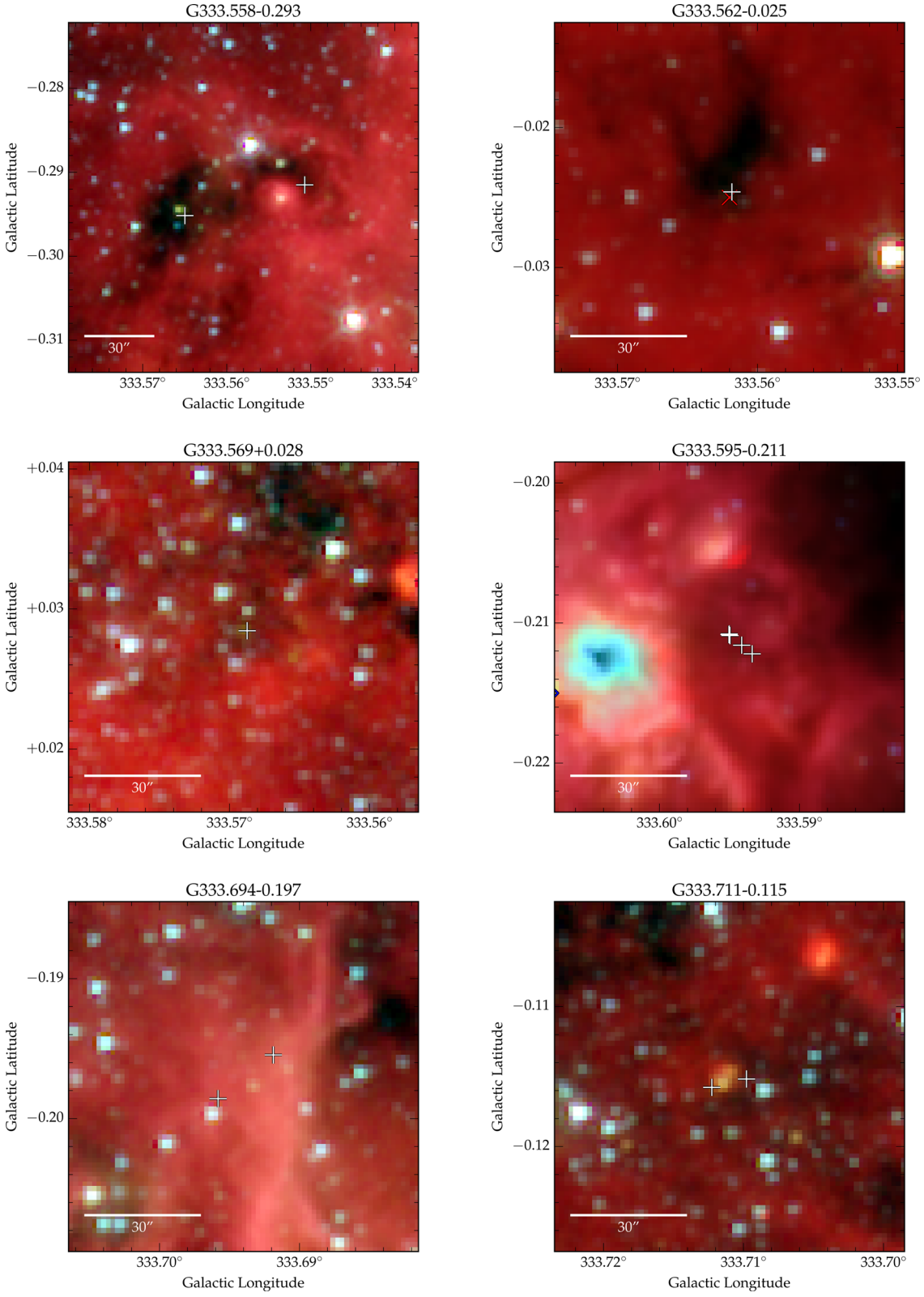

Figure C1 – *continued*

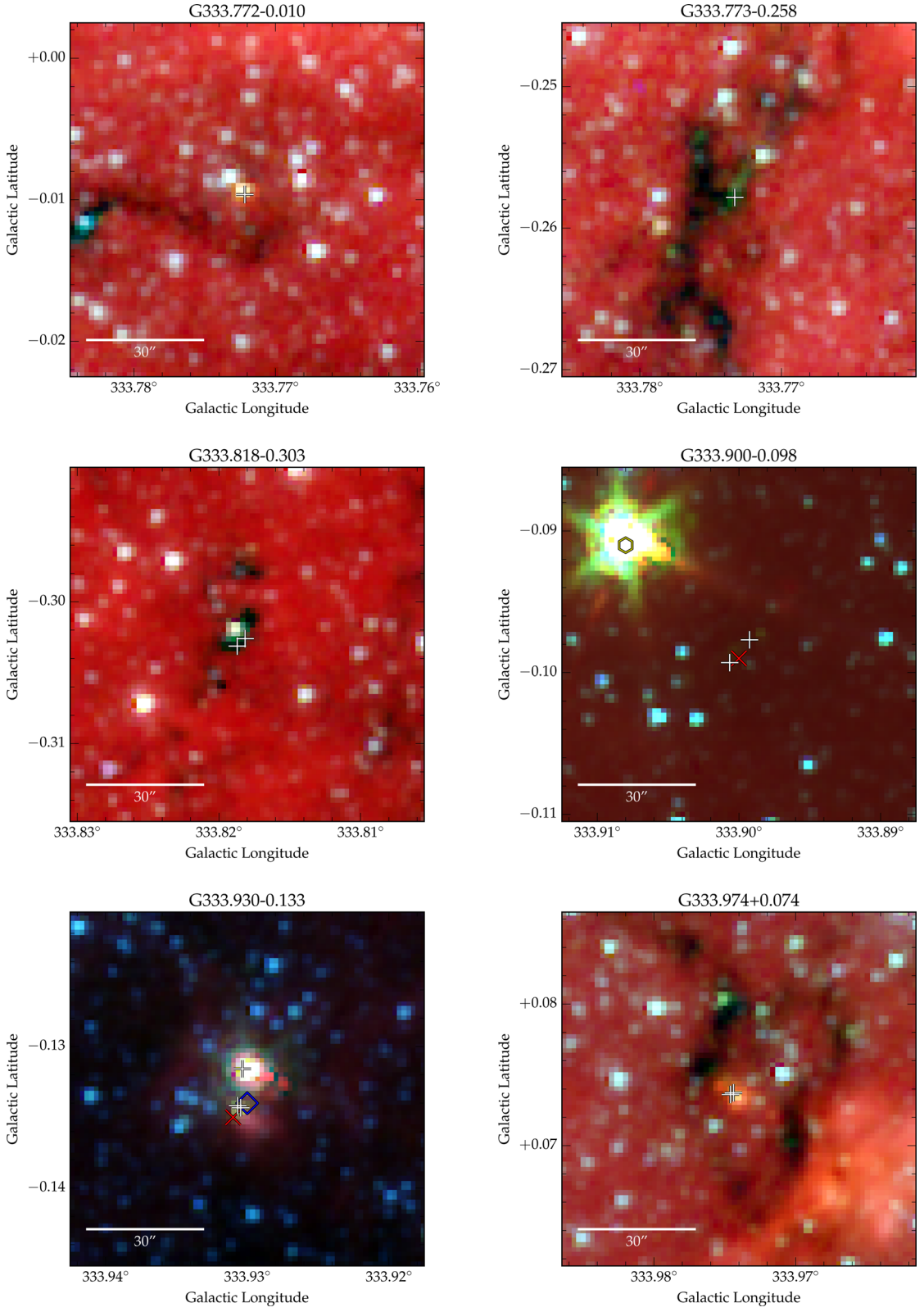

Figure C1 – *continued*

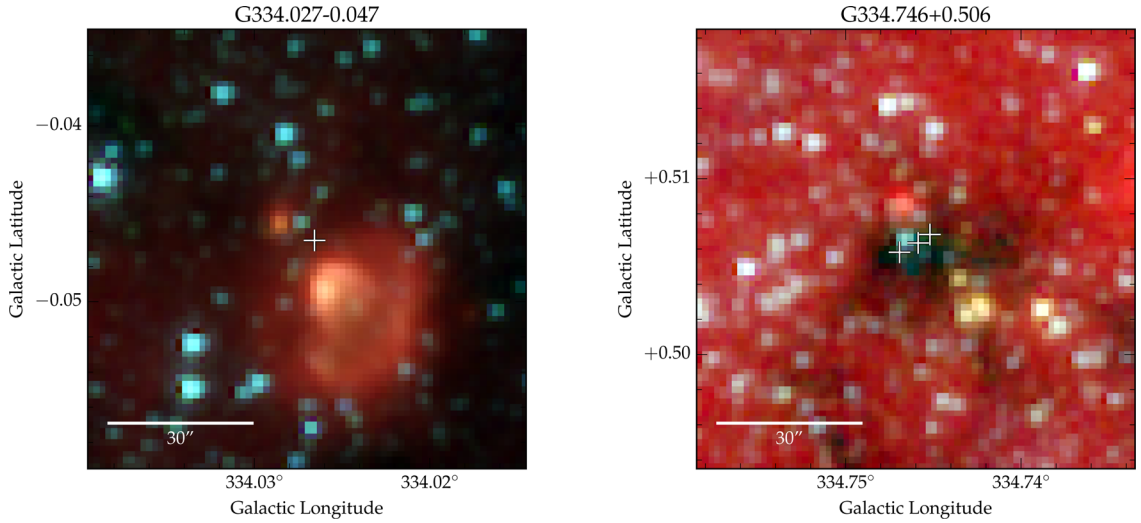

Figure C1 – *continued*

This paper has been typeset from a TEX/LATEX file prepared by the author.